# Transparent and Flexible Radio Frequency (RF) Structures

by

**Taehee Jang**

A dissertation submitted in partial fulfillment
of the requirements for the degree of
Doctor of Philosophy
(Electrical Engineering)
in the University of Michigan
2017

Doctoral Committee:

Professor L. Jay Guo, Chair
Assistant Professor Neil Dasgupta
Associate Professor Anthony Grbic
Professor Kamal Sarabandi

© Taehee Jang 2017

All Rights Reserved

*To my father Dong Won Jang and my mother Kyeong Ja Kim*

*To my wife Myunghye Yoo and my daughter Yuna Jang*

*For their love, support, and dedication*

# ACKNOWLEDGEMENTS

First and foremost, I would like to sincerely express my gratitude to my advisor Professor L. Jay Guo. He has been providing invaluable guidance and full support during the whole process of my research. I have been learned many things from him including technical knowledge, research methodologies, and communication skills. I truly appreciate his patience, wisdom, encouragement and understanding which help me to get through many difficult times during my research. I could not have achieved any of the accomplishments without his support.

I would like to extend my sincere gratitude to my other committee members, Prof. Kamal Sarabandi, Prof. Anthony Grbic, and Prof. Neil Dasgupta for devoting their time to review this thesis and advising me with valuable suggestions. I also grateful that Dr. Adib Nashashibi spent time discussing with me about measurements.

I would like to thank my colleagues and friends at Guo group, Radiation Laboratory and EECS for constructive and insightful discussions. Many thanks to former members, Prof. Hui Joon Park, Prof. Moon Kyu Kwak, Prof. Hongseok Youn, Dr. Jing Zhou, Dr. Young Jae Shin, Dr. Yi-Kuei, Dr. Alex Kaplan, Dr. Jae Yong Lee, Dr. Kyu-tae Lee, Dr. Taehwa Lee, Dr. Ashin Panday, and Andrew Hollowell. I am thankful to current members, Sangeon Lee, Cheng Zhang, Long Chen, Chengang Ji, Qiaochu Li, Xi Chen, Suneel Joglekar, Qingyu Cui for sharing their experiences and time with me. I also appreciate Dr. Kyusang Lee, Hyunsoo Kim, Seungku Lee, Kyungun Jung, Jihun Choi, and Hyeongseok Kim for their great help.

Last, but most importantly, I would like to express my deep appreciation to my dear wife, Myunghye Yoo, and my family, including my parents, younger brother, for their constant encouragement, unconditional love, and unfailing support. Especially, my special thanks go to my beloved wife, Myunghye Yoo, for support and dedication. I couldn’t have done this without the support of my wife. Thank you to my great and adorable daughter Yuna Jang. I am truly blessed to have you in my life.

# TABLE OF CONTENTS

**DEDICATION** . . . . . ... . . . . ii

**ACKNOWLEDGEMENTS** . . . . . iii

**LIST OF FIGURES** . . . . . .. . . . . viii

**LIST OF TABLES** . . . . . .xiv

**ABSTRACT** . . . . . ...xv

**CHAPTER**

**1. Introduction**……...……1

1.1 Background and Motivation……...……...…….……1

1.2 Thesis Outline ……..……...……...…4

**2. Transparent and Flexible Polarization-Independent Microwave Broadband Absorber** .....7

2.1 Introduction.....7

2.2 Principle of Double Resonance.....9

2.3 The design of Broadband Absorber ……...…….11

2.4 Absorber Simulation …….……...14

2.5 Bi-static Scattering from Absorber……...17

2.6 Realization of the Transparent and Flexible Structure……..21

2.7 Multi-layered Ultra Broadband Absorber……...……..27

2.8 Conclusion……..…….29

**3. Semi-Transparet and Stretchable Mechanically Reconfigurable Electrically Small Antennas Based on Tortuous Metallic Micromesh**……...30

3.1 Introduction…….….30

3.2 Mechanically Reconfigurable Antenna Design……..…..33

3.2.1 Zeroth-order Resoannt Antenna Theory Based on Composite Right-handed/Left-handed (CRLH) Transmission Line (TL)……..34
3.2.2 CPW-Fed Inductor-Loaded Zeroth-Order Resonant Antenna……...37
3.2.3 Analysis of Symmetric and Asymmetric CPW-fed ZOW Antennas..41
3.3 The Orientation of Meander Line…….43
3.4 The Design of Tortuous Micromesh……...….47
3.5 Antenna Fabrication and Measurement……...……52
3.6 Conclusion…….....60

**4. Ultra-Low Profile Flexible Triple-polarized Antenna Using Flexible Silver Nanowires and Substrate with High Isolation**…….....61
4.1 Introduction.....61
4.2 The Configuration of the Low-profile Tri-polarization Antenna.....63
4.2.1 The Comparison between Monopole Antenna and ZOR Array Antenna……..67
4.3 Flexible Metallic Via Based on AgNWs…….69
4.4 Simulation and Measurement Results……...71
4.5 Conclusion……...74

**5. Dual-Band/Tri-Polarized Metamaterial Antenna Based on Half-Mode Hexagonal (HMH) Substrate Integrated Waveguide (SIW) Using Flexible Substrate and Vias for WBAN Communications** ……....75
5.1 Introduction……..75
5.2 Half-Mode Hexagonal Substrate Integrated Waveguide……..77
5.3 The Configuration of the Dual-band/Tri-polarization antenna Based on Half-mode Hexagonal SIW……...…….82
5.4 Simulation and Measurement Results……...86
5.5 Conclusion……...90

**6. Conclusions and Future Work**……..……..91
6.1 Summary of Achievements…….....……91

6.2 Future Works……....92

**Bibliography**…….....……..96

# LIST OF FIGURES

Figure

1.1. Landscape of electronics……..2

1.2. Flexible electronics (a) on paper (b) on textile (c) on PET……3

1.3. Transparent electronics (a) skin-like pressure and strain sensors (b) slot antenna using AgHT-4 (c) neural micro-electrode arrays…….....4

2.1. (a) Unit cell of absorber structure (b) Equivalent circuit model……..……9

2.2. (a) Equivalent circuit at low frequency (b) Equivalent circuit at high frequency…10

2.3. Schematic of broadband absorber (perspective view)……..…11

2.4. The design of unit cell (a) top view (design parameters: $w_1$=4mm, $w_2$=1mm, $l_1$=4.2mm, l=10mm). (b) Calculated real and imaginary part of impedance……..12

2.5. Simulated and measured absorption according to the frequency…….14

2.6. (a), (b) represent the electrical amplitude on the top view at 7.4GHz and 10.1GHz and power flow at 7.4GHz and 10.1GHz, respectively. (c), (d) The color represent the amplitude of the electric field and the arrows represent the direction of the electric field on the central cross section of unit cell at 7.4GHz and 10.1GHz, respectively. (e), (f) The color represent the amplitude of the power flow and the arrows represent the direction of the power flow on the central cross section of unit cell at 7.4GHz and 10.1GHz, respectively…….....……..16

2.7. (a) Schematic of electric field and poynting vector localized in the gap between the two bow-tie structures at the low resonant frequency. (b) Schematic of electric field

and pointing vector localized around the edges of the bow-tie structure at high resonant frequency…….17

2.8. (a) Model construction for the bistatic scattering calculation. (b) Field Calculator for post-processing in Ansys HFSS…….……18

2.9. (a) Reflection at normal incidence (b) Reflection with and without bistatic scattering calculation…….…….20

2.10. (a) Simulated absorption at the different width of bow-tie ($w_1$) (the 90% absorption bandwidth at w1=1mm : 50.4%, at w1=2mm : 61.6%, at w1=3mm : 68.2%, at w1=4mm : 72%) (b) Simulated absorption at the different width of bow-tie ($t$) The inset shows the equivalent circuit model of the proposed absorber according to the frequency…….……...22

2.11. (a) Fabricated metallic bow-tie array on top of a flexible and transparent PET layer (Scale bar = 100um) (b) Optical transmittance……...23

2.12. (a) Measurement set-up (b) Time gating in vector network analyzer……..25

2.13. Measured absorptions at different polarization angle $\Phi$.(0, 30, and 45 deg)……..26

2.14. (a) Ansys HFSS simulation model of two unit cells. (b) Absorption according to the different incident angles (0˚, 20˚, 50˚, 60˚, and 70˚)……..….…27

2.15. Configuration of the multi-layer absorber structure (a) Perspective view (b) Top view……..……28

2.16. Simulated absorption. ($W_{m1}$=1.6m, $W_{m2}$=2.2mm, $W_{m3}$=2.8mm, $l_{m1}$=5.1mm, $l_{m2}$=10.8mm, $l_{m3}$=19.4mm, $t_1$=2.4mm, $t_2$=2.2mm, and $t_3$=4mm)……29

3.1. The configuration of transparent and mechanically reconfigurable antenna.....33

3.2. (a) Equivalent circuit model of the CRLH unit cell (b) Dispersion curve of the CRLH unit cell.....34

3.3. (a) The unit cell of epsilon negative (ENG) meta-structured transmission line (MTL) (b) Equivalent circuit model of ZOR antenna.....37

3.4. Dispersion disagram of the unit cell.....38

3.5. Electric field (a) Vector distribution on the antenna (b) The magnitude of electric field at zeroth-order mode……...40

3.6. The relationship between frequency and the number of unit cells……41

3.7. CPW-fed ZOR antennas using (a) one symmetric unit cell (b) two asymmetric unit cell (c) two symmetric unit cells……..42

3.8. Return losses for (a) one symmetric unit cell (b) two asymmetric unit cell (c) two symmetric unit cells……42

3.9. (a) CPW-fed ZOR antenna with larger ground planes (b) Measured return loss for the CPW-fed ZOR antenna with and without larger ground planes…….43

3.10. Simulated and measured transmission spectra of individual colors (blue, green, and red) at normal incidence…….44

3.11. The change of vertical-oriented and horizontal-oriented meander lines with the different tensile strains……45

3.12. Unit cell based on micromesh to extract equivalent circuit parameters……..46

3.13. Topology modification for transparent and stretchable micromesh.....47

3.14. Mechanical simulation of micromesh.....49

3.15. (a) Unit cell of micromesh using both tortuous wires in horizontal and longitudinal direction (tortuous micromesh design 1) (b) Unit cell of micromesh using tortuous wire in horizontal direction and straight wire in longitudinal direction one tortuous (tortuous micromesh design 2).....50

3.16. The schematic of the fabrication for micromesh……..52

3.17. The fabricated transparent and stretchable antenna.....53

3.18. The resonant frequency according to the increase of strains (a) for antenna with both tortuous lines (b) for antenna with only horizontal tortuous line (Solid line : Simulated results, Dashed lines : Measured results)…….54

3.19. The measured optical transmission of the stretchable antenna embedded in PDMS……..56

3.20. The radiation patterns (a) E-plane (xz-plane) (b) H-plane (xy-plane)……57

3.21. A mechanically stretchable device ……..…..……...…….58

3.22. The radiation patterns in response to different tensile strains (0%, 20%, and 40%)…….59

4.1. The configuration of Triple-polarized antenna system …….62

4.2. (a) Perspective view of the antenna (shows port assignments and polarization orientation) (b) top view of tri-polarized antenna. (Dimension [mm] of the antenna are: $w_1$ = 1.88, $w_2$= 0.8, $w_s$ = 1, $l_1$ = 3, $l_S$ = 45.72)…….63

4.3. Simulated surface current distribution with different ports being excited: (a) at port1, (b) at port 2…….64

4.4. (a) ZOR array antenna (Dimension [mm] of the antenna are: $w_1$ = 1.88, $w_2$= 8, $w_l$ = 1.2, g = 0.2, $l_2$ = 1, $l_l$ = 3.6, $l_g$ = 1, $l_p$ = 10) (b) Unit cell of length *p* (c) Dispersion diagram.…….65

4.5. Simulated electric field vector distribution on the ZOR array antenna ……..67

4.6. (a) Configuration of monopole array antenna (Dimension: *W*=60mm, *L*=240mm, *H*=41mm) (b) Return loss (c) Radiation patterns in terms of phase progression….67

4.7. (a) Configuration of ZOR array antenna (b) Radiation pattern……68

4.8. The SEM images of uniform, ultralong and thin AgNWs prepared by hydrothermal method at 160°C-22hours reaction. ……....69

4.9. (a) Side view of AgNW via. (b) Fabricated AgNW via on the PCB substrate.....70

4.10. Fabricated the low-profile, flexible tri-polarized antenna using AgNW vias (a) Top view (b) Bottom view…….....……71

4.11. Measured and simulated return loss of each port the tri-polarized antenna.……..72

4.12. Measured and simulated isolation between each two ports of the tri-polarized antenna……..…….72

4.13. Radiation patterns of the tri-polarized antenna (a) E-plane (+45 deg cut) at Port 1 (b) H-plane (-45 deg cut) at Port 1 (c) E-plane (-45 deg cut) at Port 2 (d) H-plane (+45 deg cut) at Port 2 (e) E-plane (XZ-plane) at Port 3 (f) H-plane (XY-plane) at Port 3……73

5.1. On-body communication and off-body communication in wireless body area network (WBANs)……..……...76

5.2. Configuration of SIW structure ……78

5.3. Simulated magnitude of the total E-field distributions of (a) full-mode SIW, (b) HMSIW, (c) triangular SIW, (d) hexagonal SIW (e) half-mode hexagonal SIW at their dominant resonant frequencies (*w=l=38mm*)……...…80

5.4. Simulated magnitude of the total E-field distributions of (a) full-mode SIW, (b) HMSIW, (c) triangular SIW, (d) hexagonal SIW at their higher-order resonant frequencies (*w=l=38mm*)……..…81

5.5. The configuration of the use of half-mode hexagonal SIW with the arbitrary internal angle…….81

5.6. (a) Equivalent circuit model of a CRLH SIW unit cell. (b) General Dispersion comparison between conventional half wavelength antenna and metamaterial antenna……...83

5.7. (a) Perspective view of the dual-band tri-polarized antenna (a) Dual-band cross-polarized CRLH HMHSIW antenna (b) Dual-band ZOR HMHSIW antenna. (Dimension [mm] of the antenna are: $w_{m1} = w_{z1} = 1.87$, $w_{z2} = 1.19$, $w_{z3} = 0.3$, $w_{z4} = 1.5$, $w_{m2} = 1.5$, $l_{m2} = 6$, $l_s = 6$, $l_{s1} = 3.5$, $g_{m1} = g_{m2} = g_{z1} = 0.2$, $r_{z1} = 0.7$)……..……85

5.8. The fabricated dual-band tri-polarized antenna based on half-mode hexagonal SIW structure ……87

5.9. Measured and simulated return loss of each port of the of the tri-polarized SIW metamaterial antenna……88

5.10. Measured and simulated isolation between each two ports of the of the tri-polarized SIW metamaterial antenna……88

5.11. Measured and simulated radiation patterns of the proposed HMHSIW at both frequencies (a) & (c) E-planes at n=-1st mode (b) & (d) E-planes at n=+1st mode (e) 0th mode at lower frequency (f) 0th mode at higher frequency…….89

6.1. (a) Pure Cyclic Olefin Copolymer (COC) grains (b) Heat-Pressure Imprinting Process…….……..94

6.2. (a) COC-based SIW slot antenna (b) S-parameter……..95

# LIST OF TABLES

Table

3.1. Inductance of meander line according to the orientations and tensile strains……..47

3.2. Comparison between metallic patch, straight mesh, and tortuous mesh……...48

3.3. Relationship between optical transparency and electrical conductivity in terms of the design of micromesh…….51

3.4. Bandwidth of proposed antenna……..…56

3.5. Antenna summary and comparison results for proposed and reference antennas….60

5.1. Comparison between full-mode SIW, HMSIW, TMSIW, and HMHSIW……...82

6.1. Properties of cyclic olefin copolymer……94

# ABSTRACT

## Transparent and Flexible Radio Frequency (RF) Electronics

by

Taehee Jang

Chair: L. Jay Guo

With increasing demand for a wearable devices, medical devices, RFID, and small devices, there is a growing interest in the field of transparent and flexible electronics. In order to realize optically transparent and flexible microwave components, novel materials can be used. The combination of new materials and radio frequency (RF) structures can open interesting perspectives for the implementation of cost effective wireless communication system and wearable device design. The transparent and flexible RF structures can facilitate its application in the transparent and curved surfaces.

In this dissertation, we present several demonstrations, all based on optically transparent and flexible materials and structures. We firstly demonstrate an optically transparent, flexible, polarization-independent, and broadband microwave absorber. The bow-tie shaped array which possesses double resonances is designed and measured. The combined resonances lead to more than 90% total absorption covering a wide frequency range from 5.8 to 12.2 GHz. Due to the use of thin metal and PDMS, the whole structure is optically transparent and flexible. Secondly, we demonstrate a new method for

fabricating transparent and stretchable radiofrequency small antennas by using stretchable micromesh structures. Size reduction is achieved by using the zeroth-order resonant (ZOR) property. The antennas consist of a series of tortuous micromesh structures, which provides a high degree of freedom for stretching when encapsulated in elastomeric polymers and is optically transparent. Accordingly, these antennas can be stretched up to 40% in size without breaking. The resonant frequency of the antennas is linearly reconfigurable from 2.94 GHz to 2.46 GHz upon stretching. Next, we describe an ultra-low profile and flexible triple-polarization antenna. It is realized by using ZOR array antenna with high port-to-port isolation. This flexible antenna is fabricated with a flexible substrate and silver nanowire vias to be used in various wearable applications. Lastly, we demonstrate a dual-band tri-polarized antenna based on half-mode hexagonal (HMH) SIW structure. CRLH HMHSIW antenna and ZOR HMHSIW antenna are designed to have dual-band operating frequencies. This novel antenna can provide much improved wireless communication efficiency for the WBAN system under various incident field angles and polarizations.

# Chapter 1

# Introduction

## 1.1 Background and Motivation

With increasing demand for a wearable devices, medical devices, RFID, and small devices, there is a growing interest in the field of transparent and flexible electronics. In order to realize the optically transparenft and flexible microwave components, the use of novel materials can open up new possibilities for implementation of microwave design and applications.

Flexible electronics is a technology applied in electronic circuits by mounting electronic devices on a flexible substrate. Flexible electronics have been integrated with a variety of applications such as flexible circuits, flexible displays, flexible solar cells, skin-like pressure sensors, and conformable radio frequency identification (RFID) tags. In addition, the transparent electronics are a technology for realizing electronic circuits by replacing with transparent structures or materials. Transparent electronics have been used in a variety of applications such as transparent circuits, transparent display, transparent solar cells, and transparent sensors. Given the benefits of these two kinds of technology, if they could be combined in novel ways in such areas as radiofrequency electronics, it could be possible to develop optically transparent and mechanically flexible radio frequency (RF) electronics have opened a gate to next-generation technologies for the RF electronics that

can be seen through and can be applied to a transparent or conformal object. Some work in this area having done leading to advancements in RF electronics that have focused on producing light weight, high performance RF electronics. Figure 1.1 shows the landscape of electronics. The optical transparency and structural flexibility add another level of complexity for designing radio frequency (RF) electronics because they are required to have the similar performance of rigid and opaque electronics in spite of the use of transparent and flexible materials.

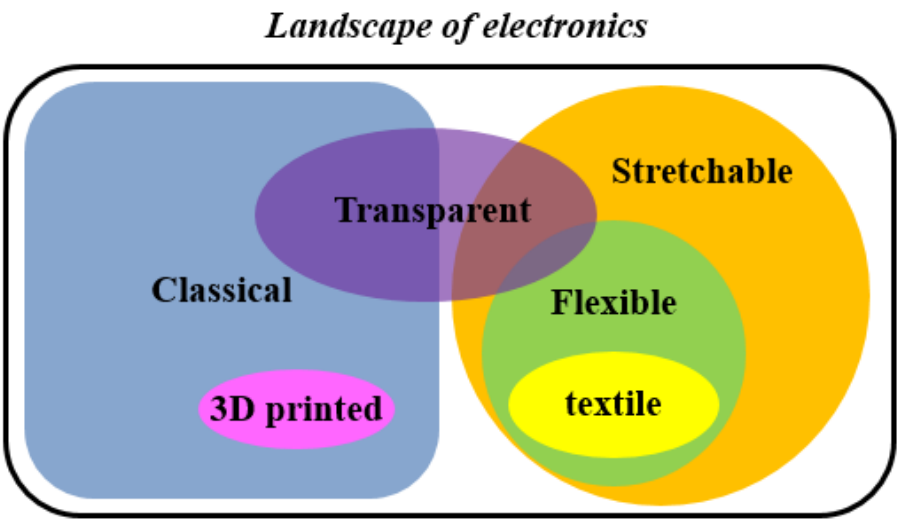


Figure 1.1. Landscape of electronics

Many studies have already been conducted on the transparent and flexible electronics. In the flexible electronics, flexible substrates such as paper, textiles, and PET provides many properties that differ from those of polymide plastics used in conventional flexible PCB technology [1-3]. Flexible electronics based on paper substrates with high flexibility can be folded, easily disposed of, and trimmed with scissors. Paper substrates also have other advantages such as low production costs and light weight. In the production of paper substrate, the metallic patterns are printed onto the paper by evaporation, sputter deposition, or spray deposition as shown in Figure 1.2(a) [4]. Electronic textiles (E-textiles)

are fabrics that can communicate with other devices, transform signals, and conduct energy which are impossible with traditional fabrics. To realize flexible electronics, the electronic elements are integrated with E-textile. In [5], textile-based antenna to create a body area network was used because it is bendable and comfortable enough to be easily inserted into garments in Figure 1.2(b). Even when bent, this antenna could still have excellent performance as well as be connected with radio module. Plastics have also been widely used because they are very cheap and easily controllable materials. In Figure 1.2(c), the mechanically flexible device was fabricated on the polyimide (PI) substrate. The ultrathin molecular-monolayer-based devices can operate reliably when bent, twisted or deformed into helical structures [6].

(a) (b) (c)

Figure 1.2. Flexible electronics (a) on paper (b) on textile (c) on PET

Many transparent materials such as glass, PET, and transparent film have been exploited, all of which show promising characteristics. The optical transparency of electronic devices can be obtained from the material properties or structural properties [7, 8]. In Figure 1.3(a), the pressure and strain sensors are realized by spray-depositing the single-walled carbon nanotubes on PDMS substrate, so that it can be rendered stretchable by applying strain along each axis [9]. The transparent antenna was fabricated on the glass substrate by using the AgHT-4 film, with an operating frequency of 2.3GHz as shown in Figure 1.3(b) [10]. Although AgHT-4 has lower gain compared to their copper

counterparts, it allow the transmission of electric current while still retaining the optical transparency. Figure 1.3(c) shows the transparent optogenetic brain implants that were realized with gold pattern and four stacked single-atom-thick grapheme layers [11]. Thus, it could remain reliable in various bending configurations, including the twisted and helical structure.

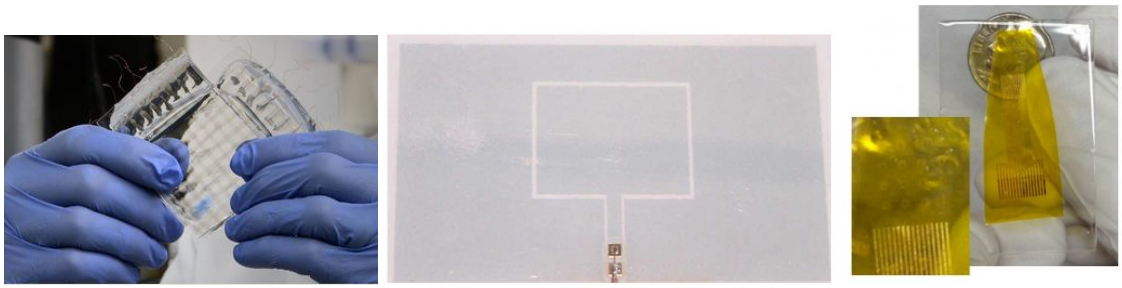

(a) (b) (c)

Figure 1.3. Transparent electronics (a) skin-like pressure and strain sensors (b) slot antenna using AgHT-4 (c) neural micro-electrode arrays

The combination of new materials and radio frequency (RF) electronics can open interesting avenues for the implementation of cost effective wireless communication system and wearable device design. The transparent and flexible radio RF electronics can facilitate its application in the transparent and curved surfaces. Thus, my research focuses on investigation of transparent and flexible RF devices, with an aim of new materials and fabrication techniques.

## 1.2 Thesis outline

This thesis explores the optically transparent and structurally flexible radio frequency electronics which can be applied to the transparent and curved surfaces. In the sections that follow, the design objectives and principles of operation are presented.

**Chapter 2: Transparent and Flexible Polarization-Independent Microwave Broadband Absorber**

A polarization-independent broadband absorber with optical transparency and structural flexibility is introduced and discussed in this chapter. These are the highly desired properties for a wide variety of applications such as stealth ship and airplane. In this chapter, we will also discuss how the absorption bandwidth can be improved. The absorber is designed to have the double resonance, so that it can have broader bandwidth by merging the double resonance.

**Chapter 3: Semi-transparent and Stretchable Mechanically Reconfigurable Electrically Small Antennas Based on Tortuous Metallic Micromesh**

Chapter 3 describes the optically transparent and mechanically reconfigurable small antenna based on the use of micromesh. Due to the transparency and flexibility, it can be smoothly integrated with interiors and exteriors of electronic devices, such as cell phones, laptops, and tablets. This mechanical tenability enables the broadband operation of the small antenna to be efficiently utilized.

**Chapter 4: Ultra-Low Profile Flexible Triple-Polarized Antenna Using Flexible Silver Nanowires and Substrate with High Isolation**

Chapter 4 presents a flexible triple-polarization antenna and discusses its great potential applications such as WBAN network and MIMO. The omni-directional horizontal polarization and conical vertical radiation patterns are obtained by using cross-

polarized slot antennas and ZOR array antenna. A silver nanowires are used to realize the flexible vias in the design.

**Chapter 5: Dual-Band/Tri-Polarized Metamaterial Antenna Based on Polagon-Mode (PM) Substrate Integrated Waveguide (SIW) Using Flexible Substrate and Vias for WBAN communications**

Chapter 5 describes a half-mode hexagonal substrate integrated waveguide (HMHSIW) structure which can to reduce the size and efficiently integrate with other SIW structures in a single elements. Since it operates at dual frequency bands, it can be used for simultaneously transmitting and receiving these two bands. The dual-band tri-polarized HMHSIW structure which four HMHSIW can be closely placed is designed, fabricated, and analyzed.

Chapter 6 summarizes the main findings of each chapter, followed by future plans.

# Chapter 2

# Transparent and Flexible Polarization-Independent Microwave Broadband Absorber

## 2.1 Introduction

Broadband absorbers can reduce the reflection and scattering of electromagnetic (EM) waves from the structures over a wide frequency range. Because of these characteristic, they can be exploited to enhance the efficiency of photovoltaic devices [12, 13] and thermal detectors [14], and can also render objects undetectable by EM waves [15]. Absorbers can be designed by using classical electromagnetic wave theory or by engineered metamaterials. Metamaterial absorbers have been designed by manipulating the effective permittivity $\varepsilon(\omega)$ and permeability $\mu(\omega)$ to match the impedance to free space [16-20]. Due to the lossy components of permittivity and permeability, the structure is then able to the transmitted power. Although metamaterial based absorbers offer the potential advantages of perfect absorption and thin thickness, their use in practical applications is limited due to their very narrow bandwidths. In order to improve the bandwidth, multi-band absorbers have been introduced that utilize multiple layered structures [21, 22]. However, significant challenges rise because these multilayered structures are thick and require a complicated fabrication process. Another approach is classical electromagnetic absorbers, which can be realized by

placing one or more additional resistive sheets in the structure to generate losses to the incident field. One of the classic electromagnetic absorbers is Salisbury screen, which have a resistive sheet placed at $\lambda/4$ over a ground plane [23]. This absorber also has some drawbacks similar to other structures such as narrow bandwidth and relatively large thickness. Another classical absorber is the Jaumann absorber, which utilizes a multi-layer structure to increase the bandwidth [24, 25]. However, to obtain the broad bandwidth, the structure becomes very thick and bulky. A further weakness is that the absorbers constructed from the conventional materials are typically rigid and optically opaque. If the absorber can be made optically transparent and structurally flexible, it can provide high design freedom for practical applications [26, 27]. For example, optically transparent and flexible absorber can be applied to applications such as window glass and curved surfaces.

In this chapter, we propose and demonstrate an optically transparent, flexible, polarization-independent, and broadband microwave absorber. The absorber is based on two principles: 1) it utilizes resonant structure to provide the impedance match to the air, such that EM energy can be coupled into the structure with little reflection; 2) the resonator is made of Al wire grid to induce ohmic loss and effectively dissipates the coupled EM energy to heat. We found that a bow-tie shaped resonator provides easy tunability of the resonance bandwidth. The new structure is designed to possess two resonances resulting from the symmetric bow-tie structures as well as the coupling between the neighboring bow-tie structures. Therefore, the bow-tie array collectively provides a broadband response. The symmetric bow-tie structure also provides a polarization-independent property. The proposed structure is realized using an Al wire grid, transparent and flexible Polyethylene terephtalate (PET) film, and Polydimethylsiloxane (PDMS) layers. The

overall structure is transparent and flexible, facilitating its application in curved surfaces. The fabricated absorber structure produces the absorption above 90% in the frequency range of 5.8-12.2GHz, and the bandwidth is 71.1% of the center frequency.

## 2.2 Principle of Double Resonance

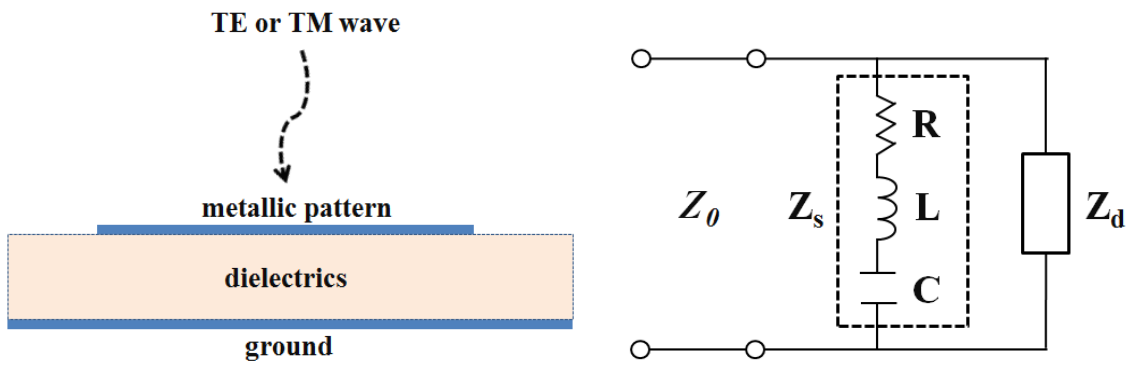


(a) (b)

Figure 2.1. (a) Unit cell of absorber structure (b) Equivalent circuit model

Figure 2.1(a) shows the structure for achieving broadband absorption. Based on the equivalent circuit as shown in Figure 2.1(b), the total impedance of the structure is composed of the impedances of metallic resonator and dielectric layer with the ground plane. The metallic resonator can be regarded as the series resonant circuit, so that its impedance ($Z_s$) is given by

$$Z_s = R + j\omega L + \frac{1}{j\omega C} \tag{2.1}$$

where $C$ and $L$ represent the capacitance and the inductance of resonant structure respectively, and $R$ is the resistivity from the ohmic loss of the metal.

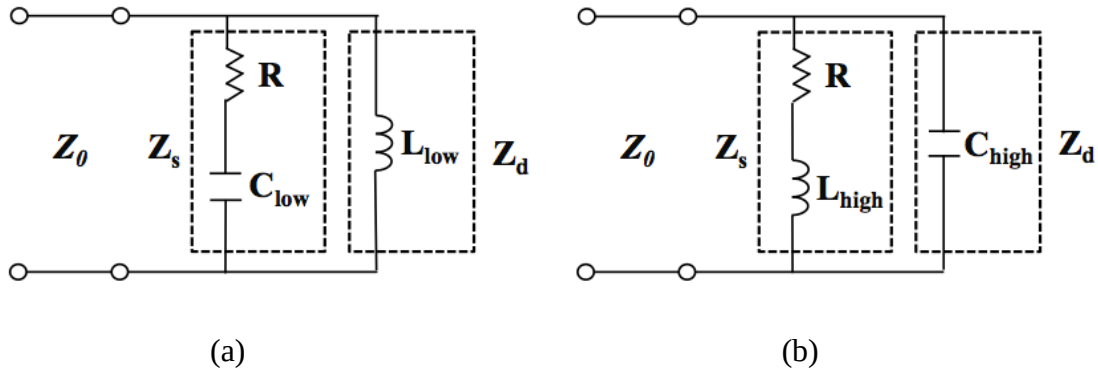


(a) (b)

Figure 2.2. (a) Equivalent circuit at low frequency (b) Equivalent circuit at high frequency

As you can see in Figure 2.2, $Z_s$ behaves like a capacitor at low frequency, and an inductor at high frequency. The quality factor of series resonant circuit is given by

$$Q_S = \frac{1}{R}\sqrt{\frac{L}{C}} \tag{2.2}$$

which shows that Q decreases as R increases. In addition, the impedance of the dielectric layer with ground is given by

$$Z_d = j\frac{Z_0}{\sqrt{\varepsilon_r}}\tan(\beta d) \tag{2.3}$$

where $Z_0$ is the characteristic impedance of free space and d is the thickness of dielectric layer. $\beta = \omega\sqrt{\mu_0\varepsilon_0\varepsilon_r}$ is propagation constant in the dielectric layer. $Z_d$ behaves as an inductor at low frequency, and a capacitor at high frequency. The Q of this resonator is determined by

$$Q_d = \frac{\beta}{2\alpha} \tag{2.4}$$

where $\beta = 2\pi/\lambda$ is the propagation constant and $\alpha$ is the attenuation constant. Since the impedance of top metallic pattern and the dielectric slab with ground are connected in parallel, the total impedance is given by

$$Z_{total} = Z_s \square Z_d = \frac{Z_s Z_d}{(Z_s + Z_d)} \tag{2.5}$$

The resonance for the equivalent circuit occurs when $Z_{total}$ is matched to the free space impedance. According to the change of frequency, $Z_s$ and $Z_d$ are changed and can have the two kinds of equivalent circuit. Since the resonances occur when $Z_{total}$ matches the free space impedance, the double resonance can occur as shown in Figure 2(c). Then, the two resonances are merged to have a broad bandwidth. The total Q-factor is determined by the parallel combination of $Q_s$ and $Q_d$. High Q factor naturally leads to narrow band operation. To achieve broadband absorption, we want to lower the total Q factor by increasing the resistance R in the equivalent circuit model, and the increased resistance also has the additional benefit of dissipating the energy, therefore result in minimized reflection. This can be accomplished by using a very thin metal film to construct the resonant structure.

## 2.3 The Design of Broadband Absorber

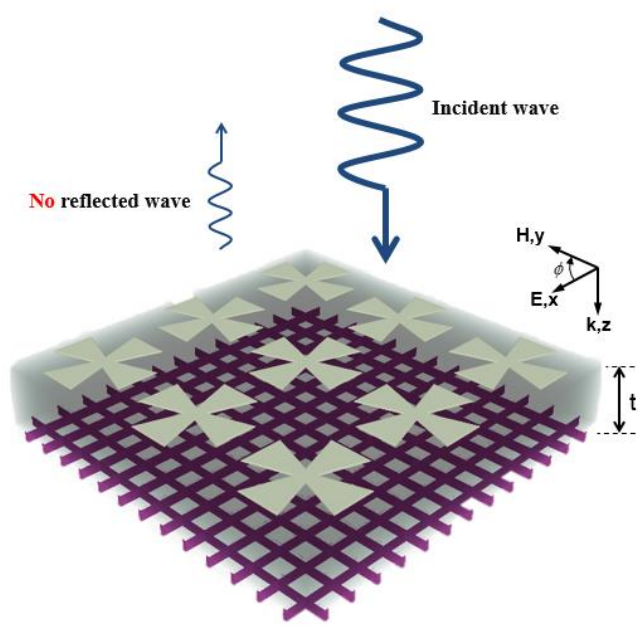


Figure 2.3. Schematic of broadband absorber (perspective view)

In order to achieve perfect absorption, the impedance of the absorber is matched to the air and then the transmitted waves are dissipated due to the loss components of the structure. The previously reported experiment of concealing an object by a carbon nanotube (CNT) coating across the entire visible band follows the same principle [18], where the aligned CNTs with low fill ratio provided the index/impedance match to air; and also absorb the light energy coupled into the CNT layer. However, if we attempted to extend the approach to the microwave range, the required CNT thickness would be impractically thick. To avoid this problem, we used an array of resonant structure to achieve the impedance matching function.

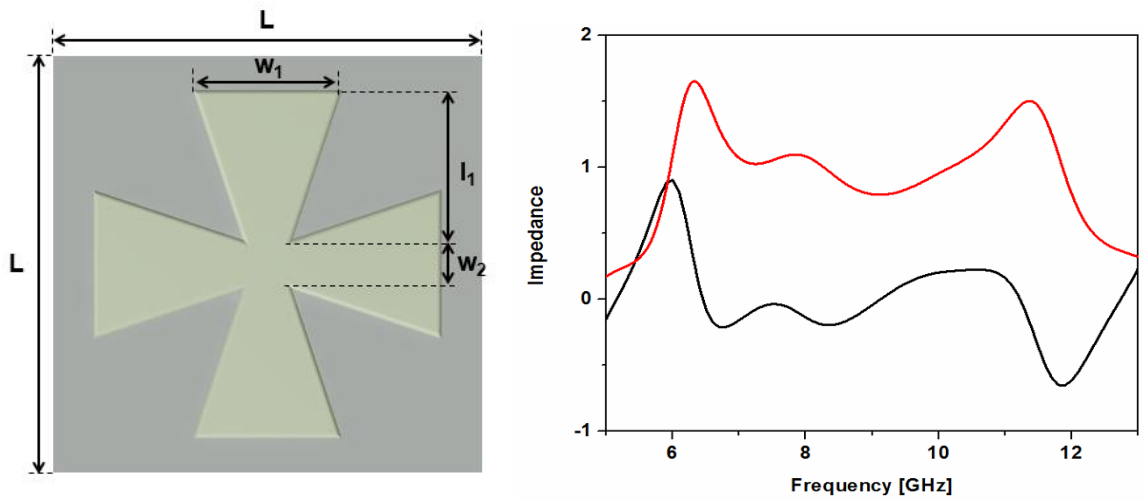


(a) (b)

Figure 2.4. The design of unit cell (a) top view (design parameters: $w_1$=4mm, $w_2$=1mm, $l_1$=4.2mm, l=10mm). (b) Calculated real and imaginary part of impedance.

Figure 2.3 shows the structure used to achieve broadband absorption. The total impedance of the structure is obtained from the combination of the impedances of the metallic resonator and dielectric layer with the ground plane. The effective impedance of the structure can be obtained from [19]

$$Z_{eff}(\omega) = \sqrt{\frac{\mu_{eff}(\omega)}{\varepsilon_{eff}(\omega)}} = \sqrt{\frac{(1+S_{11})^2 - S_{21}^2}{(1-S_{11})^2 - S_{21}^2}} \tag{2.2.1}$$

where $\varepsilon_{eff}(\omega)$ and $\mu_{eff}(\omega)$ are the effective permittivity and permeability, respectively. The real and imaginary part of the impedance are calculated from the simulated complex S-parameters and plotted in Figure 2.4(b). The effective impedance of the structure has two matched bands that result from the change of the electric and magnetic response corresponding to the change of permittivity and permeability. This impedance matching condition causes the reflected wave to be minimized.

The resonant structure having a high Q factor can be utilized in applications such as narrow band filters and oscillators that require the high selectivity and low loss. In such applications, broadband absorption can be achieved by reducing the Q factor of the structure, which can be accomplished by increasing the resistance. This increased resistance has the additional benefit of dissipating the energy, resulting in minimized reflection over a broad frequency range. To increase the resistance, Al wire grid in a bow-tie pattern is used to construct the resonant structure. For our design, we used bow-tie shaped resonator, which has a symmetric configuration that is less sensitive to the polarization of the incident wave. More importantly, we will show that the bow-tie shape can offer a broader response range by exploiting not only its own resonance, but also the coupling between the neighboring unit cells in a periodic array via the side of the bow-ties. Regardless of the number of unit cells, the resonant frequency of the cascaded circuit is determined by the resonant frequency originating from the two kinds of equivalent circuit. By merging the two resonances, we achieved a broad bandwidth 71.1% of the center frequency.

## 2.4 Absorber Simulation

The RF reflectance and the transmittance are measured at normal incidence. The measured reflectance is normalized with respect to a metal plane, while the measured transmittance is normalized with respect to the incident wave in free space. The measured transmission and reflection are then used to obtain the absorption, which is defined as

$$A(\omega) = 1 - T(\omega) - R(\omega) \tag{2.2.2}$$

where $R(\omega) = |S_{11}|^2$, and $T(\omega) = |S_{21}|^2$ are the reflectance and transmittance obtained from the measured frequency-dependent complex S-parameter, respectively. In principle, when the impedance of the structure is matched to the air to minimize the reflection, a perfect absorption can be achieved because the metallic ground plane prevents any transmission through the structure. The simulated and measured $A(\omega)$ are plotted in Figure 2.5. As expected, transmission represented by $S_{21}(\omega)$ is nearly zero in the entire operating frequency range.

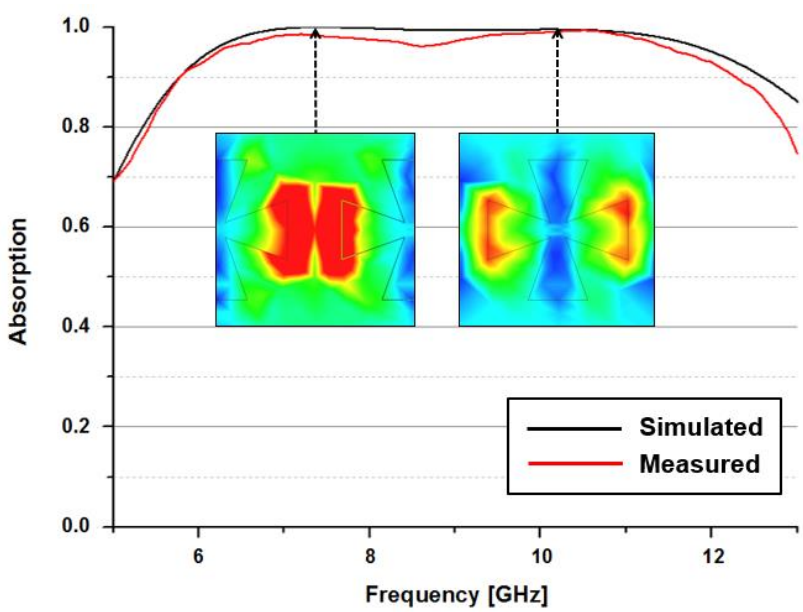


Figure 2.5. Simulated and measured absorption according to the frequency.

As can be seen in Figure 2.5, there are two absorption peaks; the low frequency is mainly attributable to the coupling field between bow-tie structures and the high frequency resonance is due to the fundamental resonant mode of bow-tie structure, as discussed below. To understand the origin of these two absorption peaks, the electrical field distribution and power flow are simulated and analyzed by using Ansys high frequency structure simulator (HFSS) software. In the simulations, the top metallic wire grid bow-tie resonators are modeled as an impedance sheet with a sheet resistance of $30\Omega/sq$ and the dielectric constant and loss tangent of the dielectric spacer are 2.25 and 0.01, respectively. A unit cell of the structure is simulated using periodic boundary conditions along the x and y directions. The proposed absorber with $w_1$ = 4mm has two resonances, one at 7.4GHz and the other at 10.1GHz. Besides the simulation, as can be seen in Figure 2.4(b), we calculated real and imaginary parts of impedance. The real part of impedance is almost unity and the imaginary part of impedance is nearly zero between 7.4 GHz and 10.1GHz. Therefore impedance matching with air was achieved, which minimizes the reflection from the absorber. Figure 2.6(a) and (b) show the top view of the simulated electrical field distribution of the absorber structure at the two absorption peak frequencies ($f_1$=7.4GHz and $f_2$=10.1GHz), while Figure 2.6(c) and (d) show the simulated electrical field distribution at the central cross section. The electric fields are strongly localized in the gap between the two bow-tie structures at the low resonant frequency, and are localized around the edges of the bow-tie structure at high resonant frequency. Figure 2.7(e) and (f) show the power flow of the absorber at two absorption peak frequencies. Figure 2.7(a) and (b) show the schematic of the electrical fields and power flows localized at low and high resonant frequencies, respectively. The behavior is similar to that of magnetostatic

interference [28] in metallic slit structures, where the polarized electric charge produces a strong localized E-field, which guide the poynting energy flow, as shown in Figure 2.7(a) and (b). At low resonant frequency, most incident power flows through the gap between the bow-tie structures; while at high resonant frequency, the power flow is toward the center of bow-tie resonator. In both cases, the energy flowing into the bow-tie eventually dissipates in response to the high ohmic loss of the Al wire grid that is used to form the bow-tie structure. These results verify that the two absorption peaks are a product of the fundamental resonance of the bow-tie structure and the coupling between bow-tie structures, respectively. The merging of the two resonances with overlap spectra ensures the broadband performance of the proposed absorber.

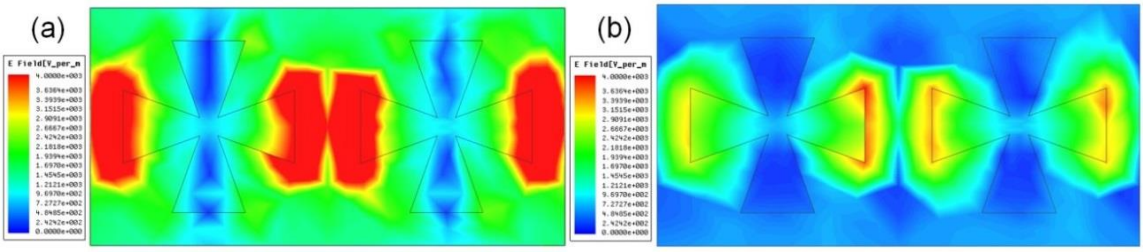


(a) (b)

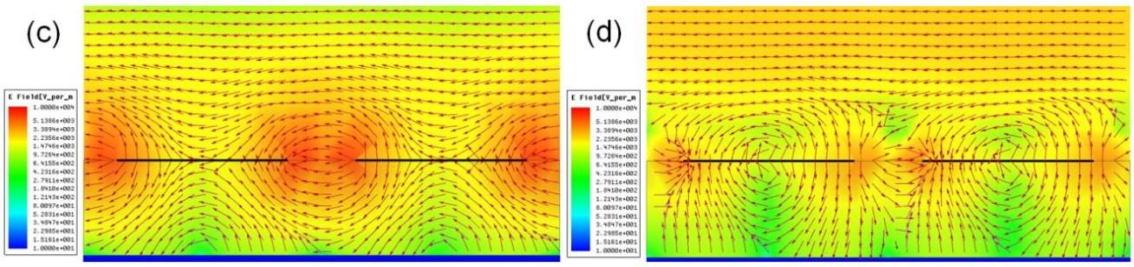


(c) (d)

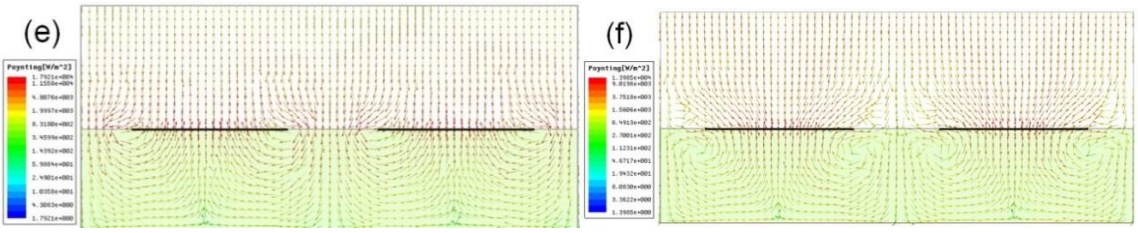


(e) (f)

Figure 2.6. (a), (b) represent the electrical amplitude on the top view at 7.4GHz and 10.1GHz and power flow at 7.4GHz and 10.1GHz, respectively. (c), (d) The color represent the amplitude of the electric field and the arrows represent the direction of the electric field on the central cross section of unit cell at 7.4GHz and 10.1GHz, respectively. (e), (f) The color represent the amplitude of the power flow and the arrows represent the direction of the power flow on the central cross section of unit cell at 7.4GHz and 10.1GHz, respectively.

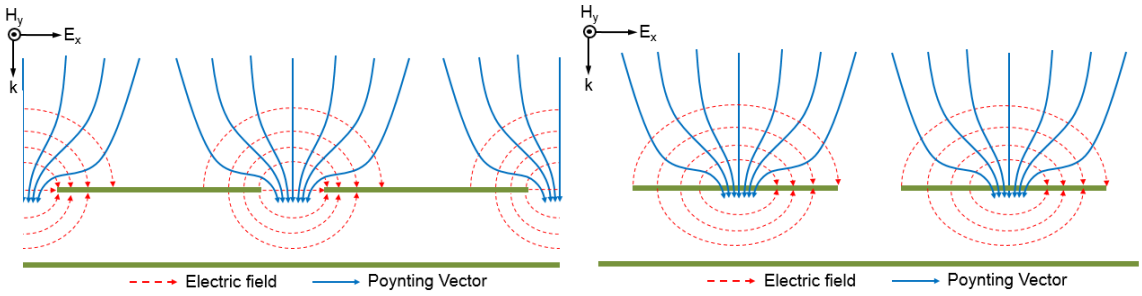


(a) (b)

Figure 2.7. (a) Schematic of electric field and poynting vector localized in the gap between the two bow-tie structures at the low resonant frequency. (b) Schematic of electric field and pointing vector localized around the edges of the bow-tie structure at high resonant frequency.

## 2.5 Bistatic Scattering from Absorber

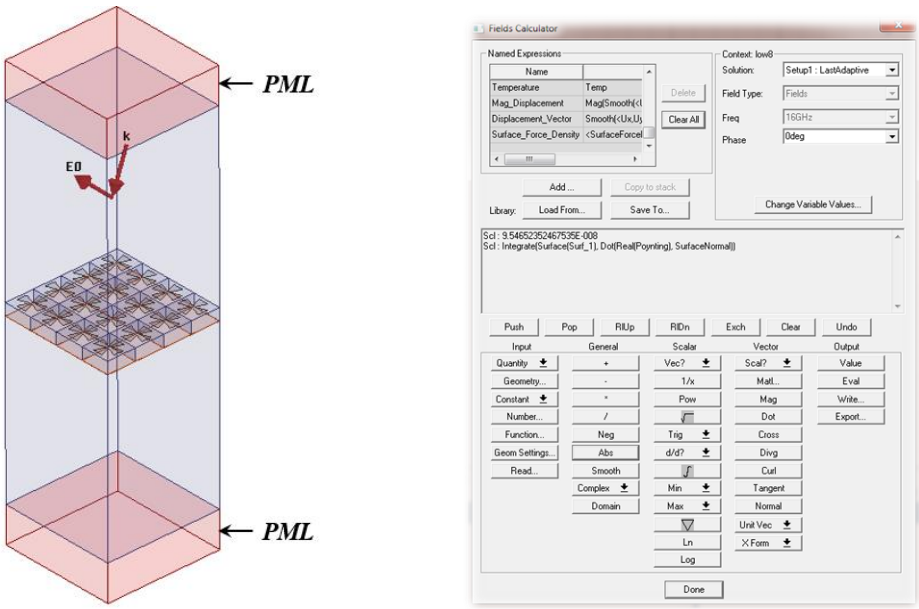


(a) (b)

Figure 2.8. (a) Model construction for the bistatic scattering calculation. (b) Field Calculator for post-processing in Ansys HFSS.

A large filed is scattered in the specular direction; i.e., the angle of reflection is equal to the angle of incidence. On the other hand, the reflected wave can be scattered to the other directions because of the structural properties. Thus, the absorber scattering model is used to examine the biscattering properties of our design in this section. Ansys HFSS is capable of computing plane-wave scattering solutions. For a normal incidence, scattering solution can be calculated using a waveguide simulation approach with port excitations. However, since the off-normal incidence requires field post-processing for the data extraction from plnae-wave excited solutions, the field post-processing for data extraction from plane-wave excited solutions is used. The Ansys HFSS model for bistatic scattering measurement is constructed as shown in Figure 2. 8(a). For incidence angle of arrival (0, θ), where θ=0-60˚, Master/Slave phase relation is set to (180, θ) to correspond to the specular angle. The

same variables are used in master/slave boundary setting. Thus, the incident wave varies from normal to 60˚ incidence angles. The height of air on each side of the absorber is considered as the necessary evaluation planes for the field calculator, and PML slabs are added on the top and bottom of the air box. The linked boundary phase setting is changed with the incidence angle.

Since minimum height to clear 60˚ angled plane is $2\times tan(60^\circ)+\lambda/10$, the height of the air should be higher than 25 mm. The cut planes for the calculation are generated from the geometry menu, and those are created normal to both the incident and the scattered ray directions. The height of air on each side of the dielectric must consider the necessary evaluation planes for post-processing. The cut plane for magnitude (or phase) integration data cannot intersect the dielectric itself because of the very high reactive near fields. For the post-processing, the field calculator is used to extract two quantities, incident magnitude ($P_{inc}$) and reflected magnitude ($P_{ref}$). Then these quantities are used to compute reflection coefficient.

$$\Gamma(\theta)=\sqrt{\frac{P_{ref}(\theta)}{P_{inc}(\theta)}}=\sqrt{\frac{\int_S \frac{1}{2}\left(E_{ref}(\theta)\times H_{ref}(\theta)\right)\cdot dS}{\int_S \frac{1}{2}\left(E_{inc}(\theta)\times H_{inc}(\theta)\right)\cdot dS}} \tag{2.5.1}$$

Because the field calculator provides the RMS Poynting vector, the desired surface is selected directly and integrated. The Poynting vector is calculated using only the $E$ and $H$ field components of interest for the reflection. The calculated reflection at normal incidence is plotted in Figure 2.9(a). The reflections with and without bistatic scattering calculation are plotted in Figure 2.9(b), respectively. Blue dots shows the reflection magnitude when the angle of reflection is equal to the angle of incidence. Red dots represent the reflection

which includes all reflections of the side wall of air box. As the incidence angle increases, the reflection with bistatic scattering calculation becomes higher than the reflection without it.

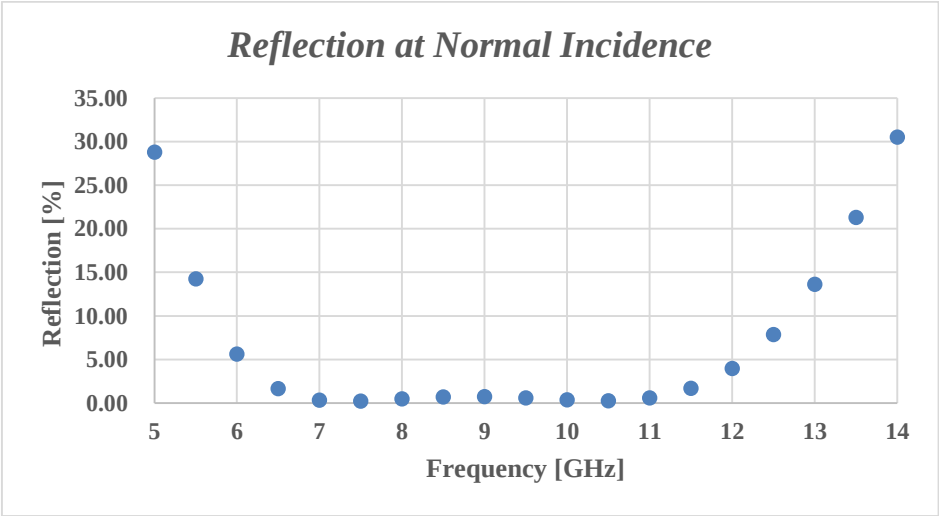


(a)

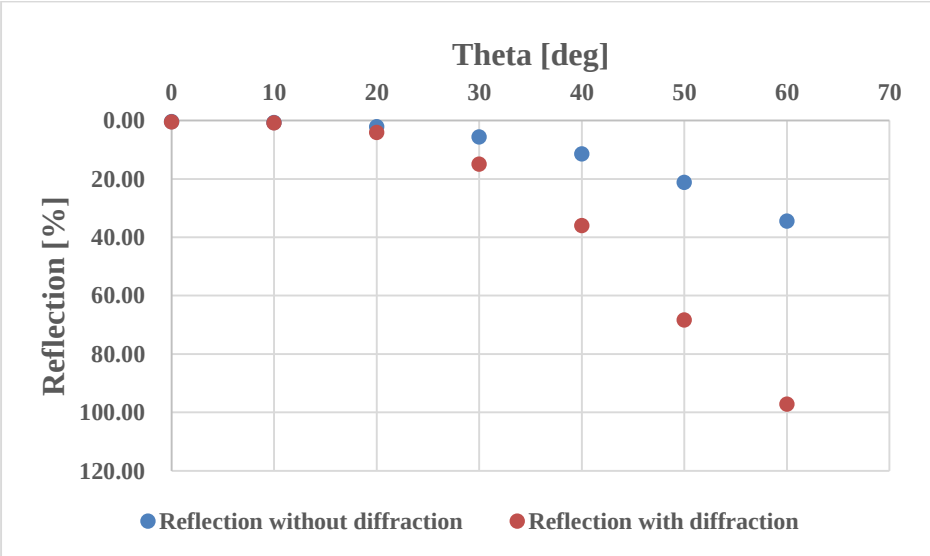


(b)

Figure 2.9. (a) Reflection at normal incidence (b) Reflection with and without bistatic scattering calculation.

## 2.6. Realization of the Transparent and Flexible Structure

The proposed absorber is composed of top Al wire grid metallic patterned patches, PET, PDMS, and metallic wire grid ground. Figure 2.3(a) shows the schematic of the proposed absorber consisting of an array of Al wire grid metallic bow-tie resonators on a PDMS dielectric layer backed by a metallic wire grid mesh ground plane. Figure 2.3(a) shows the proposed absorber arranged in a periodic array, and figure 2.4(b) shows the unit cell with the design parameters. A flexible and transparent PET and PDMS layer separate the two metallic layers. Such flexible polymer layers with patterned bow-tie structures are optically transparent, and can be applied to any metallic surface to provide the broadband absorption property.

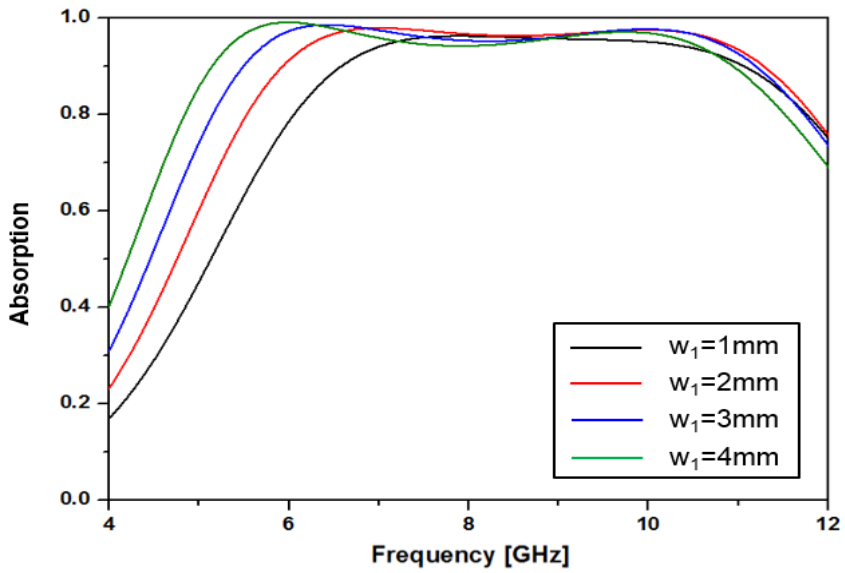


(a)

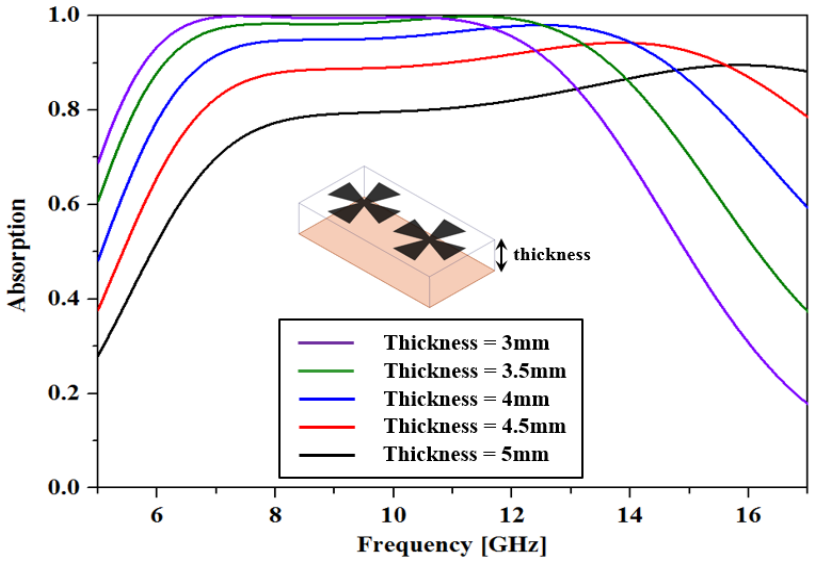


(b)

Figure 2.10. (a) Simulated absorption at the different width of bow-tie ($w_1$) (the 90% absorption bandwidth at w1=1mm : 50.4%, at w1=2mm : 61.6%, at w1=3mm : 68.2%, at w1=4mm : 72%) (b) Simulated absorption at the different width of bow-tie ($t$) The inset shows the equivalent circuit model of the proposed absorber according to the frequency.

In designing the broadband absorber, the geometric parameters, including the thickness of metallic patterns, are chosen to obtain the desired wave absorptions at two resonance frequencies; and these parameters are further optimized so that the two resonances are spectrally merged together to provide broadband characteristics. As an example, Figure 2.10(a) shows that as base ($w_1$) of the bow-tie increases, the absorption band extends to lower frequency range. Here, the length of bow-tie and the spacing are fixed to $l$ =10mm and $t$ = 5mm, respectively. In Figure 2.10(b), the thickness of the substrate is changed from 3mm to 5mm. As the thickness decreases, the higher operating spectrum is shifted into the higher band and the absorption became lower at the lower

frequencies. To reduce the reflection from the absorber structure, good impedance matching to air is required.

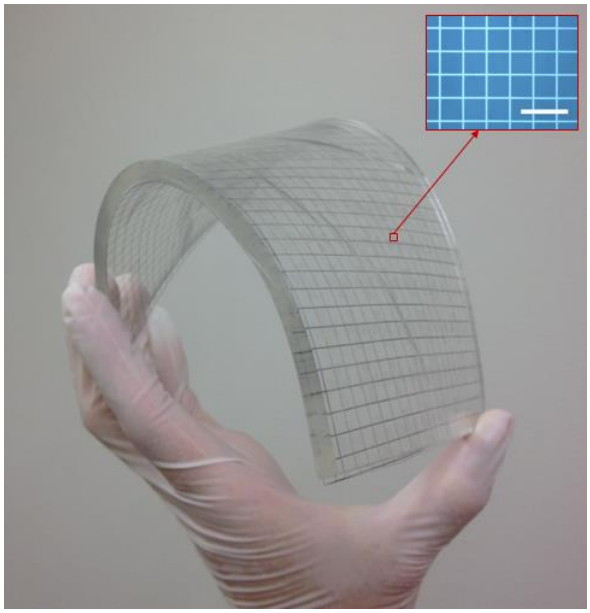

(a)

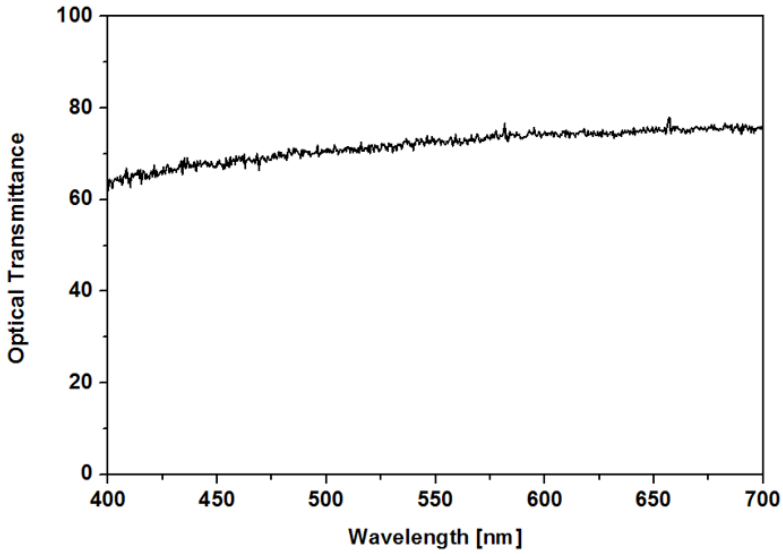


(b)

Figure 2.11. (a) Fabricated metallic bow-tie array on top of a flexible and transparent PET layer (Scale bar = 100um) (b) Optical transmittance.

This can be achieved by varying the spacing between bow-tie structure and dielectric spacer layer thickness as well as using the optimized metal thickness. In order to obtain greater than 90% absorption over the desired bands, the absorption magnitudes and frequencies at the two resonances are optimized by adjusting the thicknesses of the dielectric layer (PDMS) and the surface impedance of metallic wire grid bow-tie resonator (Aluminum). For the bow-tie shaped resonator made of Al mesh with surface resistance of $30\Omega/sq$ , the optimized Al thickness is 62nm, while the PDMS layer with dielectric constant 2.25 and thickness of 4.9mm is utilized for a spacer. The surface resistivity of the deposited metal film was measured using a standard four-point probe configuration. Furthermore, a transparent metal mesh ground plane that provides optical transparency greater than 90% [29] is employed.

To fabricate the absorber structure having an area of 300mm$\times$ 200mm, a 62nm-thick aluminum was first deposited on a 50um-thick PET film by sputtering. The aluminum wire grid mesh was then patterned in the shape of the bow-tie by optical lithography and etching. Then the PET film with patterned Al structure is attached to a thicker and more flexible PDMS layer. A picture of the fabricated bow-tie array on top of PET is shown in Figure 2.11(a). The inset in Figure 2.11(a) shows the zoomed view of bow-tie of Al wire grid mesh. The fabricated structure is optically transparent, and when attached to a wire grid metallic ground plane, forms a complete absorber structure.

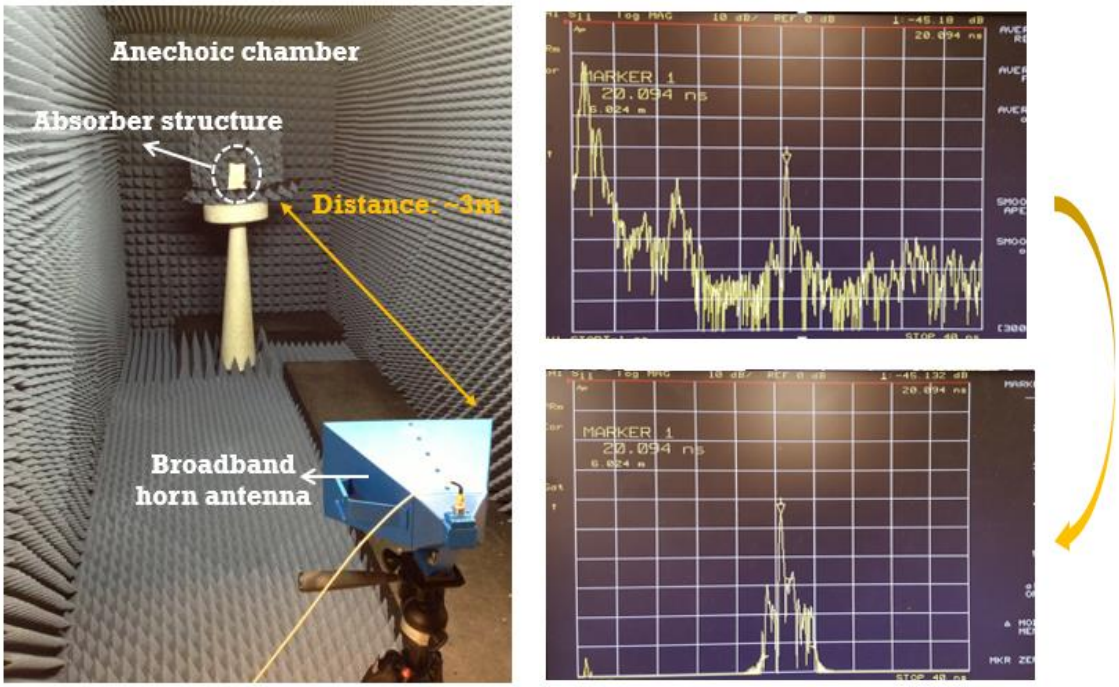


(a) (b)

Figure 2.12. (a) Measurement set-up (b) Time gating in vector network analyzer.

The absorber was measured by using a HP 8720B network analyzer that covers the range of 0.13–20 GHz, and two broadband horn antennas in a microwave anechoic chamber, as shown in Figure 2.12. As shown in Figure 2.12(b), the peak reflection is obtained, and then the maximum peak is remained by using bandpass time gating in vector network analyzer. The wire grid mesh ground plane can act as the metal plane at the microwaves. The fabricated structure shows absorption greater than 90% is in the frequency range of 5.8-12.2GHz and the bandwidth is 71.1% of center frequency. Figure 2.13 shows the measured absorptions for different polarizations of the incident wave. The optical transmittance of total structure is more than 62% as shown in Figure 2.11(b). Due to the symmetric pattern of bow-tie structure, the absorption is almost polarization-

independent. The polarization angle ($\phi$) is defined as the angle between the electric field and x-axis.

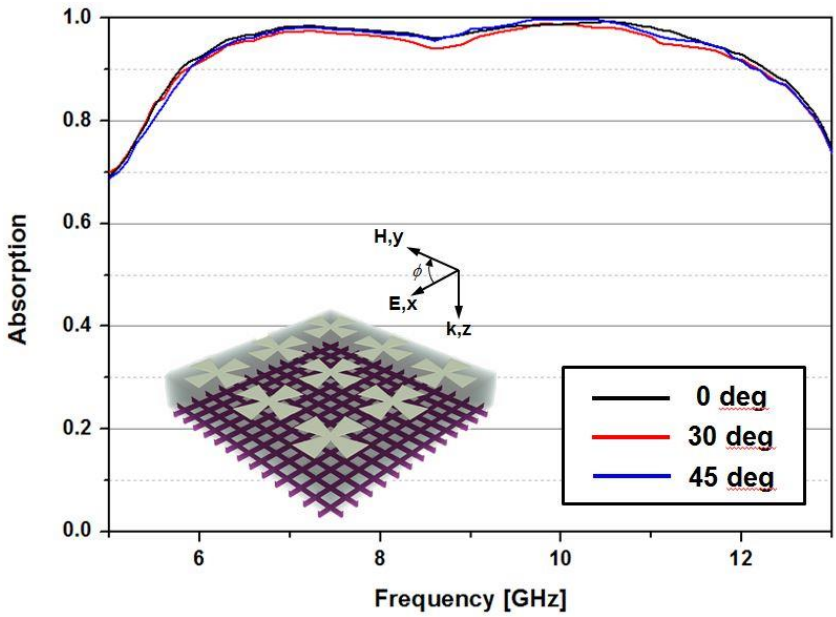


Figure 2.13. Measured absorptions at different polarization angle $\Phi$.(0, 30, and 45 deg).

Figure 2.13 shows the measured absorption according to the polarization. As the $\phi$ increases, the absorption magnitudes and resonance frequencies of the absorber are nearly unchanged for different polarizations (0, 30, 45 deg) of the normal incident wave, demonstrating polarization-independence of the absorber structure. Figure 2.14(a) shows the HFSS model of two unit cells based on bow-tie structures. Due to the Master/Slave boundary pairs, the model represents infinitely periodic structure. Figure 2.14(b) shows the simulated absorption according to the different incident angles (0˚, 20˚, 50˚, 60˚, and 70˚). As the incident angle increases, the absorption peak at high frequency is shifted. The absorption above 90% is achieved up to 54˚ of the incident angle as shown in Figure 2.14(b).

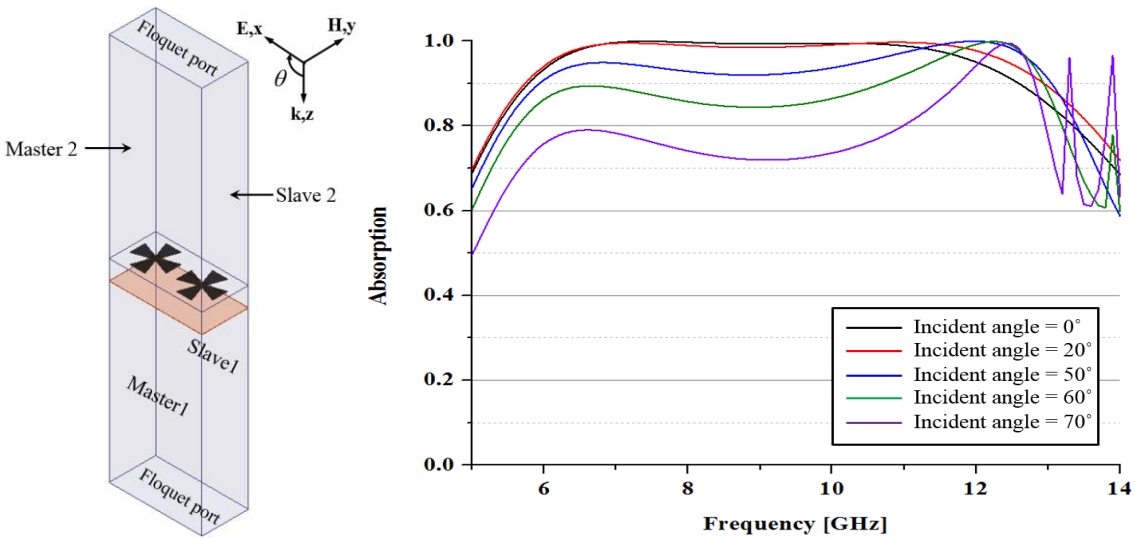


(a) (b)

Figure 2.14. (a) Ansys HFSS simulation model of two unit cells. (b) Absorption according to the different incident angles (0˚, 20˚, 50˚, 60˚, and 70˚).

## 2.7 Multi-layered Ultra Broadband Absorber

Finally we discuss methods to further increase the absorption bandwidth. Based on the principle discussed above, even greater bandwidth can be obtained by merging multiple resonances with overlap spectra. In order to achieve new resonances, bow-tie resonators having different geometric parameters can be inserted in the dielectric spacer as intermediate layers. In such a structure, each layer generates two resonant frequencies by the similar principle. By adding patterned structures having the different lengths at thickness of $t_1$, $t_1+t_2$, and $t_1+t_2+t_3$ respectively, different resonances can be obtained to increase the bandwidth. For example, a 3 layer absorber is designed as shown in Figure 2.15(a). This structure avoids the alignment of the patterned bow-tie structures in each layer as shown in Figure 2.15(b). As shown in Figure 2.15, the resonant fields are less affected by the presence of the neighboring layers. In the simulation, the bow-tie resonators

in the 1st, 2nd, and 3rd layers from the ground plane are modeled with the sheet resistances of $20\Omega/sq$, $20\Omega/sq$, and $25\Omega/sq$ respectively.

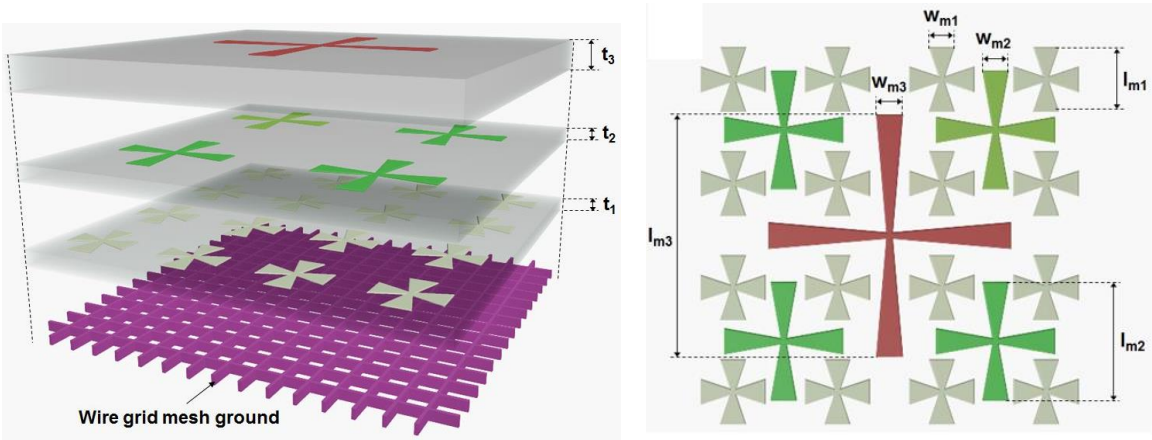


(a) (b)

Figure 2.15. Configuration of the multi-layer absorber structure (a) Perspective view (b) Top view.

Since the absorption peaks are located close to each other, the frequency range needed to achieve absorption above 90% is 3.8-19.2GHz and, therefore the bandwidth of the 3 layer absorber is enhanced to 133.9% of the center frequency, as shown in Figure 2.16. The metal mesh structure used in our structure not only provides optical transparency but also increased resistance that is needed for the broadband application. To reduce fabrication costs and time of our structure, large area of such flexible absorbers can be fabricated in roll-to-roll platform using the recently developed photo roll lithography [29, 30], facilitating practical applications. With further development, we anticipate numerous applications of such transparent and broadband absorbers in the future, e.g. zero-reflected power over a wide bandwidth for better aircraft stealth performance.

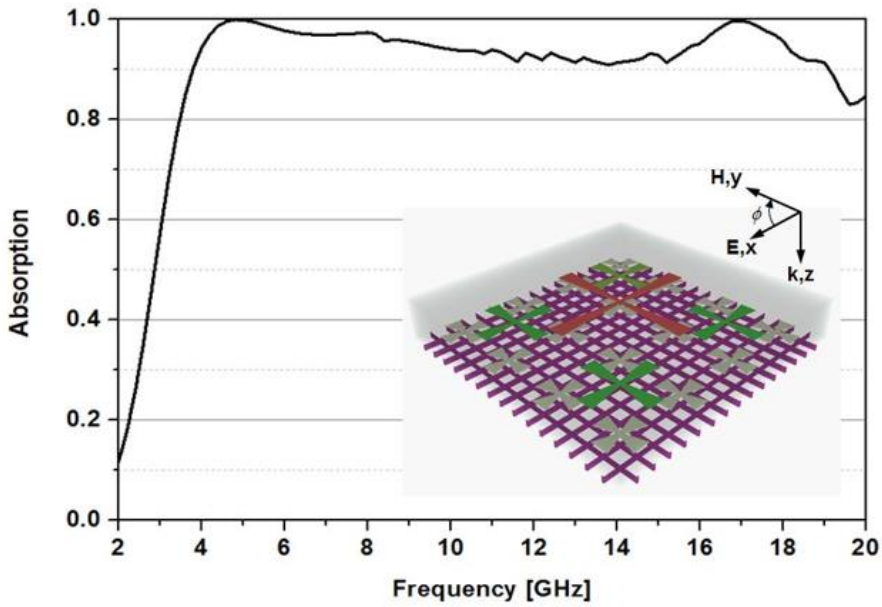


Figure 2.16. Simulated absorption. ($W_{m1}$=1.6m, $W_{m2}$=2.2mm, $W_{m3}$=2.8mm, $l_{m1}$=5.1mm, $l_{m2}$=10.8mm, $l_{m3}$=19.4mm, $t_1$=2.4mm, $t_2$=2.2mm, and $t_3$=4mm).

## 2.8 Conclusion

In conclusion, the two absorption peaks are the result of energy flow and loss in different positions of the absorber. Importantly, these peaks can be adjusted by changing the width and length of the bow-tie structure respectively. Figure 2.6 shows that as the width of bow-tie increases from 1mm to 4mm, the absorption peak at low frequency is shifted to the lower frequency range in response to the increased coupling between the neighboring bow-tie structures. Thus, the bandwidth needed to achieve more than 90% absorption can be extended by increasing the $w_1$. The spectral overlap of the two selected absorption bands broadens the absorption bandwidth. In addition, owing to simple periodically symmetric patterned structures, the absorber is independent to the polarizations of the incident wave.

# Chapter 3

# Semi-Transparent and Flexible Mechanically Reconfigurable Electrically Small Antennas Based on Tortuous Metallic Micromesh

## 3.1 Introduction

Recently, wearable technologies that aim to monitor person's wellness or assist people with diseases have attracted considerable interest. For wearable applications, a variety of sensors, antennas, electronic circuits, and storage systems have been developed. Not only should the wearable devices be small and light, but they should also be able to communicate with other electronic devices. However, the antennas and battery are heavy and take up a large amount of space in the system. In order to produce more compact and lighter system, antenna integrated with a rectifying circuit can be employed to harvest RF energy eliminating the need for the battery. Thus, a radio frequency antenna plays a significant role in the wearable system.

The antennas for wearable applications should be able to be stretched, folded, and twisted. A lot of flexible antennas, which are fabricated on a flexible copper-clad laminate, have been researched [31, 32]. One challenge with using a flexible substrate is that the

mechanical stability of the metal pattern and rigidity of the substrate are not sufficient for wearable gadgets. To address this issue, stretchable antennas have been developed that use a liquid metal such as mercury and eutectic gallium indium alloy (EGaIn) [33-37]. Although liquid metal antennas are mechanically tunable and have high degrees of stretchability, the use of the liquid metal presents a challenge with regard to integration with other system components (e.g. rectifying circuit and RF amplifier). A further challenge is that the antenna may fail to operate properly due to the leakage of the liquid metal if the sealing layer for the liquid metal is even slightly torn or has small holes. Alternative to using liquid metal antennas is the textile-based antenna using metal-coated polymer fibers (e-fibers) [38, 39]. To create such antenna, the conductive textile surface was embroidered to form the antenna. However, because the e-fiber used in these antennas is not stretchable, they are difficult to use for frequency-tunable applications. A further drawback is that the efficiency of this antenna tends to be lower because of electrical contact loss between the e-fibers and the high roughness of the textile.

In order to realize reconfigurable antenna, various mechanisms such as a switch and varactor diode have been employed. Many reconfigurable antennas with electrical switches (e.g. RF MEMs switch, pin diode, MEMs capacitor, and varactor diode) have been developed by interconnecting the adjacent segments of the antenna elements [40]. For RF-MEMs switch and pin diode, the reconfigurability is limited due to the discrete nature of the switch [41-43]. In addition, since varactor diodes and MEMs capacitor provide variable capacitance according to the voltage bias, continuous ranges of frequency reconfigurability of the antenna are obtained [44, 45]. However, in order to operate the switches, a large RF bias network is needed and the switches suffer from nonlinear effect and parasitic

parameters. On the other hand, mechanical tunability could be exploited because it is linearly tunable over a wide range of frequency band and does not require a bias network [46-48]. Furthermore, optical transparency is desirable to meet the space requirement of the wearable devices for practical applications (e.g. transparent smartphone and contact lens display) [49]. Thus, the transparent antenna is intended for the wearable electronics or implantable medical devices where it can be easily camouflaged. In order to provide the optical transparency and electrical conductivity, graphene, nano-particle based electrodes and ITO films have been studied for decades. However, studies have shown that due to the low conductivity, relatively thick layers are needed in order to operate efficiently in the desired radio frequency range. In addition, ITO film is rigid and brittle and therefore not suitable for wearable applications.

This chapter describes a new method for fabricating transparent and stretchable radiofrequency small antennas by using stretchable micromesh structures. These antennas are smaller and lighter than the conventional antennas. Size reduction is achieved by using the zeroth-order resonant (ZOR) property [50]. The antennas consist of a series of tortuous micromesh structures, which provides a high degree of freedom for stretching when encapsulated in elastomeric polymers and is optically transparent. Accordingly, the structure can undergo mechanical deformation such as stretching, folding, or twisting without breakage. These antennas can be stretched up to 40% in size without breaking and easily return to their original shape after the force is removed. According to the increase in the tensile strain, the resonant frequency of the antennas is almost linearly reconfigurable from 2.94 GHz to 2.46 GHz. In addition, they are optically transparent due to the large openings in the mesh and the optical transmittance have increased under high strains.

Therefore, the proposed antennas could be used for the applications such as reconfigurable antennas, antennas for transparent and curved spaces, and wearable sensors.

## 3.2 Mechanically Reconfigurable Antenna Design

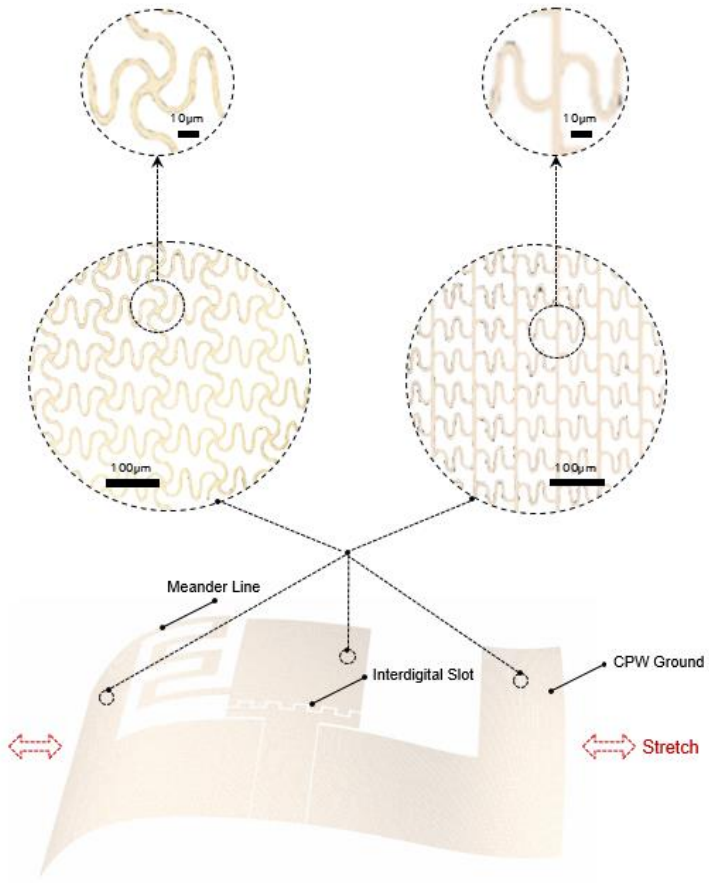


Figure 3.1. The configuration of transparent and mechanically reconfigurable antenna.

Figure 3.1 shows a transparent and stretchable compact zeroth-order resonant (ZOR) coplanar waveguide (CPW)-fed antenna. The antenna consists of the metallic patch, shorted meander line, interdigital slot, and CPW ground. In order to be stretchable and optically transparent, we replace the uniform metallic patches in the traditional antenna configuration with a tortuous wire micromesh design. It can be replaced without loss of

performance since the period of the mesh are roughly smaller than $\lambda_0/1100$ [51], where $\lambda_0$ is free space wavelength.

### 3.2.1 Zeroth-order Resonant Antenna Theory Based on Composite Right-handed/Left-handed(CRLH) Transmission Line(TL)

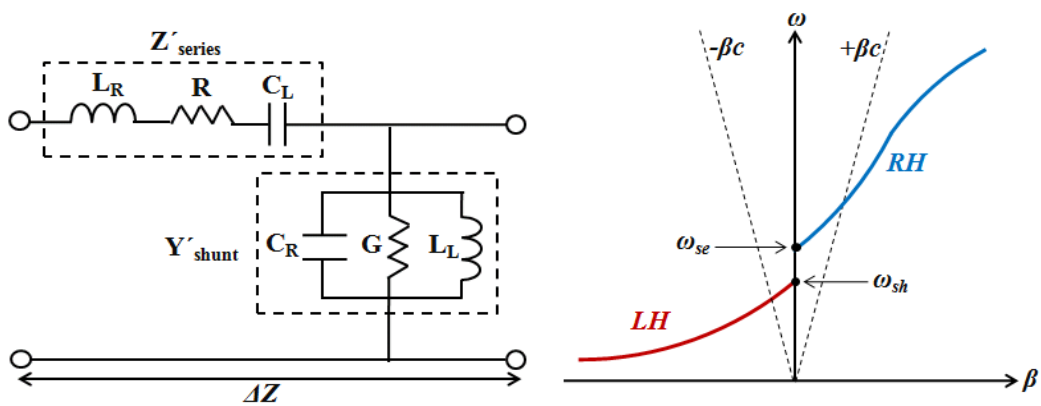


(a) (b)

Figure 3.2. (a) Equivalent circuit model of the CRLH unit cell (b) Dispersion curve of the CRLH unit cell

A general CRLH TL is composed of series capacitance ($C_L$) and inductance ($L_R$) as well as a shunt capacitance ($C_R$) and inductance ($L_L$), as shown in Figure 3.2. It is designed in a periodic configuration by cascading $N$ unit cells. The immittances of a lossy CRLH TL are given by

$$Z'_{series} = R + j\left(\omega L_R - \frac{1}{\omega C_L}\right) \tag{3.1}$$

$$Y'_{shunt} = G + j\left(\omega C_R - \frac{1}{\omega L_L}\right) \tag{3.2}$$

where $R$ and $G$ are the series resistance and shunt conductance of the lossy CRLH TL, respectively. The series and shunt resonant frequencies are given by

$$\omega_{se} = \frac{1}{\sqrt{L_R C_L}} \quad rad/s \tag{3.3}$$

$$\omega_{sh} = \frac{1}{\sqrt{L_L C_R}} \quad rad/s \tag{3.4}$$

Thus, the complex propagation constant ($\gamma$) and characteristic impedance ($Z_C$) are

$$\gamma = \alpha + j\beta = \sqrt{Z'_{series} Y'_{shunt}} \tag{3.5}$$

$$Z_C = \sqrt{\frac{Z'_{series}}{Y'_{shunt}}} = \sqrt{\frac{L_L}{C_L}} \sqrt{\frac{(\omega/\omega_{se})^2 - 1}{(\omega/\omega_{sh})^2 - 1}} \tag{3.6}$$

Because the CRLH TLs have periodic boundary conditions, the Bloch-Floquet theorem can be applied and its dispersion relation is determined by

$$\beta(\omega) = \frac{s(\omega)}{\Delta Z} \sqrt{\omega^2 L_R C_R + \frac{1}{\omega^2 L_L C_L} - \frac{L_R C_L + L_L C_R}{L_L C_L}} \tag{3.7}$$

where $s(\omega)$ and $\Delta Z$ are a sign function and the differential length, respectively.

$\omega_{se}$ and $\omega_{sh}$ can be unequal in the dispersion diagram of the unbalanced LC-based CRLH TL, as shown in Fig. 3.2(b). At these resonant frequencies, where $\beta = 0$, an infinite wavelength can be supported. According to the theory of the open-ended resonator with the CRLH TL, its resonance occurs when

$$\beta_n = \frac{n\pi}{l} (n = 0, \pm 1, ..., \pm(N-1)) \tag{3.8}$$

where $l$, $n$ and $N$ are the physical length of the resonator, mode number, and number of unit cells, respectively. When $n$ is zero, the wavelength becomes infinite and the resonant frequency of the zeroth-order mode becomes independent of the size of the antenna, while the shortest length of the open-ended resonator is one half of the wavelength. Thus, an antenna with a more compact size can be realized.

As shown in Fig. 3.2(b), two resonant frequencies, $\omega_{se}$ and $\omega_{sh}$, with $\beta = 0$ for the unbalanced CRLH TL are observed with a matched load. Considering the open-ended TL, where $Z_L = \infty$, the input impedance ($Z_{in}$) seen from one end of the resonator toward the other end is given by

$$Z_{in}^{open} = -jZ_c \cot(\beta\ell) \overset{\beta\to 0}{\approx} -jZ_c \frac{1}{\beta\ell}$$

$$= -j\sqrt{\frac{Z'_{series}}{Y'_{shunt}}}\left(\frac{1}{-j\sqrt{Z'_{series}Y'_{shunt}}}\right)\frac{1}{\ell} = \frac{1}{Y'_{shunt}\,\ell}$$

$$= \frac{1}{Y'_{shunt}(N\Delta z)} \tag{3.9}$$

where $Y'_{shunt}$ is the admittance of the CRLH unit cell.

Since, from Eq. (3.9), the input impedance of the open-ended resonator is equal to $1/N$ times $1/Y'_{shunt}$ of the unit cell, the equivalent $L$, $C$, $G$ values are equal to $L_L/N$, $NC_R$, and $1/NG$, respectively. Regardless of $N$, the resonant frequency of the $N$ cascaded open-ended ZOR circuit is determined by the resonant frequency originating from the shunt LC tank ($Y'_{shunt}$). Thus, the open ended ZOR antenna's resonant frequency is given by Eq. (3.4), resulting in depending only on the shunt parameters of the unit cell.

Considering that the open ended resonator is only dependent on $Y'_{shunt}$ of the unit cell, the average electric energy stored in the shunt capacitor, $C_R$, is given by

$$W_e = \frac{1}{4}\left|V^2\right| NC_R \tag{3.10}$$

and the average magnetic energy stored in the shunt inductor, $L_L$, is

$$W_m = \frac{1}{4}\left|I_L\right|^2 \frac{L_L}{N} = \frac{1}{4}\left|V\right|^2 \frac{N}{\omega^2 L_L} \tag{3.11}$$

where $I_L$ is the current through the inductor.

Because resonance occurs when $W_m$ is equal to $W_e$, the quality factor can be calculated as follows:

$$Q = \omega \frac{(average \quad energy \quad stored)}{(energy \quad loss/second)}$$

$$= \omega_{sh} \frac{2W_m}{P_{loss}} = \frac{1/NG}{\omega_{sh}(L_L/N)} = \frac{1/G}{\omega_{sh} L_L}$$

$$= \omega_{sh}(1/NG) \cdot NC_R = \omega_{sh}(1/G)C_R$$

$$= \frac{1}{G}\sqrt{\frac{C_R}{L_L}} \tag{3.12}$$

### 3.2.2 CPW-fed Inductor-Loaded Zeroth-Order Resonant Antenna

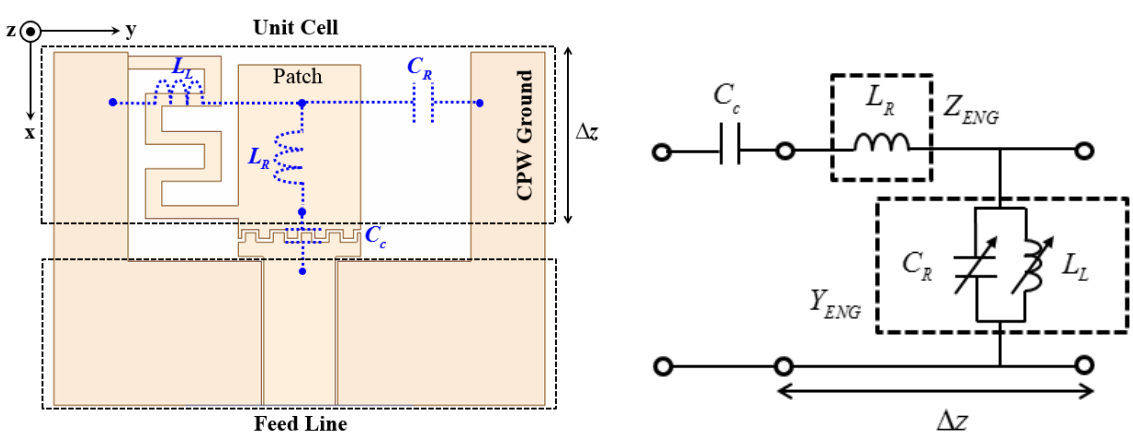


(a) (b)

Figure 3.3. (a) The unit cell of epsilon negative (ENG) meta-structured transmission line (MTL) (b) Equivalent circuit model of ZOR antenna

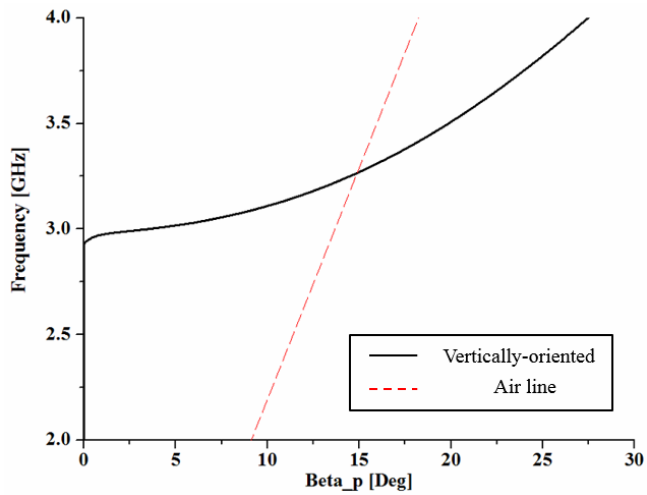


Figure 3.4. Dispersion disagram of the unit cell

Figure 3.3(b) depicts an infinitesimal circuit model for the lossless unit cell of ENG MTL model which is represented as the combination of a per-unit length series inductance ($L_R$), and a shunt capacitance ($C_R$), and a per-unit length shunt inductance ($L_L$). The shunt components of the unit cell are obtained from the shunt capacitance between the top patch and CPW ground, and a shunt inductance of the shorted meander lines as shown in Figure 3.3(a). In addition, the $L_L$ and $C_R$ include additional inductance and capacitance formed by the tortuous metal micromesh. The coupling capacitance ($C_c$) created by an interdigital capacitance in the equivalent circuit model of ZOR antenna is introduced and responsible for only impedance matching. Given that only shunt components ($Y_{ENG}$) of the unit cell determine the resonant frequency of the open-ended resonator, the average electric energy and the average magnetic energy are stored in the shunt capacitor ($C_R$) and the shunt inductor ($L_L$), respectively. From an infinitesimal circuit model for the lossless unit cell of

epsilon negative (ENG) meta-structured transmission line (MTL) model, the effective permeability and permittivity of the MTL materials are obtained as

$$\varepsilon_{ENG} = \frac{Y_{ENG}}{j\omega} = C_R - \frac{1}{\omega^2 L_L} \tag{3.13}$$

$$\mu_{ENG} = \frac{Z_{ENG}}{j\omega} = L_R \tag{3.14}$$

where Z and Y are the per-unit length impedance and admittance, respectively [50, 52, 53]. If the frequency band (ω) is smaller than $1/\sqrt{L_L C_R}$, the ENG MTL has positive permeability and negative permittivity so that it has single negative stopband. The ENG has the unique characteristic of an infinite-wavelength wave at the boundary of passband and stopband. Therefore, zeroth-order resonance occurs when the MTL has zero permittivity. Based on the open-ended structure, the resonant frequency of the mechanically reconfigurable antenna based on ENG MTL is determined by

$$\omega = \frac{1}{\sqrt{L_L C_R}} \quad [1/s] \tag{3.15}$$

where $L_L$ is the inductance of shorted meander line and $C_R$ is the capacitance between the metallic patch and CPW ground respectively as shown in Figure 3.3(a). It indicates that the ZOR frequency is determined only by the shunt inductance and capacitance and therefore independent of the physical length of the resonator. Thus, a small antenna based on the zeroth-order condition is implemented and the resonant frequency of the antenna can be controlled with applied mechanical force. Figure 3.4 illustrates the dispersion diagram for the proposed unit cell. It is based on the S-parameters obtained from the driven mode simulation results. Since this antenna is realized by the inductor-loaded unit cells, the

dispersion diagram only shows the phase delay characteristic. Therefore, the negatice resonance is effectively eliminated while maintaining the zeroth-order resonance.

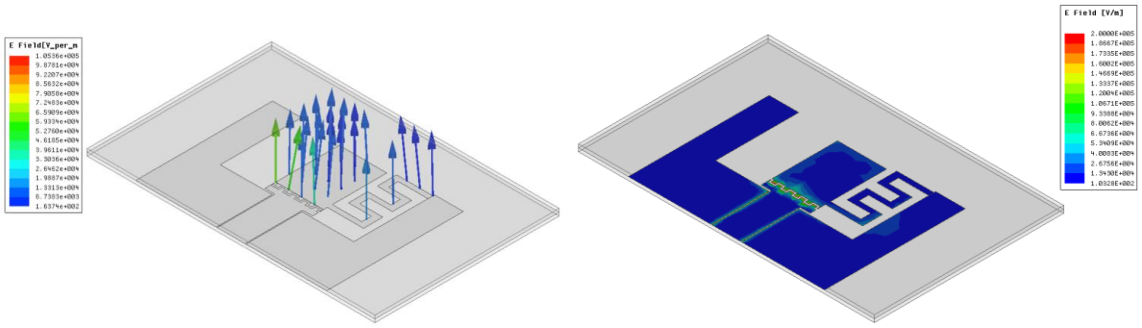

(a) (b)

Figure 3.5. Electric field (a) Vector distribution on the antenna (b) The magnitude of electric field at zeroth-order mode

The structure based on the CPW-fed zeroth order resonant property had been verified. As shown in Figure 3.5(a), the electric field distribution of the zeroth-order resonant antenna is in-phase. At the zeroth-order resonant frequency, the resonant condition is independent of the aperture dimension. Figure 3.6 shows the magnitude of electric field at zeroth-order mode. Since the magnitude of the electric field in the interdigital slot is more dominant than others, the interdigital slot makes the main contribution ot the antenna radiation pattern. In general, both microstrip and CPW resonant antennas radiate from slots. In Ref. [52], the microstrip ZOR antenna's radiation mechanism is same as well. The constant magnetic loop current source is generated by the constant E-field distribution in four slots. Although the proposed CPW ZOR antenna is similarly radiating from slots, the dominant magnetic current source is one slot which is located at the feeding line. The other magnetic current sources from three slots are weaker because the signal and ground planes are far away. Accordingly, this antenna looks like an ideal magnetic dipole rather than a

magnetic loop. As a result, the E-plane and H-plane of the proposed antennas become yz-plane and xz-plane by duality, respectively. Generally, the discontinuity in CPW structure makes less radiation than the microstrip. The asymmetric antenna has more discontinuity than symmetric antenna. Therefore, the efficiency of asymmetric antenna is lower because of the coupled slot mode as well as the small electrical size.

Figure 3.6 clearly demonstrates that the resonant frequencies remain almost constant as the aperture dimension is increased. In conventional resonant antenna, it is obvious that the resonant frequency is decreased as its size is increased.

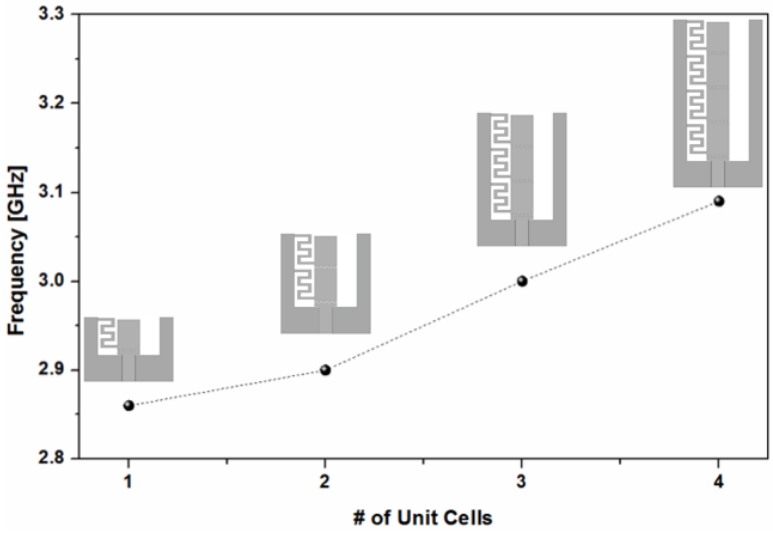


Figure 3.6. The relationship between frequency and the number of unit cells

### 3.2.3 Analysis of Symmetric and Asymmetric CPW-Fed ZOR Antennas

Since our proposed antenna has electrically finite ground plane and an unbalanced structure, CPW-fed ZOR antennas that consist of asymmetric and symmetric structures as shown in Figure 3.7 are studied for the effects of finite ground plane and unbalanced structure in this Chapter. Figure 3.7(a) represents the one unit cell of symmetric antenna. Figure 3.7(b) and 3.7(c) show the CPW-fed ZOR antenna using two asymmetric and

symmetric unit cells, respectively. Since the resonant frequency are determined from the shunt inductance and capacitance, three antennas have the different operating frequencies. The measured return loss are plotted in Figure 3.8.

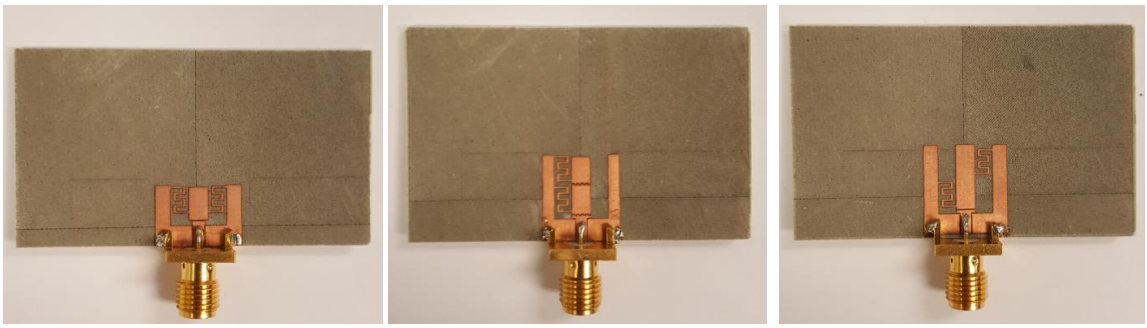

(a) (b) (c)

Figure 3.7. CPW-fed ZOR antennas using (a) one symmetric unit cell (b) two asymmetric unit cell (c) two symmetric unit cells

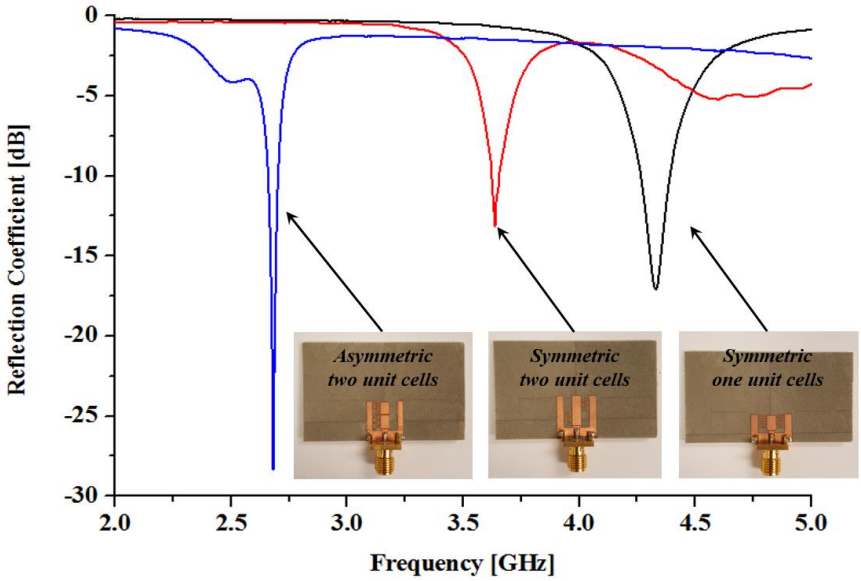


Figure 3.8. Return losses for (a) one symmetric unit cell (b) two asymmetric unit cell (c) two symmetric unit cells

The proposed design is validated using a large ground plane and balanced structures as shown in Figure 3.9(a) [54]. First of all, a large ground plane is added on the CPW ground of the proposed antenna and measured by a vector network analyzer. The resonant

frequency of the antenna with a large ground plane are slightly different from those of the same antenna on a finite ground plane. Figure 3.9(b) shows the measured reflection coefficient for the CPW-fed ZOR antenna with and without larger ground planes. As the ground size becomes larger, the effect from the cable is reduced.

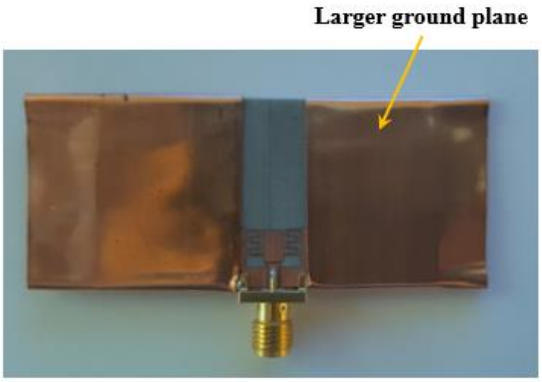


(a)

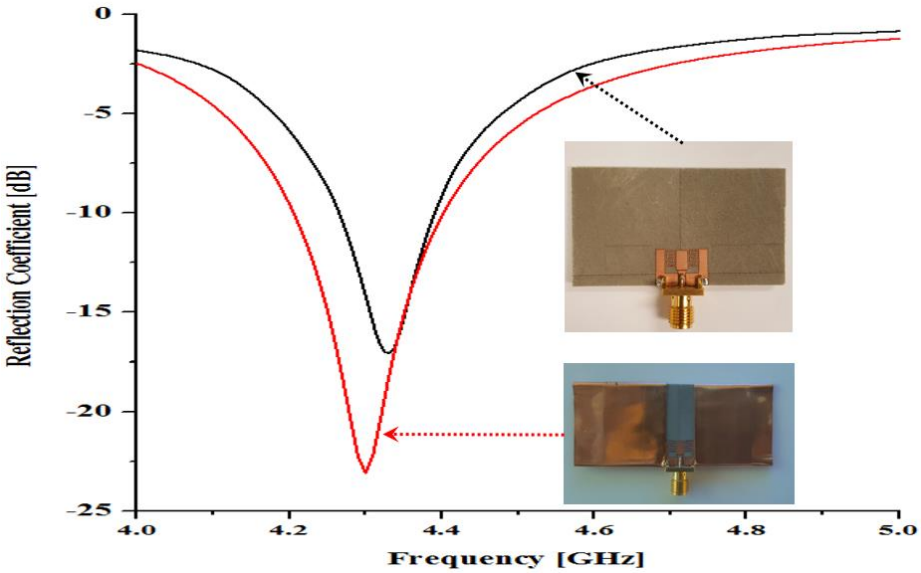


(b)

Figure 3.9. (a) CPW-fed ZOR antenna with larger ground planes (b) Measured return loss for the CPW-fed ZOR antenna with and without larger ground planes.

## 3.3 The Orientation of Meander Line

In addition, to obtain the change the inductance ($L_L$) by applying mechanical means, the vertically oriented meander line is used than the horizontally oriented meander line in our antenna as shown in Figure 3.3(a)

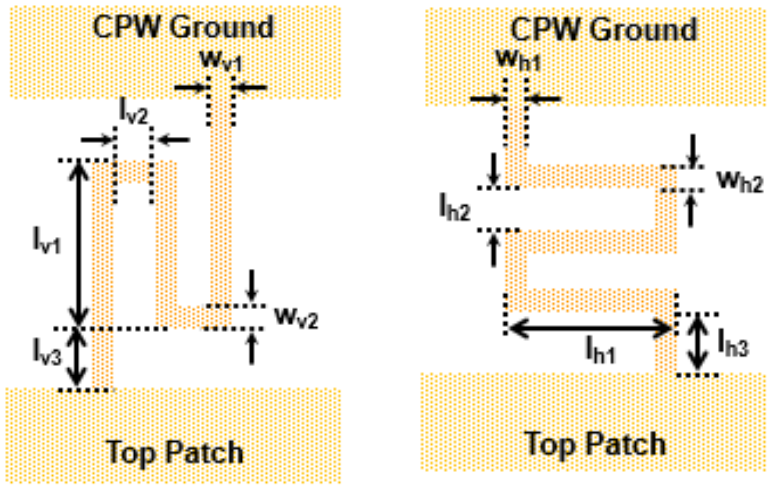


(a) (b)

Figure 3.10. Simulated and measured transmission spectra of individual colors (blue, green, and red) at normal incidence.

Figure 3.10(a) and (b) show the meander-shape inductors positioned in a vertical and a horizontal orientations, respectively. The meander line is connected between the metallic patch and CPW ground as shown in Figure 3.3(a). It can be modeled as an equivalent inductor because it is considered as shorted transmission line. In order to realize the meander line, the tortuous meshed conductors are orthogonally placed. The vertically-oriented meander line has longer conductors with length $l_{v1}$ and width $w_{v1}$ in the direction of force and shorter conductors with length $l_{v2}$ and width $w_{v2}$ in the perpendicular direction of force as shown in Figure 3.6(a). Appropriate self and mutual inductance values are determined by the optimal arrangement of the size parameters. According to the applied tensile strains, the parameters of the vertically-oriented meander line are changed. The $l_{v1}$

and $w_{v2}$ increases, and $l_{v2}$ and $w_{v1}$ decreases. The horizontally-oriented meander line consists of shorter conductors with length $l_{h2}$ and width $w_{h1}$ in the direction of force and longer conductors with length $l_{h1}$ and width $w_{h2}$ in the perpendicular direction of force as shown in Figure 3.10(b).

When the tensile strain is applied in the vertical direction as shown in Figure 3.11, the $l_{h2}$ and $w_{h2}$ of the horizontally-oriented meander line increases, but $l_{h1}$ and $w_{h1}$ decreases. The inductances and capacitances are extracted from a circuit (Advanced Design System 2015) and full wave (Ansoft HFSS 15) simulator regarding the meander line shapes and applied tensile strains.

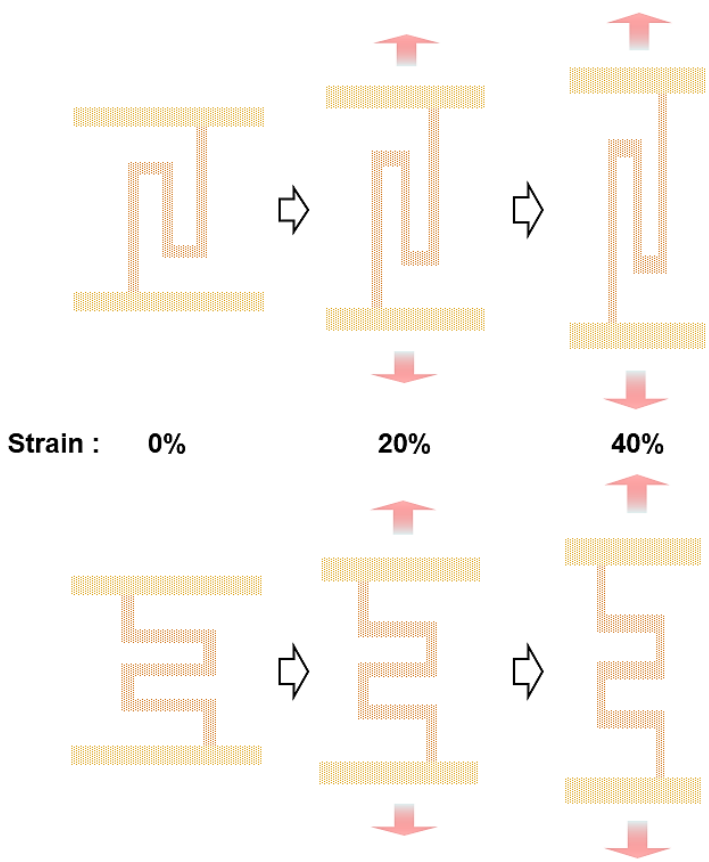


Figure 3.11. The change of vertical-oriented and horizontal-oriented meander lines with the different tensile strains.

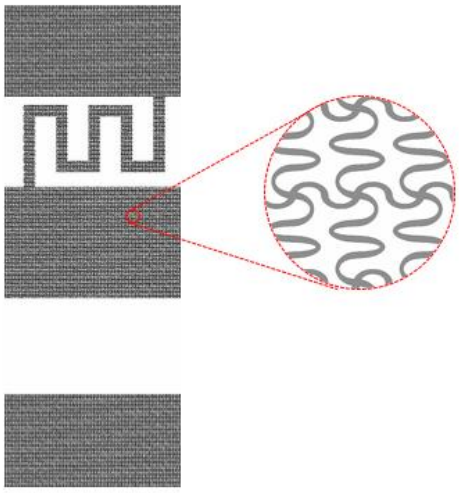

Figure 3.12. Unit cell based on micromesh to extract equivalent circuit parameters

To obtain the circuit parameters containing the parasitics, the micromesh is drawn directly in the simulation as shown in Figure 3.12, and the values of the circuit parameters ($L_L$, $C_R$) are extracted from the S-parameters [55]. Our procedure is as follows: First, a shorted meander line with CPW ground consists of a shunt capacitance and inductance (CR, LL) and it is simulated in Ansys HFSS. Its s-parameter is used in order to extract equivalent circuit parameters. The series inductance ($L_R$) can be modeled by the Π network. The shunt inductance ($L_L$) and capacitance ($C_R$) can also be modeled by the T network. Those Π network and T network are analyzed to find the corresponding parameters for the equivalent circuit. For a 2-port network, the impedance parameters and admittance parameters are determined. Thus, the admittance and impedance matrices are obtained for the $C_R$, $L_L$, and $L_R$. The extracted parameters are tabulated in Table 3.1. Thus, it shows the influence of the orientation of the meander lines according to the different strains. Apparently when a tensile strain is applied along the vertical direction, the inductance of the vertically oriented meander line varies much more than that of the horizontally oriented

meander line. Thus, the vertically oriented meander line is preferred to obtain widely mechanically tunable resonances.

TABLE 3.1 INDUCTANCE OF MEANDER LINE ACCORDING TO THE ORIENTATIONS AND TENSILE STRAINS

| | TENSILE STRAIN (%) | 0% | 20% | 40% |
|---|---|---|---|---|
| MTL with vertically oriented meander line | Inductance (nH) | 6.323 | 7.519 | 8.271 |
| | Capacitance (pF) | 0.451 | 0.434 | 0.493 |
| | Resonant frequency (GHz) | 2.98 | 2.78 | 2.49 |
| MTL with horizontally oriented meander line | Inductance (nH) | 6.198 | 6.287 | 6.497 |
| | Capacitance (pF) | 0.452 | 0.463 | 0.456 |
| | Resonant frequency (GHz) | 3.01 | 2.95 | 2.92 |

## 3.4 The Design of Tortuous Micromesh

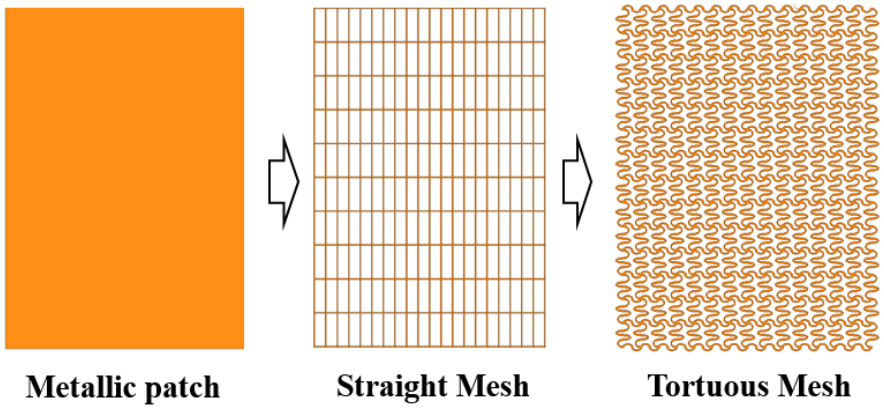


Figure 3.13. Topology modification for transparent and stretchable micromesh.

The metallic patch of the antenna in Figure 3.13 can be replaced with micromesh to be optically transparent as well as to have good electric conductivity. The electric current distribution on an ordinary metallic patch at the zeroth-order mode is not changed, but the

thin wires of micromesh introduce an additional inductance per unit length. In addition, the straight wires are wound to be stretchable so that it effectively lead to the miniaturization of the linear dimension of the micromesh.

TABLE 3.2 COMPARISON BETWEEN METALLIC PATCH, STRAIGHT MESH, AND TORTUOUS MESH

| | Metallic Patch | Straight Mesh | Tortuous Mesh |
|---|---|---|---|
| Effective conductivity (S/cm) | $5.96\times10^5$ | $2.24\times10^4$ | $3.28\times10^4$ |
| 10 dB bandwidth (%) | 2.93 | 3.53 | 3.43 |
| Resonant frequency (GHz) | 2.940 | 2.943 | 2.941 |
| Realized Gain (dB) | -3.04 | -3.72 | -3.46 |
| Radiation efficiency (%) | 85.4 | 79.1 | 81.4 |

The antennas based on the metallic patch, straight mesh, and tortuous mesh are simulated in Ansoft HFSS and the 10 dB bandwidth, resonant frequency, and realized gain are tabulated in Table 3.2. Although tortuous mesh has slightly broader 10dB bandwidth and lower gain because of low conductivity, it still has same resonant frequency compared with the metallic patch. Typically the metallic patch and straight mesh are easily broken with a small tensile strain because of the high Young's modulus (117GPa) of the copper. In order to withstand the applied tensile strains, the strength applied to the mesh should be lower than the yield strength. Prior to the yield point, the material can be deformed elastically and will return to its original shape when the applied stress is removed. To decrease the stress applied to the mesh as well as to increase the structural ability of mesh

to be elongated, the straight lines of straight mesh are wound [56]. Thus we used a tortuous metallic mesh rather than the straight wire mesh. Specifically, we designed two types of tortuous meshes which we then used to fabricate our structurally stretchable and optically transparent antenna.

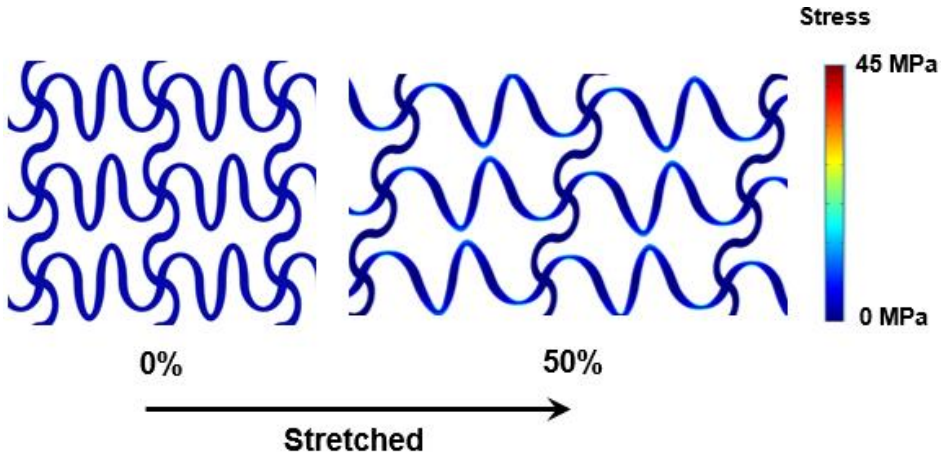


Figure 3.14. Mechanical simulation of micromesh

Figure 3.14 shows the mechanical simulation of meshes with Comsol 4.4. The results are based on finite element method (FEM) and it presents the calculated stress localized in the stretched mesh. In our designed tortuous micromesh the maximum stress is 44.14 MPa with 50% of tensile strain. Because of this characteristic, our tortuous micromesh is more durable than straight line mesh in terms of the tensile strain. To make the tortuous wire micromesh structure, it is worth noting that the narrower wires tend to be more stretchable than the wider ones. Thus, to withstand the applied tensile strains, the geometrical parameters of the unit cells of the micromesh are optimized and determined.

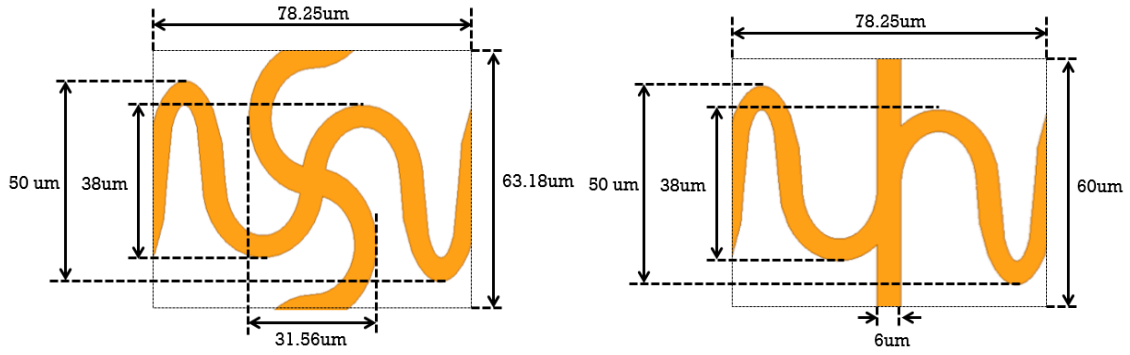


(a) (b)

Figure 3.15. (a) Unit cell of micromesh using both tortuous wires in horizontal and longitudinal direction (tortuous micromesh design 1) (b) Unit cell of micromesh using tortuous wire in horizontal direction and straight wire in longitudinal direction one tortuous (tortuous micromesh design 2).

Figure 3.15(a) and (b) show the zoom-in view of the unit cells of our two tortuous wire micromesh designs. In order to avoid multiple contacts at the intersection of the wires, the first tortuous mesh is designed by mixing tortuous wires with tortuous lines with a period of 78.25μm in the horizontal direction and a period of 63.18μm in the longitudinal direction, respectively, as shown in Figure 3.15(a). Between the intersections in the horizontal direction, the wires with a high undulation amplitude and a short period are connected to increase the ability of wires to elongate. The second tortuous mesh is designed with a tortuous line with a period of 78.25μm in the horizontal direction and the straight line with a period of 60μm in the longitudinal direction, as shown in Figure 3.15(b). In addition to the elongation, another advantage of using the tortuous mesh is that the linear dimension along the current path of the antenna is reduced while at the same time maintaining good optical transparency and electrical conductivity.

TABLE 3.3 RELATIONSHIP BETWEEN OPTICAL TRANSPARENCY AND ELECTRICAL CONDUCTIVITY IN TERMS OF THE DESIGN OF MICROMESH

| # OF WAVY LINE | 2 | 4 | 6 | 8 |
|---|---|---|---|---|
| Micromesh Design & Size | | | 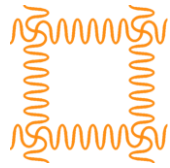 | 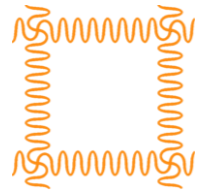 |
| Optical Transparency | 58 % | 74% | 81% | 88% |
| Electrical Conductivity | $3.28\times10^4$ | $1.56\times10^4$ | $1.13\times10^4$ | $8.29\times10^3$ |

Table 3.3 shows the ratios of opening area to total area of micromesh unit cells. Generally optical transparency and electrical conductivity change in opposite directions. In addition, 400μm-thick PDMS has 8% of an additional reflection, and high aspect ratio of metal may make additional scattering. If we use larger period micromesh structure as shown in Table 3.3, the higher optical transmittance can be obtained. Thus, the size of the opening of micromesh can be selected to determine the optical transparency and electrical conductivity requiring to the practical applications.

The figure of merit has been widely used to evaluate the overall performance of transparent conductive electrodes [57-59]. The figure of merit (FoM) is defined as the ratio of the electrical conductivity to optical conductivity ($\sigma_{dc}/\sigma_{op}$) where $\sigma_{dc}$ is the electrical conductivity at DC and $\sigma_{op}$ is the sheet conductivity in the optical frequency range. The larger FoM represents the better performance, and the optical transparency ($T$) is determined by

$$T = \frac{1}{\left(1 + \frac{Z_0}{2R_S}\frac{\sigma_{op}}{\sigma_{dc}}\right)} \tag{2}$$

where $Z_0$ is the free space impedance (377Ω) and $R_S$ is the sheet resistance of the metallic tortuous micromesh. $T$ is typically measured at a wavelength λ=550nm which is the maximum of the human eye luminosity. The FoM of our tortuous micromesh is more than 5k which is much higher than other transparent conductive electrodes [60-63].

## 3.5 Antenna Fabrication and Measurements

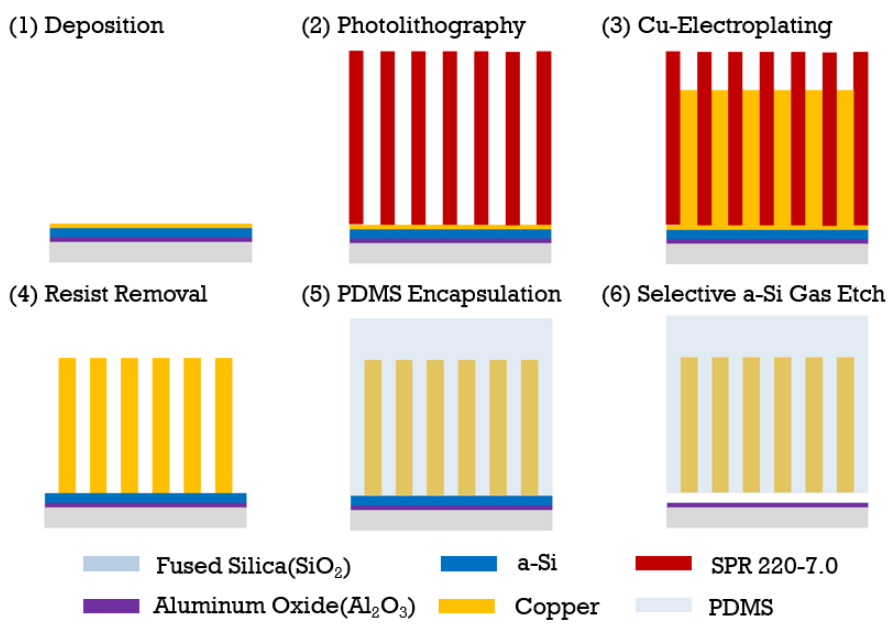


Figure 3.16. The schematic of the fabrication for micromesh.

Figure 3.16 shows the schematic of the fabrication process used to produce the tortuous micromesh antenna. Copper is employed for the antenna because of its excellent conductivity ($59.6\times10^6$ S/m), ductility, low cost, and light weight. A fused silica substrate is first coated with a 150 nm thick a-Si layer deposited by PECVD, which works as a sacrificial layer that is removed later in the fabrication process. A 40 nm Cu film is then

deposited on the substrate to serve as the seed layer for the subsequent Cu electro-plating. The antenna of tortuous micromesh is defined by photo-lithography process. A patterned resist is used as the mask for the Cu plating, which produces a 4.7 μm thick tortuous Cu mesh pattern. After the resist is removed, the Cu mesh is encapsulated by a polydimethyl-siloxane (PDMS) layer, which is flexible and optically transparent. This step also maintains the shape of micromesh as well as protects the metal wire from mechanical damage when the micromesh is stretched. The PDMS and the Cu mesh embedded in it are then separated from the substrate by removing the a-Si layer by applying xenon di-fluoride ($XeF_2$) gas [64]. Finally, another PDMS layer is laminated onto the Cu mesh side to conclude the flexible antenna fabrication, resulting in a total thickness of the PDMS of about 400 μm.

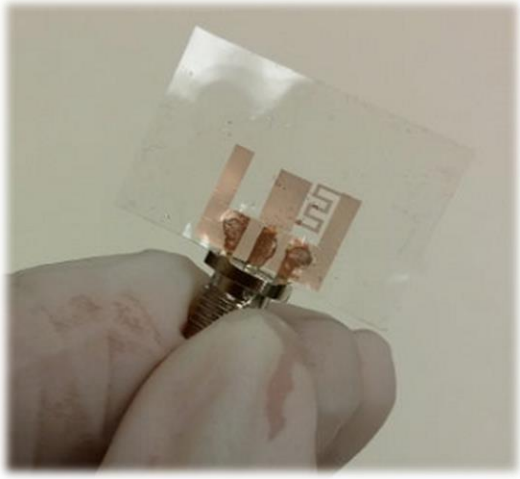

Figure 3.17. The fabricated antenna.

The proposed antenna is fabricated and embedded in a commonly used elastomer PDMS with a relative permittivity of $\varepsilon_r$=2.80 and loss tangent of tan $\delta$= 0.02, as shown in Figure 3.17. The fabricated antenna is connected to a SMA connector. The impedance of the antenna is matched to 50 Ohm. The antenna is measured using a vector network analyzer (Agilent E5071B).

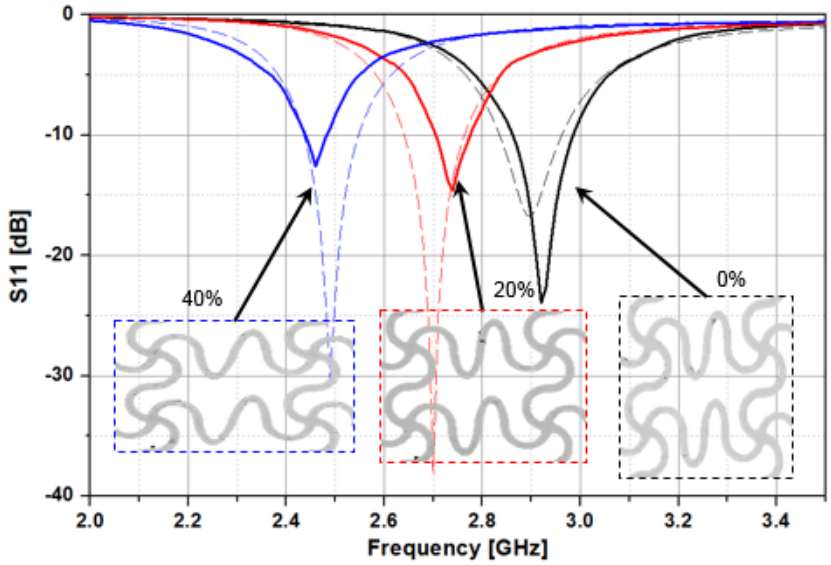


(a)

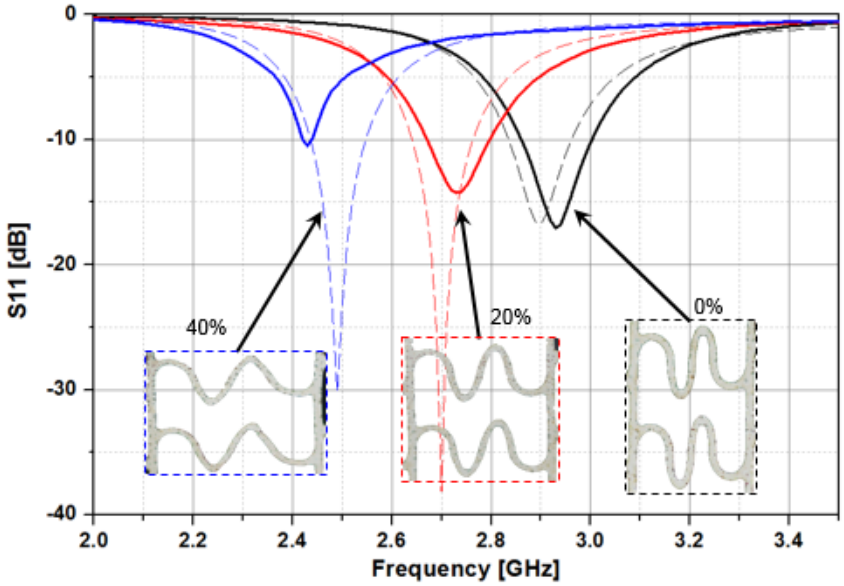


(b)

Figure 3.18. The resonant frequency according to the increase of strains (a) for antenna with both tortuous lines (b) for antenna with only horizontal tortuous line (Solid line : Simulated results, Dashed lines : Measured results).

The actual conductivities of the micromeshes are measured by 4 points probe, and the measured conductivities are used as the effective conductivities in a full wave simulation. Figure 3.18(a) and (b) show the simulated and measured return loss ($S_{11}$) along with the increases in the tensile strains (0%, 20%, and 40%). As the tensile strains are increased, the resonant frequencies of antennas decrease from 2.94 GHz to 2.46 GHz, which shows good agreement between the simulated and measured results. To obtain the different stretchability in the measurement, the mechanical stretching device which consists of the plastic nuts, bolts, and acrylic is used. The bandwidths of the antennas are tabulated in Table 3.4. Although Eq. 3.12 does not consider the impedance matching at the input terminals, it provides an intuitive concept by means of which the bandwidth can be efficiently increased. Generally, ZOR antennas are known to have a narrow bandwidth problem compared to conventional resonant antennas. This is because the Q-factor of a ZOR antenna is only related to $C_R$ and $L_L$. For example, in a microstrip structure, $L_L$ and $C_R$ are realized by the shorting pin (via) and parallel plate between the top patch and bottom ground. Since $L_L$ in a microstrip line (MSL) depends on the length of the via, the microstrip structure limits the value of $L_L$. In addition, since the thickness and size of the substrate determine the capacitance of the parallel plate, the MSL has a large $C_R$. According to Eq. 3.12, the narrow bandwidth is originated from the small $L_L$ and large $C_R$. Therefore, the ZOR antenna in microstrip technology has a narrow bandwidth due to the structural problem. In order to extend the bandwidth of the microstrip structure, a thick substrate with low permittivity is generally utilized. However, this causes fabrication difficulties and reduces the design freedom. Our antennas result in improved bandwidth with degrading the efficiency due to the shunt conductance ($G$).

TABLE 3.4 BANDWIDTH OF PROPOSED ANTENNA

| | Simulated Results | | | Measured Results | | |
|---|---|---|---|---|---|---|
| Applied Tensile Strain | 0% | 20% | 40% | 0% | 20% | 40% |
| 10dB Bandwidth (Design 1) | 4.13% | 4.44% | 4.01% | 4.43% | 4.03% | 0.03% |
| 10dB Bandwidth (Design 2) | 4.17% | 4.07% | 4.06% | 3.78% | 2.19% | 1.61% |

The measured conductivity and thickness of the fabricated micromesh are used to simulate the antenna. The overall area of the radiating aperture is very small and approximately $0.08\lambda_0 \times 0.11\lambda_0 \times 0.004\lambda_0$ (8.32 mm × 11.6 mm × 0.4 mm) at 2.92 GHz. The optical transmittances of the tortuous micromesh structure increase with increased stretching because of the large opening ratio of the mesh, which measures 32-44% in the wavelength range of 400-800nm depending on the level of stretching (i.e. strain ratio) as shown in Figure 3.19.

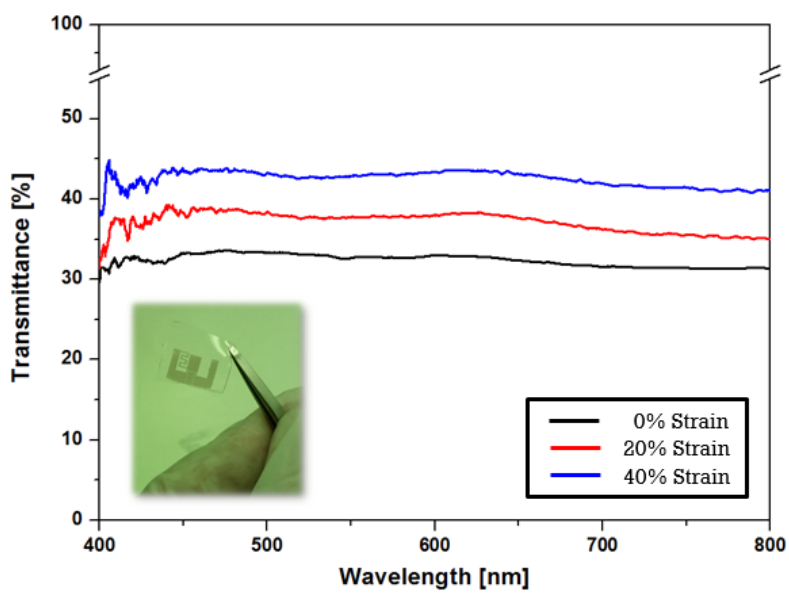

Figure 3.19. The measured optical transmission of the stretchable antenna embedded in PDMS.

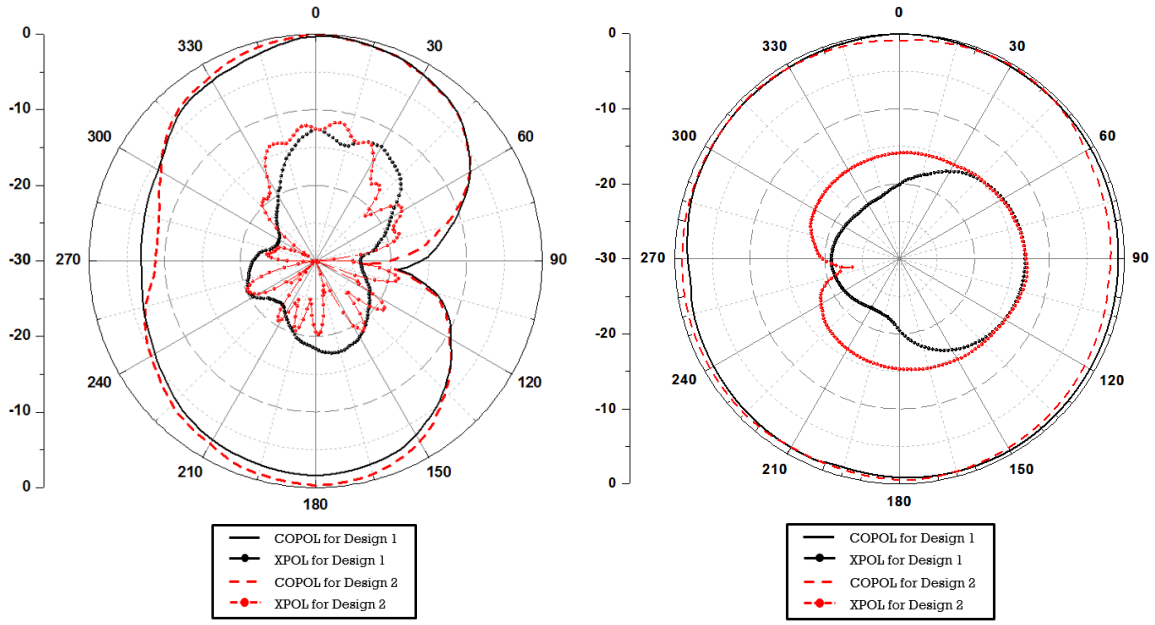


(a) (b)

Figure 3.20. The radiation patterns (a) E-plane (xz-plane) (b) H-plane (xy-plane).

The radiation patterns of the fabricated antenna were measured with the mechanically stretchable device in the anechoic chamber. The stretchability of the antenna is controlled with a mechanically stretchable devices as shown in Figure 3. 21. One side of the mechanically stretchable device is fixed, and the other side is moving to stretch the antenna from 0% to 40%. In order to reduce the unwanted reflections, non-conductive plastic is used to design the mechanically stretchable device. The antenna under test (AUT) is placed on a rotating styrofoam platform in the chamber. The AUT is then connected to a signal generator (Agilent N5183A). A standard horn antenna is connected to a spectrum analyzer (Hewlett Packard 8529L) to measure the received power by using a data acquisition program. By rotating the AUT, the received power is measured by the horn antenna which

allows the radiation patterns to be measured. Combined with the measured values, the antenna gain is calculated using the gain comparison method [65]. In this method, the Friis Transmission formula is utilized to calculate the unknown antenna gains. In this process, the AUT is replaced with a reference horn antenna with a known gain. By comparing the received power of the AUT and the reference antenna, the gain can be calculated.

Figure 3.20(a) and (b) shows the measured radiation patterns on the xz-plane (E-plane) and yz-plane (H-plane) at 2.92GHz. As the tensile strains are increased from 0% to 40%, the measured gains slightly decrease because their effective conductivity are decreased. According to the increase of the tensile strians, the measured gains of the antenna for design 1 have the -0.21dBi, -0.39dBi, and -0.53dBi, respectively. In addition, the measured gains of the antenna for design 2 has the -0.02dBi, -0.14dBi, and -0.29dBi, respectively. As the tensile strain is increased from 0% to 40%, the antenna gain is slightly decreased because the effective conductivity slightly varies from $3.28\times10^4$ S/cm to $3.12\times10^4$ S/cm.

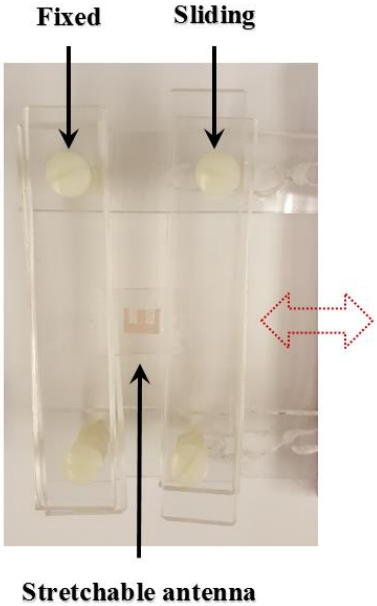


Figure 3.21. A mechanically stretchable device

Figure 3.22 shows the measured radiation patterns at their resonant frequencies (2.46GH, 2.73GHz, and 2.94GHz) in response to the increase of the tensile strain. The radiation patterns of the antenna are not significantly changed by the applied tensile strains. The measured gain of the antennas has the maximum values of -0.21dBi and -0.02dBi, respectively. The overall antenna performances of our antennas are compared with those of previously reported flexible antennas in Table 3.5. Although other antennas in Table 3.4 are flexible, they are not transparent or stretchable. Unlike these other antennas, since our antennas are realized based on the tortuous micromesh, they provide optical transparency as well as structural stretchability. In addition, they can be a smaller size than other flexible antennas because of the use of the zeroth-order mode.

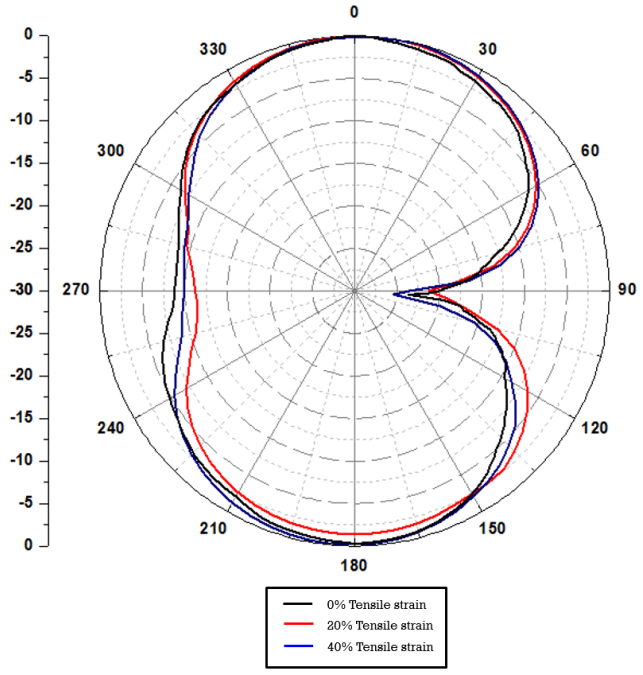


Figure 3.22. The radiation patterns at the resonant frequencies (2.46GH, 2.73GHz, and 2.94GHz) in response to different tensile strains (0%, 20%, and 40%).

Table 3.5. Antenna summary and comparison results for proposed and reference antennas.

| Symbol | THIS WORK | [36] | [39] | [44] |
|---|---|---|---|---|
| Resonant Frequency [GHz] | 2.92 | 3.45 | 2.1 | 2.92 |
| Gain [dBi] | -0.02 | -2.4 | 12.8 | 0.37 |
| Size [$mm^3$] | 8.32 ×11.6 ×0.4 | 40 ×40 ×1 | 153.2 ×122 ×6.35 | 45 ×40 ×1 |
| Metal materials/Substrate materials | Tortuous Cu micromesh / PDMS | EGaIn / PDMS | E-texile / fabric | AgNWs / PDMS |
| Flexible | O | O | O | O |
| Transparent [a)] | O | X | X | X |

## 3.6 Conclusion

In conclusion, we demonstrated a transparent, reversibly deformable, and frequency reconfigurable small antenna by utilizing the tortuous micromesh structures, which provides excellent electric conductivity, flexibility, stretchability, as well as optical transparency. The resonant frequency could be tuned by mechanically elongating the meandering line of the antenna. Such tunable antenna could be potentially used for the transparent, flexible, and stretchable radiofrequency wearable applications.

# Chapter 4

# Ultra-Low Profile Flexible Triple-Polarized Antenna Using Flexible Silver Nanowires and Substrate with High Isolation

## 4.1 Introduction

Wireless communication systems have been developed rapidly in the past decades. Multiple-input–multiple-output (MIMO) technology has been intensively used in modern wireless communication systems to improve system performance. Polarization diversity plays an important role in the MIMO system for mitigating signal impairments caused by the multipath propagation or enhancing performance of wireless communication system [66, 67]. The scatterings or multiple reflections cause multipath interference, where radio signals travel in multiple complicated paths from the transmitter to the receiver, arriving at slightly different time. In addition, the polarization of the propagating radio wave may become diversified. Thus, in order to enhance performance, an antenna requires polarization diversity.

To satisfy such a requirement, various dual-polarized antennas have been studied [68-70]. Dual polarizations is obtained by using two pairs of orthogonal slots which are placed under the radiating patch to excite two orthogonal modes [70]. Patch antenna using cross-shaped slots were used to obtain two orthogonal linear polarization [69]. Moreover,

the bowtie patch antenna with electric dipoles for dual polarizations were designed to produce equal +45 and -45 radiation pattern with low back-radiation [68]. However, those structure becomes thicker due to the use of the air gap and multi-layer structure.

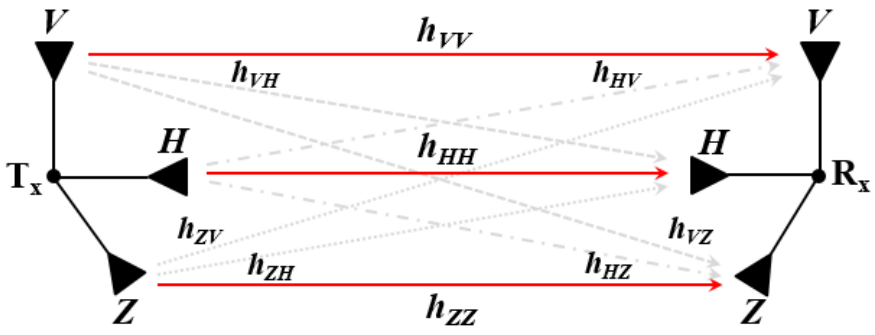


Figure 4.1. The configuration of Triple-polarized antenna system

In order to fully use the polarization diversity characteristic, a single triple-polarized antenna system as shown in Figure 4.1 has been achieved for the triple-polarized MIMO. In [71], the dipole antennas and half-slot antennas are adopted for three port orthogonally polarized antennas. Three mutually perpendicular radiating elements were achieved good isolation and low signal correlation between ports. In order to reduce the profile of the tri-polarized antenna, a disk-loaded monopole was used for the vertical polarization instead of a single monopole [72, 73]. The circular patch antenna for two orthogonal polarizations and a monopole for the third polarization are proposed in [73]. In addition, the slot-coupled microstrip antennas for two orthogonal polarization and the disk-loaded monopole for the third polarization are integrated into one structure so that it reduces the profile of the antenna [72]. In their designs, two orthogonal patch modes were used to realize the broadside pattern, and the monopole mode was used to radiate conical pattern. Although these designs effectively reduce the profile of the antennas, those are not sufficient to be used for the wearable devices.

This chapter proposes an ultra-low profile flexible antenna with tri-polarization characteristic for wearable or MIMO application. To achieve a good impedance matching while maintaining good isolations among the antenna ports, perpendicularly radiating cross-slot antennas and ZOR array antenna are used in the proposed design. Due to the use of ZOR antenna, the vertical polarization is obtained with an ultra-low profile. Since it is designed on the flexible substrate and the silver nanowire is used to realize the metallic vias, the proposed antenna is flexible. A prototype antenna was fabricated and measured. The antenna has an ultra-low profile, high isolation, and the measured results can validate the theoretical simulation.

## 4.2 The Configuration of the Low-profile Tri-polarization Antenna

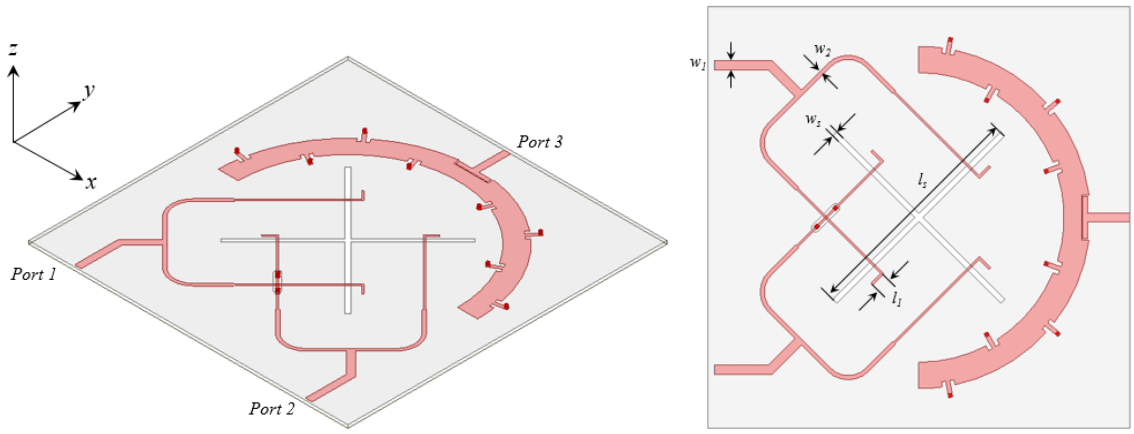


(a) (b)

Figure 4.2. (a) Perspective view of the antenna (shows port assignments and polarization orientation) (b) top view of tri-polarized antenna. (Dimension [mm] of the antenna are: $w_1$ = 1.88, $w_2$= 0.8, $w_s$ = 1, $l_1$ = 3, $l_S$ = 45.72)

A low profile tri-polarization antenna is designed by integrating the cross polarized slot antennas and zeroth-order resonant (ZOR) antenna. The proposed antenna provides

three orthogonal polarizations with good ports isolation, and ZOR antenna is employed for a vertical polarization. The 2 ports orthogonal feed network is used to realize dual linear polarizations, and ports 1 and 2 are fed into the quasi-cross-shaped slot etched on the ground. The cross-shaped slots radiate according to the excitation ports. Since there is a crossing position between microstrip feed lines, the air bridge for feed line is used to provide the isolation between crossed microstrip lines.

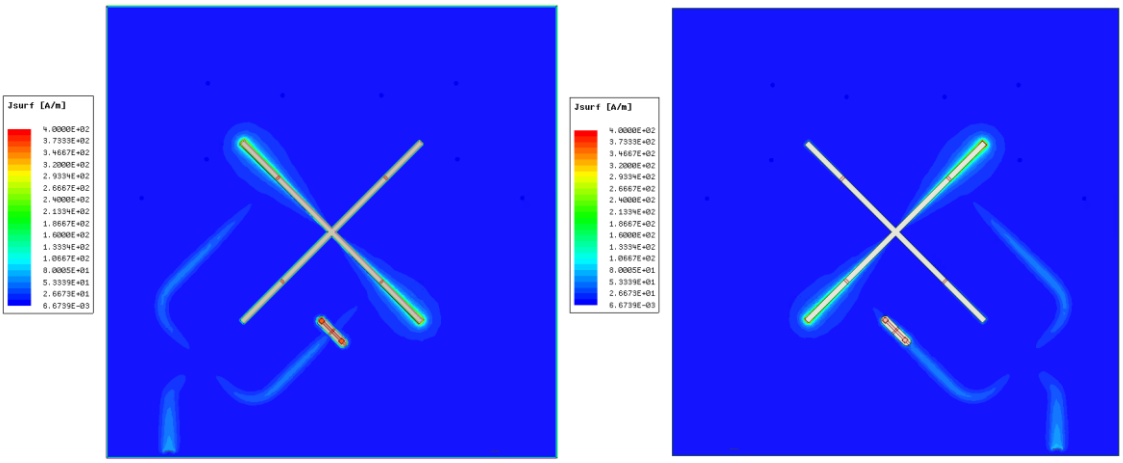


(a) (b)

Figure 4.3. Simulated surface current distribution with different ports being excited: (a) at port1, (b) at port 2

The current distributions are shown in Figure 4.3 when ports 1 and 2 are excited, respectively. The surface currents with port 1 that has been excited is along +45 deg, while it is along -45 deg when port 2 is excited. Thus, two orthogonal polarizations are obtained at the crossed slots and the omni-directional radiation patterns are observed for the same direction at the slot.

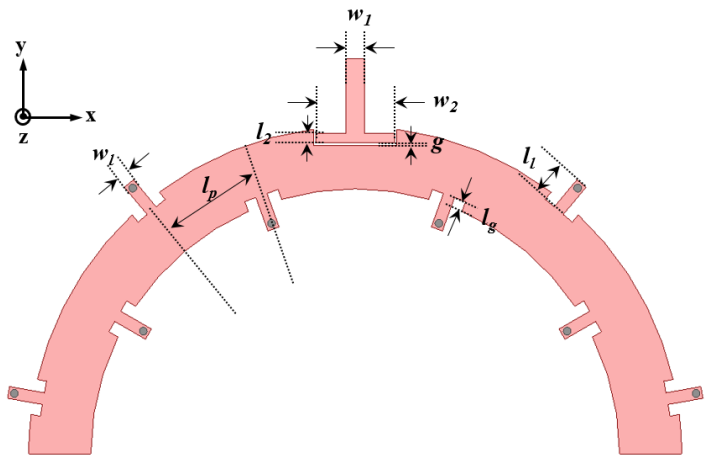


(a)

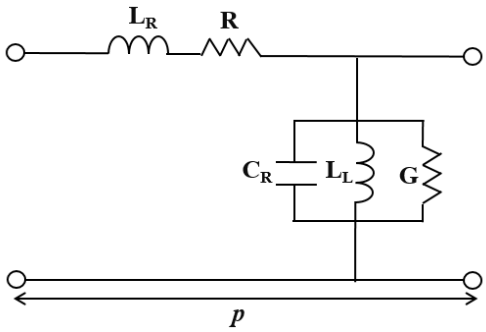


(b)

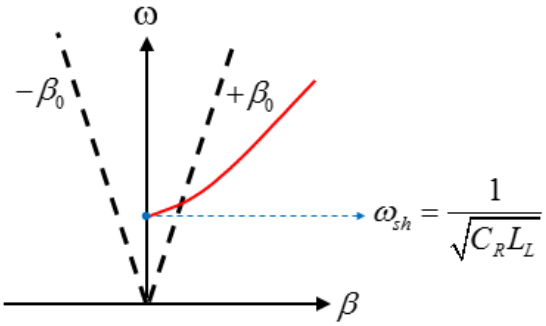


(c)

Figure 4.4. (a) ZOR array antenna (Dimension [mm] of the antenna are: $w_1$ = 1.88, $w_2$= 8, $w_l$ = 1.2, g = 0.2, $l_2$ = 1, $l_l$ = 3.6, $l_g$ = 1, $l_p$ = 10) (b) Unit cell of length *p* (c) Dispersion diagram.

In order to realize the vertical polarization with low-profile characteristics, the ZOR array antenna is designed and integrated with cross polarized slot antennas. A unit-cell of an inductor-loaded TL consists of a series inductor ($L_L$), shunt capacitors ($C_R$) and shunt inductor ($L_L$) as shown in Figure 4.4(b). *R* and *G* are the resistance accounting material losses and the conductance due to dielectric loss of the substrates, respectively. Figure 4.4(a) shows the proposed two elements ZOR antenna array implemented with microstrip

technology. Each of the ZOR elements consists of sequential connected unit cells each of which has inductor-loaded structures to remove the negative modes. For an inductor-loaded unit cell, the propagation constant is given by

$$\beta(\omega) = \frac{1}{p}\cos^{-1}\left(1 + \frac{1}{2}\left(\frac{L_R}{L_L} - \frac{\omega^2}{C_R^2 L_R^2}\right)\right) \tag{4.1}$$

where $p$ is the period of the unit cell. The dispersion diagram of the inductor-loaded TL is plotted in Figure 4.4(c). The only phase delay can occur for the inductor-loaded TL, while the CRLH TL supports both phase advance or phase delay. The input impedance of the antenna is dependent on the number of unit cells and is given by

$$Z_{in} = -jZ_0 \cos(\beta l) \overset{\beta \to 0}{\approx} \frac{1}{jN\left(\omega C_R - 1/\omega L_L\right)} \tag{4.2}$$

where $N$ is the number of unit cells in the resonator and $N=l/p$. As shown in Figure 4.4(a), a ZOR array antenna with two 4 unit cells is designed due to the enhancement of antenna gain. The resonant frequency of the ZOR antenna array is determined by

$$\omega = \frac{1}{\sqrt{L_L C_R}} \quad [1/s] \tag{4.3}$$

where $L_L$ is the inductance of shorted via and $C_R$ is the capacitance between the metallic patch and ground respectively. The electric field distribution of the zeroth-order resonant antenna is in-phase as shown in Figure 4.5. Since the slot antennas has the horizontal electric fields and ZOR antenna has the vertical electric field, they has a good isolation while integrating them closely.

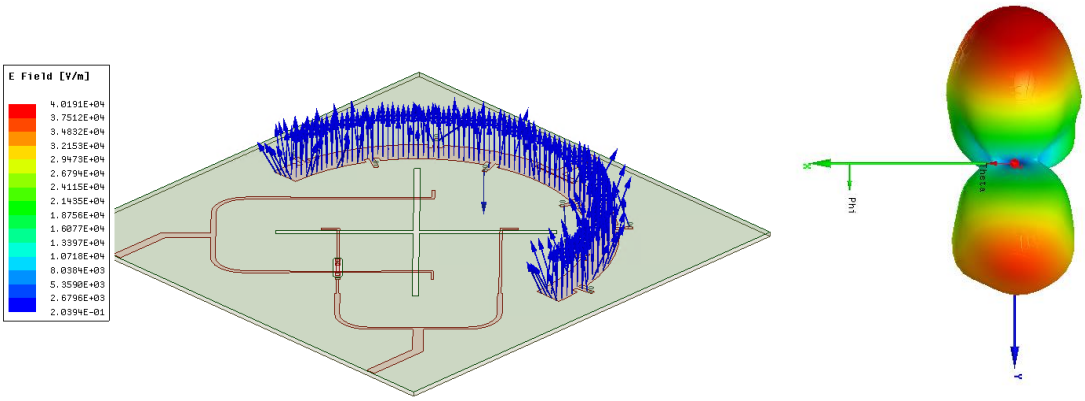


(a) (b)

Figure 4.5. (a) Simulated electric field vector distribution on the ZOR array antenna (b) Simulated 3D radiation patterns

### 4.2.1 The Comparison between Monopole Antenna and ZOR Array Antenna

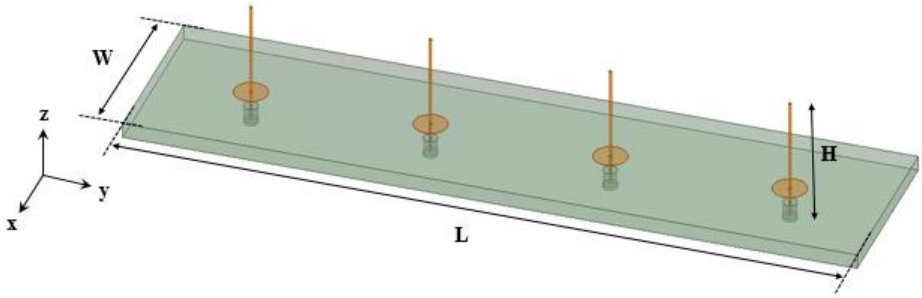


(a)

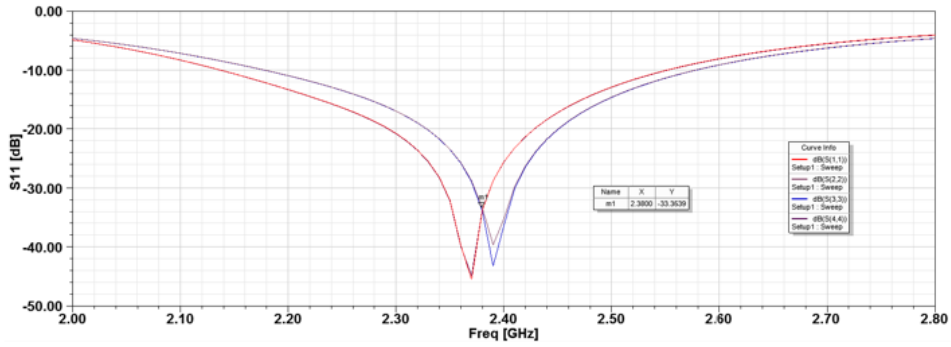


(b)

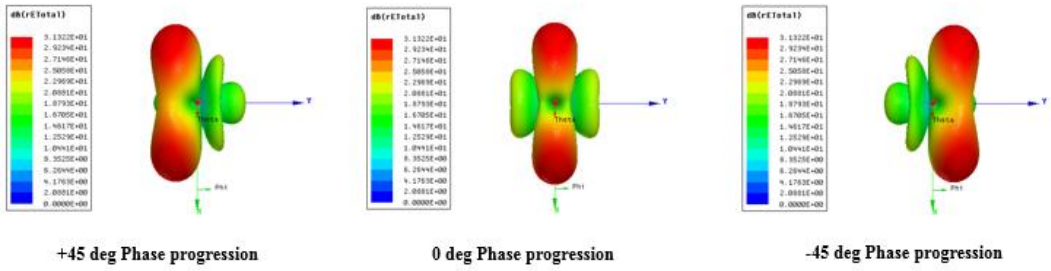


(c)

Figure 4.6. (a) Configuration of monopole array antenna (Dimension: *W*=60mm, *L*=240mm, *H*=41mm) (b) Return loss (c) Radiation patterns in terms of phase progression

This chapter shows the comparison between quarter wave monopole array antenna and ZOR array antenna. In order to realize the monopole array antenna, the four quarter-wave monopole antennas are mounted on a dielectric substrate as shown in Figure 4.6(a). Figure 4.6(b) shows the return loss at four each port. The distance between the antenna elements is 0.47 wavelength in free space compromising a relatively high gain and low side lobes as well as preventing unwanted grating lobes. The direction of maximum radiation is normal to the equi-phase plane. By changing the phase progression among the monopole antennas, the radiating beam can be scanned as shown in Figure 4.6(c).

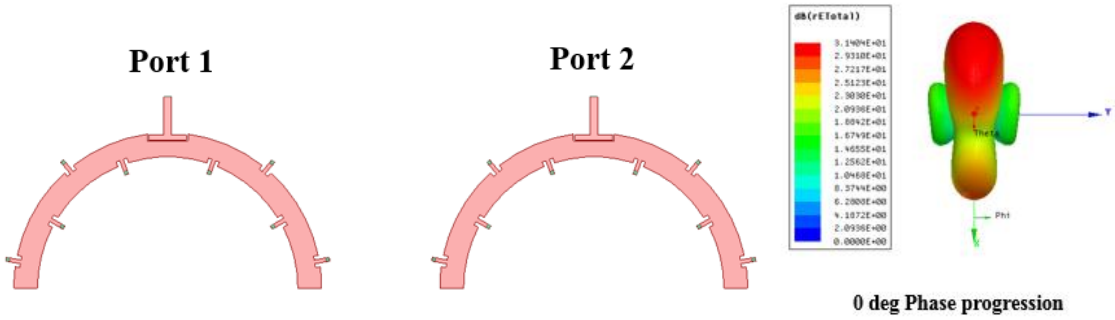


(a) (b)

Figure 4.7. (a) Configuration of ZOR array antenna (b) Radiation pattern

Figure 4.7(a) and (b) shows the configuration of ZOR array antenna with four elements and the radiation pattern, respectively. The radiation pattern is similar to that of monopole array antenna. Thus, the vertical polarization can be obtained with a ultra-low profile characteristic. The radiation pattern is slightly distorted because of coupling and asymmetric ground plane configuration.

## 4.3 Flexible Metallic Via Based on AgNWs

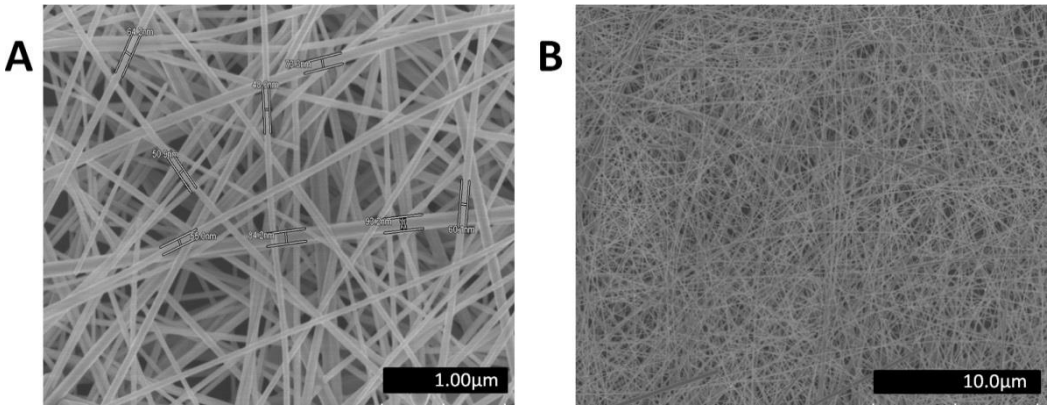


Figure 4.8. The SEM images of uniform, ultralong and thin AgNWs prepared by hydrothermal method at 160°C-22hours reaction.

In order to design the flexible antenna, the flexible substrate and vias based on AgNWs are used. In our laboratory, long silver nanowires of an average diameter 45-65 nm and length greater than 200 µm are synthesized by a simple hydrothermal route [74]. In a typical synthesis procedure, silver nitrate (0.02M, 15ml)(Sigma-Aldrich, 10220), D+glucose (0.12g, 5ml) (Sigma-Aldrich, G8270), Poly (vinylpyrrolidone) (PVP, $M_w$≈40000) (1g, 5ml)(Fisher Sci, BP431) and sodium chloride (0.04M, 15ml)(Fisher Sci, S93361) are prepared in deionized water (DI) as four separate solutions, in a well dissolved form. PVP solution is prepared using magnetic stirring at 65 °C while rests of the solutions

are prepared at normal room temperature. Glucose solution is added to Silver nitrate solution with continuous stirring. After 5 to 10 minutes, PVP solution is added and stirred for 20 minutes until mixed well. Afterwards, sodium chloride solution is injected drop-wise to the above solution with continues stirring until fully dissolved. This turbid hydrosol is added to 50 ml Teflon-lined stainless steel autoclave and heated in oven at 160 $^{0}$C for 22 hours. After that the autoclave is air cooled to room temperature unaided and final product in the form of fluffy gray white precipitate is collected by centrifugation at a speed of 2500 rpm for 60 minutes and washed thrice with distilled water and 3 to 4 times with isopropanol. Final product is dispersed in isopropanol for further use. Every time before centrifugation to remove PVP layer, wires are shaken gently to prevent them from breaking down. SEM images obtained from the as prepared product are shown in Figure 4.8. These images indicate that the sample is composed of almost uniform wires of average diameter 45-65 nm and lengths greater than 200 μm.

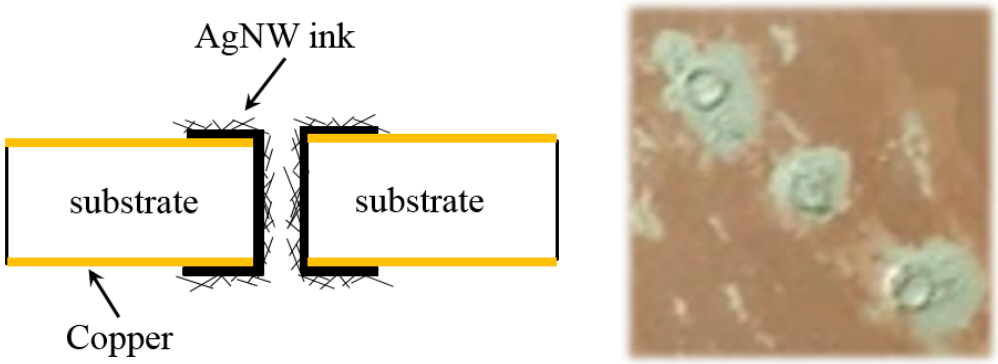


(a) (b)

Figure 4.9. (a) Side view of AgNW via. (b) Fabricated AgNW via on the PCB substrate

In order to build the flexible metallic vias, we drilled holes on the flexible substrate (RT/duroid RO3003) substrate and then inserted the silver nanowires inside the holes as

shown in Figure 4.9(a). Figure 4.9(b) shows the fabricated silver nanowire vias with PCB substrate.

## 4.4 Simulation and Measurement Results

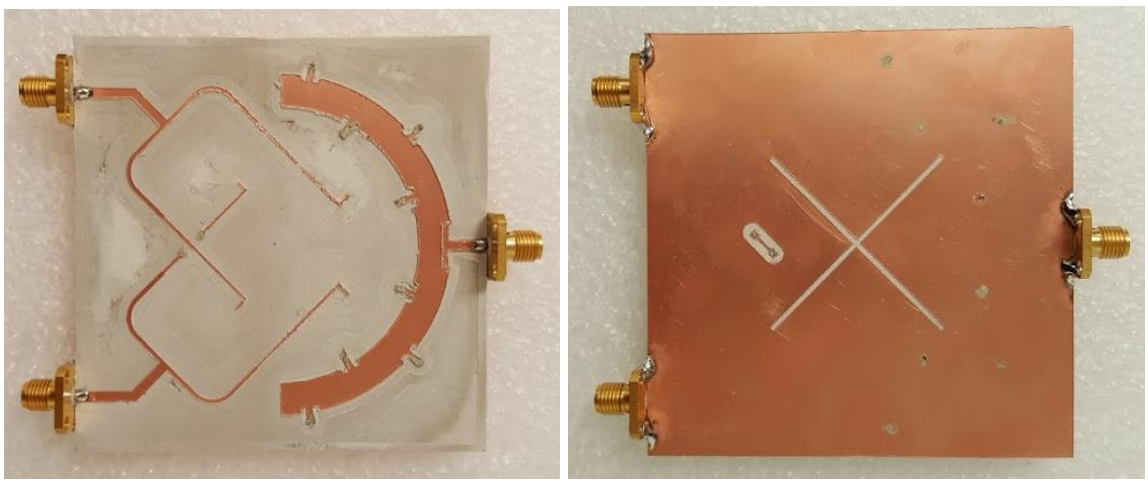

(a) (b)

Figure 4.10. Fabricated the low-profile, flexible tri-polarized antenna using AgNW vias (a) Top view (b) Bottom view

Full wave EM simulation of the tri-polarization antenna with dimension provided in Figure 4.2(a) is carried out. In order to validate our concept a prototype of the antenna is fabricated using a high resolution LPKF milling machine (ProtoMat S103) which ensures the accuracy of the drillings and ultra-fine milling of the design. Moreover, the silver nanowires are used to realize the flexible metallic vias. It is realized on 0.762 mm thickness RT/duroid RO3003 substrate, and we drilled holes on the substrate to build the vias and then inserted the silver nanowires inside the holes. Figure 4.10(a) and (b) show the top view and bottom view for the fabricated the low-profile, flexible tri-polarized antenna using AgNW vias.

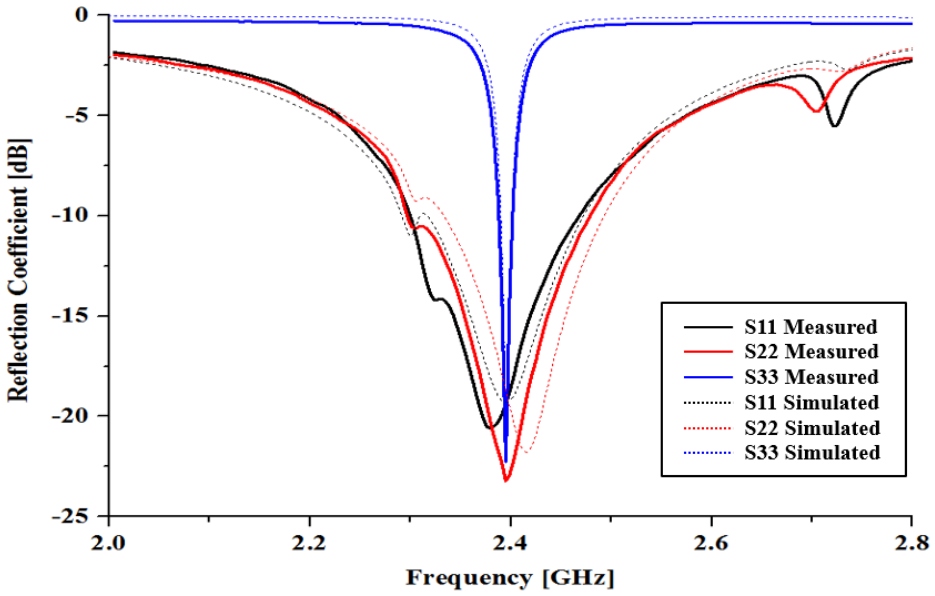


Figure 4.11. Measured and simulated return loss of each port the tri-polarized antenna.

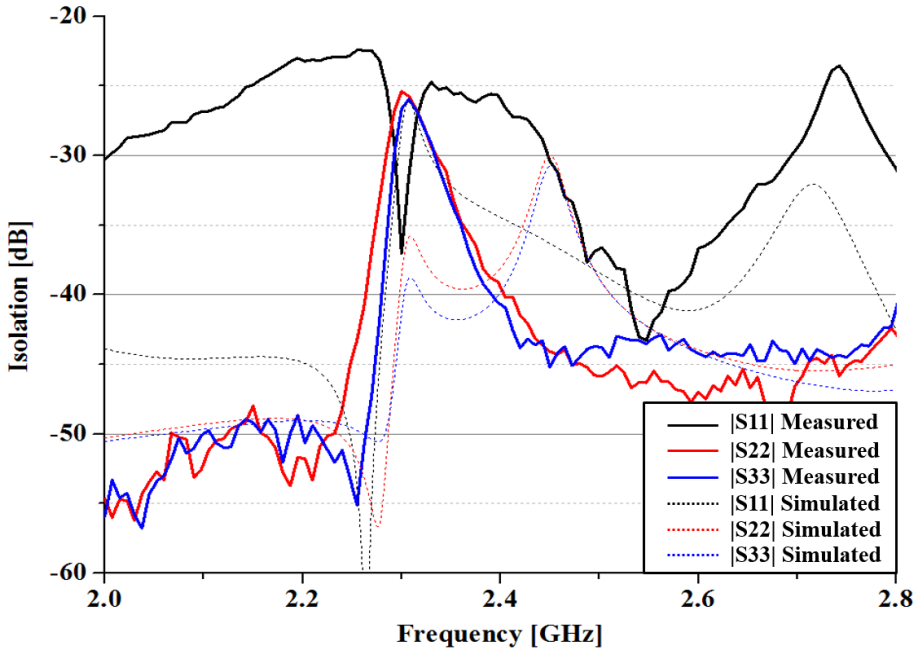


Figure 4.12. Measured and simulated isolation between each two ports of the tri-polarized antenna.

The measurements are carried out and compared with the ones obtained from the simulation. Both S-parameter results are in good agreement although small discrepancy is

observed and can be due to fabrication errors as shown in Figure 4.11 and 4.12. Good impedance matching less than -10dB is achieved and high port-to-port isolations are observed at the resonant frequency. Excellent cross-polarization levels less than 20dB is obtained. The measured and simulated radiation patterns results in the two orthogonal cutting planes (+45deg and -45deg planes) are also illustrated in Figure 4.13. For ports 1 and 2, the good omni-directional patterns are obtained for cross-slot antenna radiation.

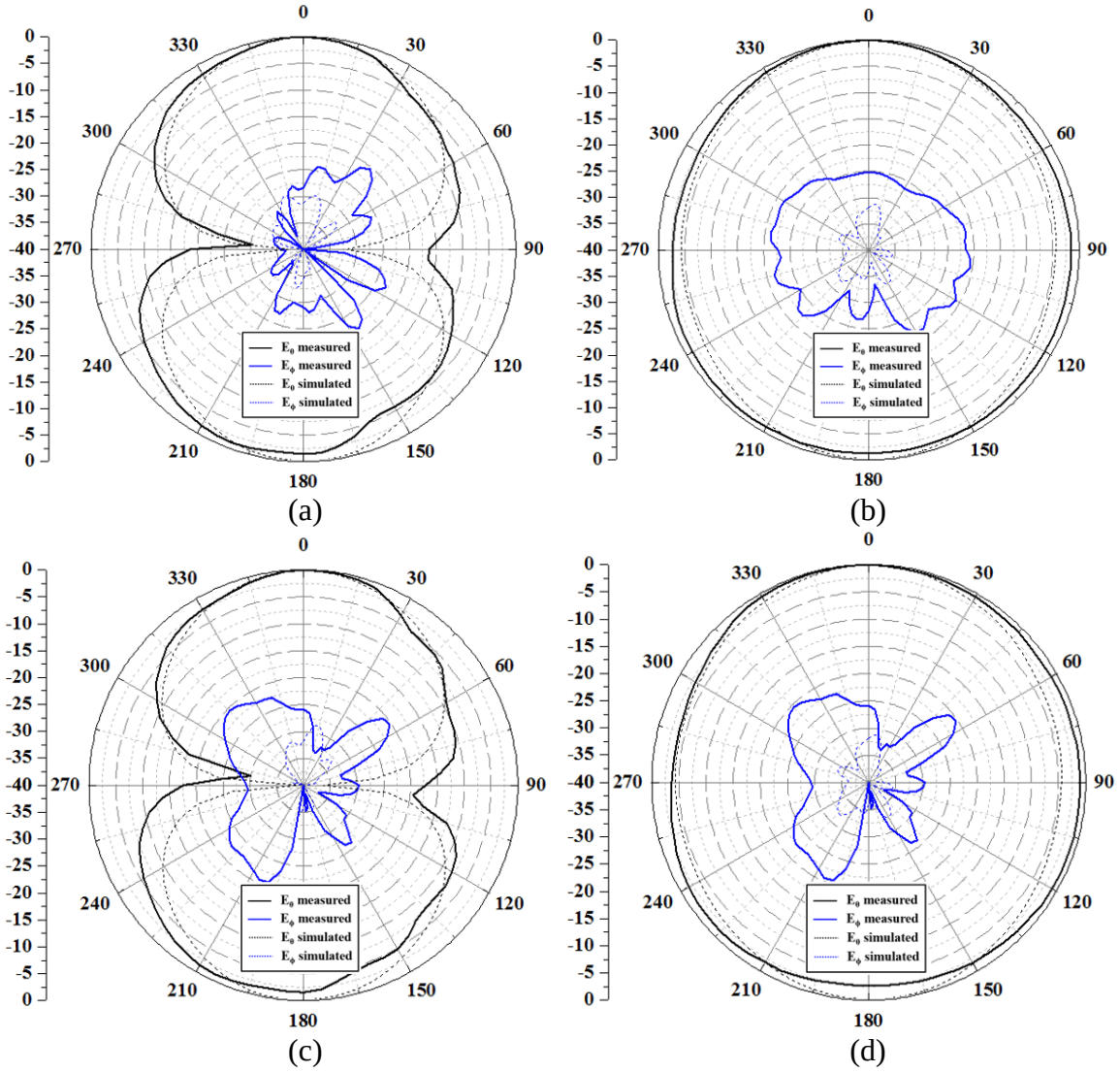

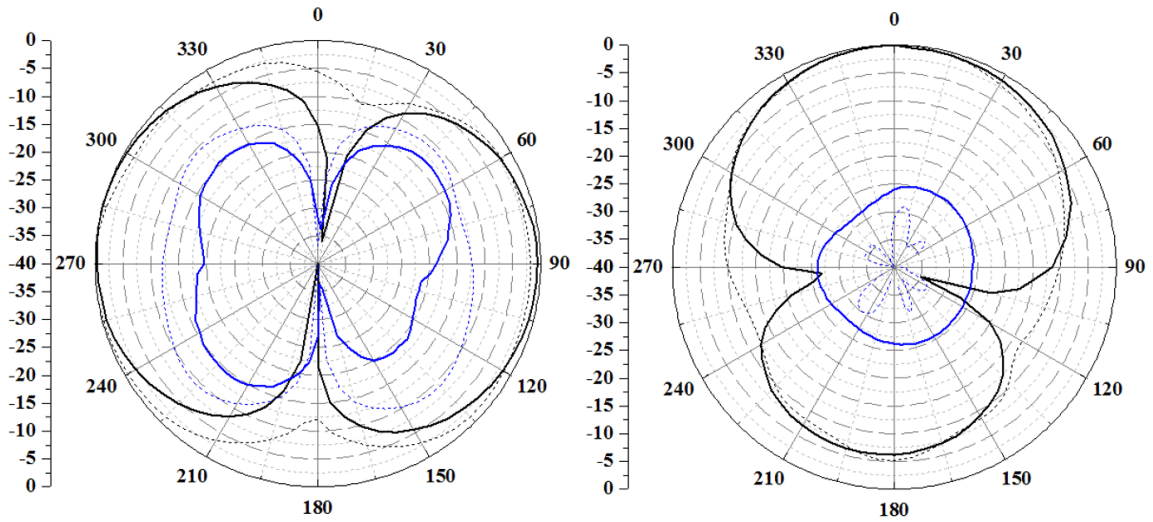


(e) (f)

Figure 4.13. Radiation patterns of the tri-polarized antenna (a) E-plane (+45 deg cut) at Port 1 (b) H-plane (-45 deg cut) at Port 1 (c) E-plane (-45 deg cut) at Port 2 (d) H-plane (+45 deg cut) at Port 2 (e) E-plane (XZ-plane) at Port 3 (f) H-plane (XY-plane) at Port 3

## 4.5 Conclusion

A flexible tri-polarized antenna with three feeding ports providing the three different polarizations has been demonstrated by using a cross-polarized antenna and ZOR array antenna. By using the ZOR array antenna for the vertical polarization, our proposed antenna can be ultra-low profile in the design. The proposed flexible tri-polarized antenna is very advantageous for example in wearable MIMO systems. Operating frequencies can also be easily scaled to desired spectrums. A good isolation performances (better than -20dB) have been obtained.

# Chapter 5

# Dual-Band/Tri-Polarized Metamaterial Antenna Based on Half-mode Hexagonal (HMH)) Substrate Integrated Waveguide (SIW) Using Flexible Substrate and Vias for WBAN communications

## 5.1 Introduction

Wireless body area networks (WBAN), which is a network of wearable computing devices, can be used for a range of applications such as health monitoring, emergency rescue service, physical training, and care for the elderly and children which can contribute to a better quality of life and improve people's health by providing useful information. In order to collect and analyze a large amount of information on health conditions, WBAN is designed to connect the network sensors to the human body, many of which can be read by one reader at the same time. The sensors can be implanted inside the body or surface-mounted on the body of a person to measure physiological changes, and WBAN connects independent nodes or sensors.

These system requires comfort, flexible materials in order to use in the human body. Since there is the limited space on a human body, the diversity such as space diversity, pattern diversity, and polarization diversity play an important role in WBANs. For off-

body communication, wearable systems usually require a low-profile dual-polarized antenna to improve the communication quality. It is used to communicate from on-body device to off-body devices or embedded devices. By adding the vertical polarization, the antenna can be employed for the on-body communication. The vertical polarized antenna over the body surface communicate efficiently with other co-located body worn devices. Antenna radiation pattern and polarization influence the on/off-body radio channels performance. Antenna with omnidirectional radiation pattern over the body surface improves the path for the on-body links while antenna with broadside polarization for off-body radiation pattern improves the path gain for off-body channels.

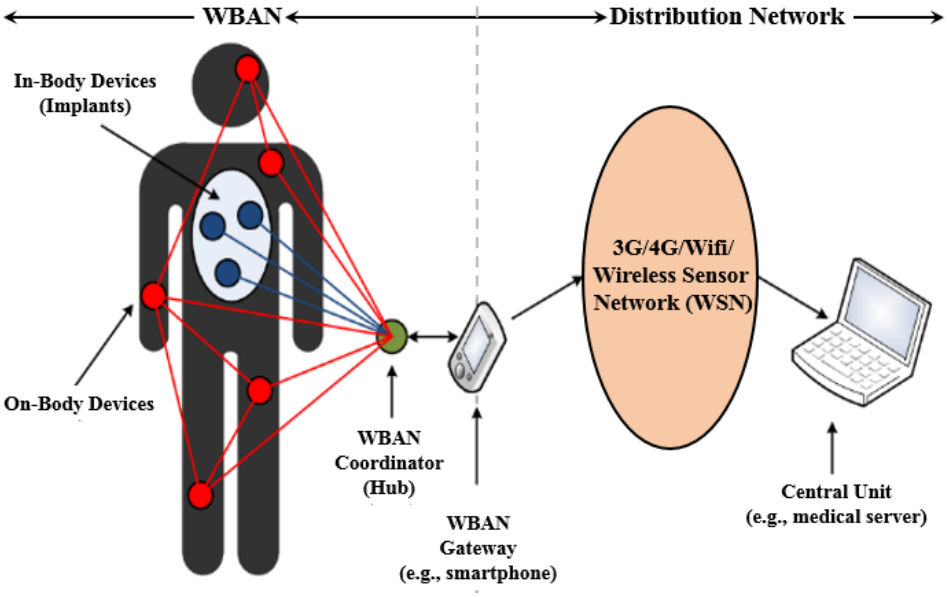


Figure 5.1. On-body communication and off-body communication in wireless body area network (WBANs)

Waveguide components are widely used in various microwave communication system, satellites, and wireless baseband station due to the high power capacity and low loss. However, waveguides are difficult to integrate with other components and they are

bulky. Recently, substrate integrated waveguides (SIW) represent an emerging approach for the implementation of waveguide-like components. The advantage of SIW is that can provide low cost, size reduction, complete shielding, and easy integration of planar circuits [75, 76]. The conventional SIW structure is designed by properly arranging the metallic vias on the substrate. These vias act as electrical walls resulting in the realization of waveguide structure in many applications such as filters and antennas. In order to reduce the size and efficiently integrate with other SIW structures, the shape of SIW structure plays an important role in designing the devices.

In this chapter, a dual band and diverse radiation pattern antenna is proposed for efficient and reliable on-body and off-body communications. A half mode hexagonal (HMH) SIW structure with the different internal angle is proposed to provide more design freedom which can design in a single structure and operate independently. In order to validate our concept, dual-band tri-polarized antenna is realized based on HMHSIW structure. The four HMHSIW can be closely placed so that four HMHSIW having different operations can efficiently be integrated. Thus, the antenna with dual band and diverse radiation patterns is designed and fabricated. In a single area, three different antennas are placed and operate at dual frequencies $f_1 \approx 3.2$ GHz and $f_2 \approx 5.78$ GHz.

## 5.2 Half-Mode Hexagonal Substrate Integrated Waveguide

Figure 5.2 shows an SIW structure which exhibits propagation characteristics similar to those of rectangular wave guide. It is designed by properly arranging on the substrate, the metallic vias that act as the electrical walls resulting in the realization of waveguide structure. In order to design the SIW structure, the effective width, $w_{eff}$, of SIW is obtained by

$$w_{eff} = w - 1.08\frac{d^2}{s} + 0.1\frac{d^2}{w} \tag{5.1}$$

where $d$ is the diameter of the metallic via. $w$ and $s$ represent spacing between the via arrays and spacing between the vias, respectively. In addition, $d$ and $s$ are selected to reduce the radiation loss due to EM field leakage in the SIW as well as enhance the return loss. The $w_{eff}$ also is calculated by

$$w_{eff} = \frac{c}{2 f_c \sqrt{\varepsilon_r}} \tag{5.2}$$

where $c$ is the speed of light in free space and $f_c$ is the lowest cutoff frequency of the $TE_{10}$ mode. Therefore, the distance between two via arrays determines the propagation constant of the fundamental mode. Since generally the dielectric losses are predominant at higher frequencies, it is important to use a dielectric substrate with the low loss to design SIW structures at mm-wave frequencies.

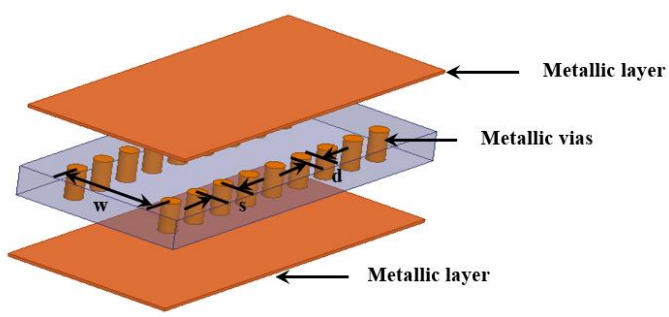


Figure 5.2. Configuration of a conventional SIW structure

SIW rectangular cavity is obtained by holding a part of a substrate using four sides of metallic vias which react as equivalent electrical walls ($E=0$). When the width ($w$) and length ($l$) of the SIW cavity are the same, the electric and magnetic fields for the dominant $TE_{110}$ mode can be expressed by

$$E_z = E_0 \sin\frac{\pi x}{a}\sin\frac{\pi y}{a} \tag{5.3}$$

$$H_x = \frac{j\pi E_0}{k\eta a}\sin\frac{\pi x}{a}\cos\frac{\pi y}{a} \tag{5.4}$$

$$H_y = \frac{-j\beta_z E_0}{k\eta}\cos\frac{\pi x}{a}\sin\frac{\pi y}{a} \tag{5.5}$$

$$E_x = E_y = H_z = 0 \tag{5.6}$$

where $\eta$ is the intrinsic impedance of a dielectric material inside the cavity and $k = \omega\sqrt{\mu\varepsilon}$ is the wavenumber. The phase constant is given by

$$\beta_z = \beta_{110} = \sqrt{k^2 - 2\left(\frac{\pi}{a}\right)^2} \tag{5.7}$$

where $w=l=a$. The lowest mode of the SIW cavity is $TE_{110}$ mode, and the resonant frequency of $TE_{110}$ mode is given by

$$f_{110} = \frac{1}{2\pi\sqrt{\mu\varepsilon}}\sqrt{\left(\frac{\pi}{w}\right)^2 + \left(\frac{\pi}{l}\right)^2} \tag{5.8}$$

The magnitude of the E-field distribution of a conventional SIW cavity is plotted in Figure 5.3(a). The electric field for the dominant mode of the SIW is perpendicular to the sidewalls, while the direction of the magnetic field is parallel to the waveguide surface. When the SIW cavity is cut on A-A' along the perfect magnetic wall, the Half mode SIW (HMSIW) cavity which keeps half of the field distribution of the dominant mode $TE_{110}$ is obtained as shown in Figure 5.3(b). Thus, the HMSIW can reduce the size of the SIW by half.

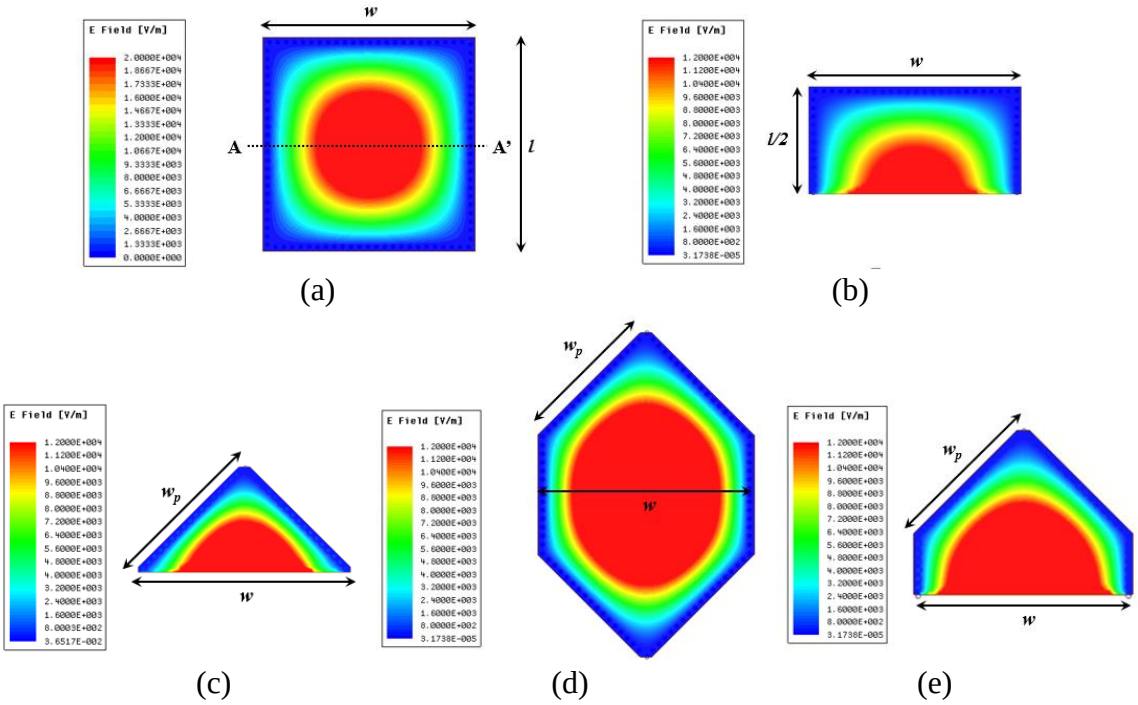


Figure 5.3. Simulated magnitude of the total E-field distributions of (a) full-mode SIW, (b) HMSIW, (c) triangular SIW, (d) hexagonal SIW (e) half-mode hexagonal SIW at their dominant resonant frequencies (*w=l=38mm*).

The triangular mode SIW (TMSIW) is obtained from SIW cavity by diagonally bisecting it into two sections, so that its geometry is an isosceles triangle with one open side (perfect magnetic conductor) and three via arrays (perfect electric conductor). The difference between the two electric fields distributions in SIW and TMSIW is shown in Figure 5.3(c). The resonant frequency of TMSIW is determined by the length of leg of a right triangles as you can see in Table I. Hexagonal SIW can combine flexibility of rectangular cavity and performance of circular cavity. The configurations and the electric field distributions of fundamental mode of a hexagonal SIW cavity are shown in Figure 5.3(d).

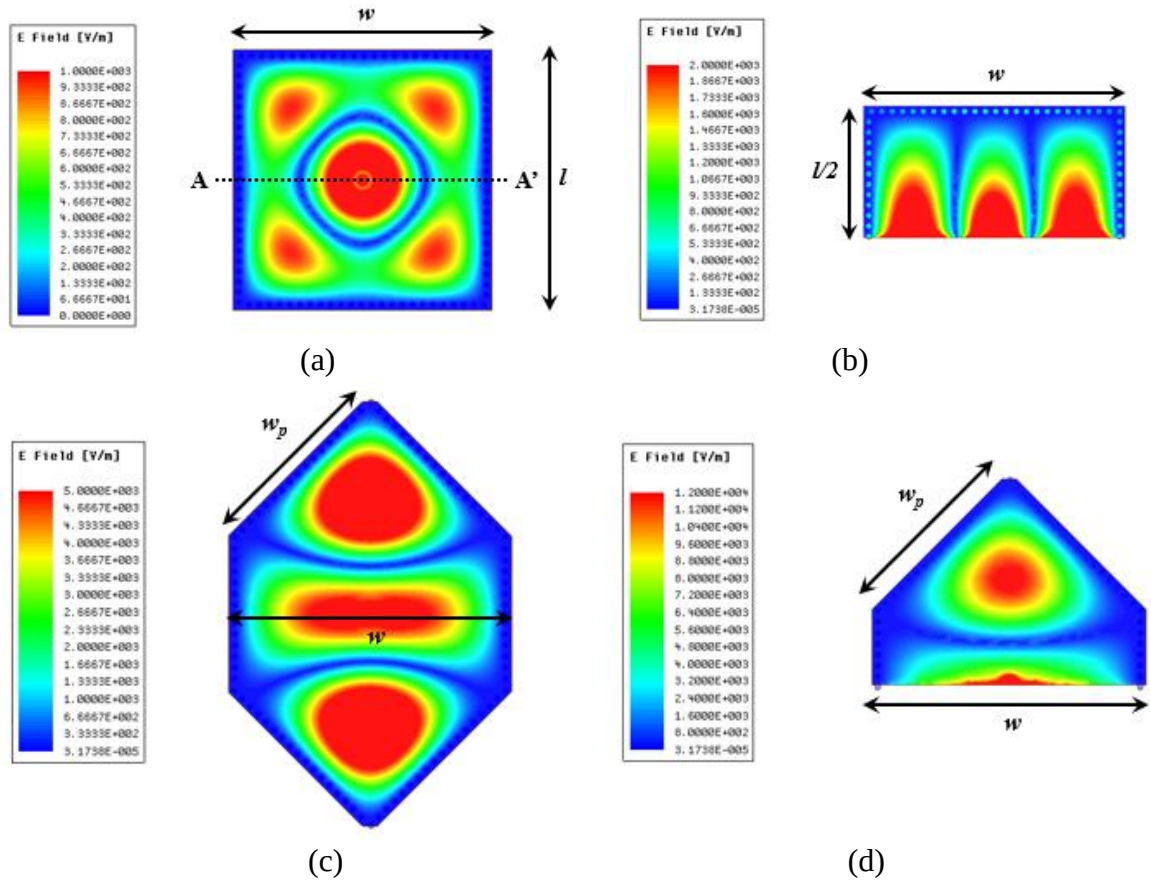


Figure 5.4. Simulated magnitude of the total E-field distributions of (a) full-mode SIW, (b) HMSIW, (c) triangular SIW, (d) hexagonal SIW at their higher-order resonant frequencies (*w=l=38mm*).

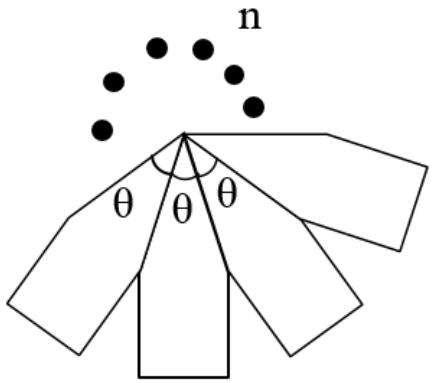


Figure 5.5. The configuration of the use of half-mode hexagonal SIW with the arbitrary internal angle

As shown in Figure 5.5, the half mode hexagonal SIW (HMHSIW) can have the different internal angles between equilateral triangle to , and the angle (θ) is determined by

$$\theta = \frac{2\pi}{n} \tag{1}$$

where $n$ is the number of half mode hexagonal SIW. By selecting the inner angle, the number of elements are determined and they are integrated in the center. The half-mode hexagonal (HMH) SIW is obtained from SIW rectangular cavity by diagonally bisecting the square cavity into two sections and adding two via walls in open side. Thus, its geometry is a pentagon with one open side (perfect magnetic conductor) and four via arrays (perfect electric conductor) as shown in Figure 5.3(e). The resonant frequency of HMHSIW is determined by the length of the open side. The resonant frequencies and area of the SIW, HMSIW, and TMSIW are investigated and tabulated in Table 5.1.

TABLE 5.1 COMPARISON BETWEEN FULL-MODE SIW, HMSIW, TMSIW, AND HMHSIW

| | 1st Resonant Frequency | 2nd Resonant Frequency | Size ($mm^2$) |
|---|---|---|---|
| Full-mode SIW | 3.17 GHz | 7.185 GHz | 1,444 |
| Half-mode SIW | 3.12 GHz | 6.78 GHz | 722 |
| Triangular SIW | 4.08 GHz | 8.3 GHz | 361 |
| Half-mode hexagonal SIW | 3.01 GHz | 5.847 GHz | 1,083 |

## 5.3 The Configuration of the Dual-band/Tri-polarization SIW Antenna Based on Half-mode Hexagonal SIW

For wireless communication, a dual frequency antenna is needed for simultaneously

transmitting and receiving these two bands [77, 78]. In order to verify our proposed HMHSIW, dual-band tri-polarized antenna is realized with the composite right/left-handed transmission lines (CRLH TLs) and half mode hexagonal SIW. The CRLH TLs behave as metamaterial, producing simultaneous negative permittivity ($\varepsilon_r$) and permeability ($\mu_r$) properties [55]. A unit-cell of a CRLH-TL consists of a conventional right-handed (RH) TL and a left-handed (LH) TL as shown in Figure 5.6(a). RH TL has shunt inductor ($L_R$) and series capacitors ($C_R$), and LH TL has series capacitors ($C_L$) and shunt inductor ($L_L$). $R$ is the resistance accounting both radiative and material losses, and $G$ is the conductance due to dielectric loss of the substrates.

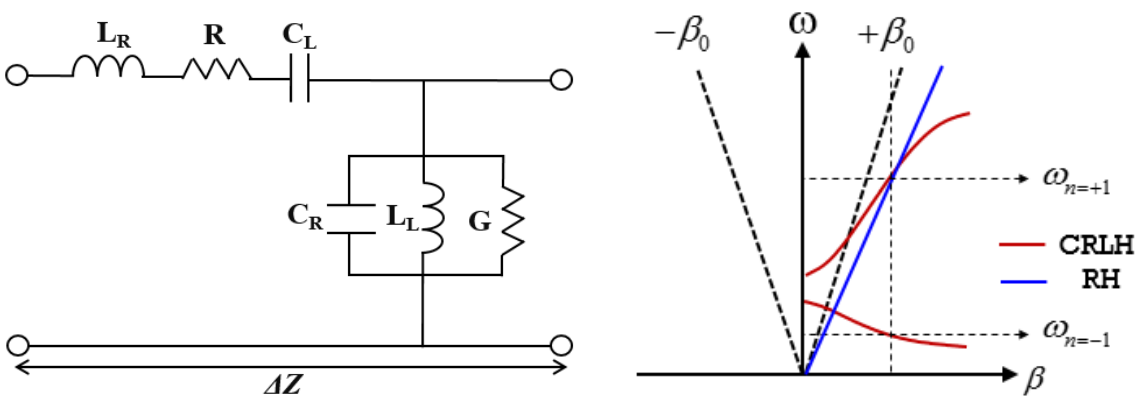


(a) (b)

Figure 5. 6. (a) Equivalent circuit model of a CRLH SIW unit cell. (b) General Dispersion comparison between conventional half wavelength antenna and metamaterial antenna.

According to the theory of open-ended or short-ended resonators with a CRLH TL, the resonant frequencies of different order modes for an N-stage CRLH TL can be found on the dispersion curve when the electrical length, $\theta=\beta l$ satisfies. The phase constant ($\beta$) is determined by

$$\beta(\omega) = \frac{s(\omega)}{\Delta l}\sqrt{\omega^2 L_R C_R + \frac{1}{\omega^2 L_L C_L} - \frac{L_R C_L + L_L C_R}{L_L C_L}} \tag{5.1}$$

where $s(\omega)$ and $\Delta l$ are the sign function and the differential length, respectively. In order to realize $C_L$ and $L_L$ in HMHSIW, the interdigital capacitor slots etched on the top of the metallic surface serve as a series capacitance ($C_L$), and the 0.8-mm diameter metallic vias connecting between the top layer and ground plane behave as shunt inductance ($L_L$).

The proposed dual-band tri-polarization antenna consists of two parts of cross-polarized CRLH SIW antenna and ZOR antennas as shown in Figure 5.7(a). Since each HMHSIW has 90deg internal angle, four HMSIW can be efficiently integrated in the center. First of all, the design process for cross-polarized CRLH resonant antennas is similar to that of the conventional resonant antennas requiring proper coupling and terminations (either open or short). In general, the conventional resonant antennas have the resonant modes when length $d$ is equal to $(n \cdot \lambda g)/2$ with the resonant mode index ($n$) = positive integer. However, $n$ for CRLH resonant antennas can be both positive and negative integer, even zero. The comparison between the dispersion relations of the conventional antenna and the CRLH antenna can be seen from the simplified dispersion diagram as shown in Figure 5.6(b). The $n$ = +1 resonant mode is similar to that of conventional $\lambda g$ /2 resonant antenna such as patch antenna ($\lambda g$ is the guided wavelength). However, CRLH structure has $n$ = -1 mode which also resonates with half wavelength field distribution but at much lower frequency. The operating frequency at $n$ = -1 mode is lowered without the change of the structural dimension, so that the antenna behaves as electrically-small radiator. The cross-polarized CRLH resonant antenna is realized on the HMSSIW as shown in Figure 5.7(b). Since both -1 and +1 modes exhibit half-wavelength field distribution with the field

null at the center of the SIW antenna, a second port can be connected at this location to generate dual-polarization with high port-to-port isolation at both frequencies. Thus, dual polarization is realized by placing the two feed lines along the orthogonal directions with respect to each other. In addition, $n = 0$ mode can be suppressed by placing via wall at the center of the antenna. The direction of interdigital slots determines the polarization of CRLH resonant SIW antenna.

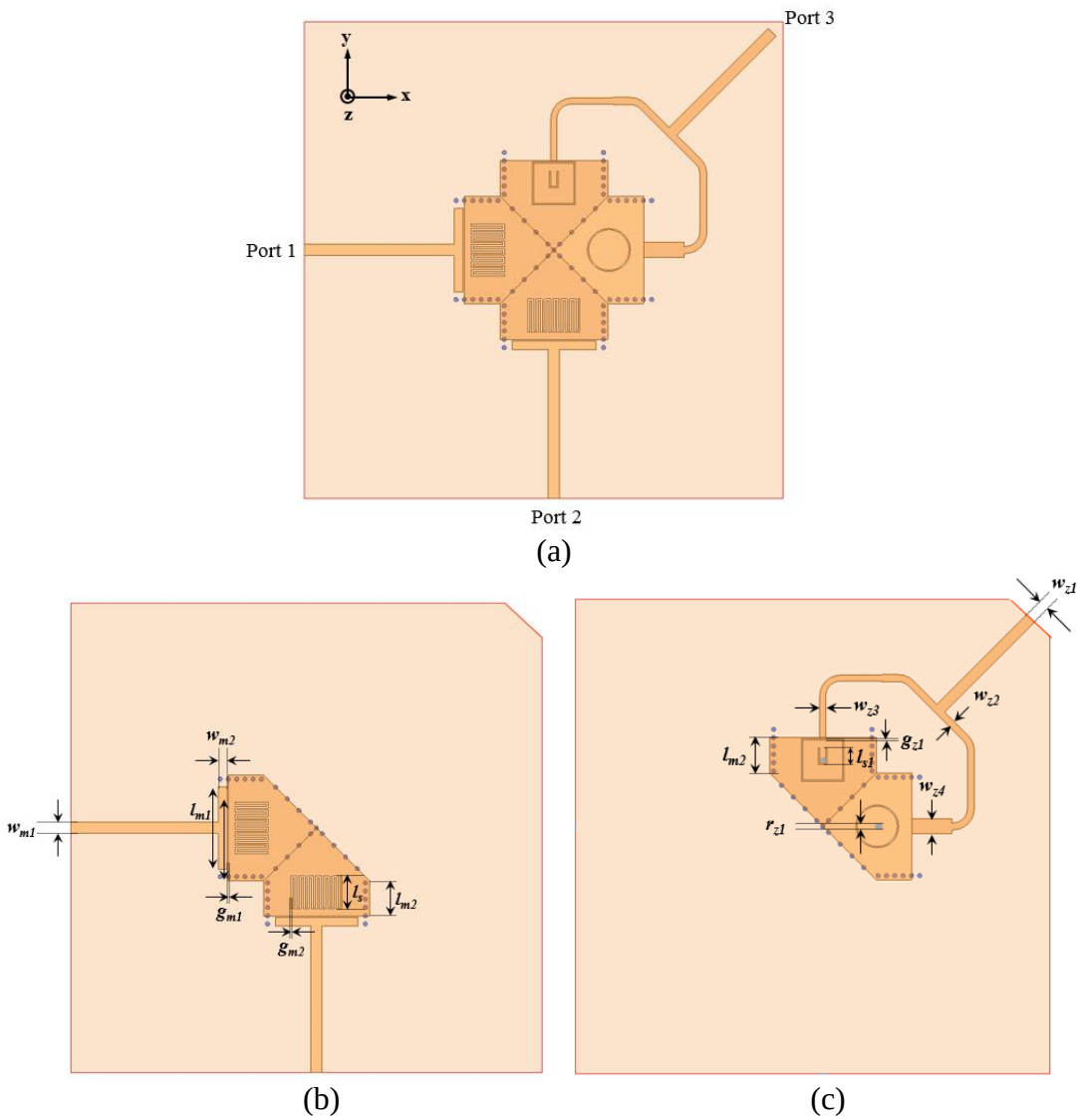


Figure 5.7. (a) Perspective view of the dual-band tri-polarized antenna (a) Dual-band cross-polarized CRLH HMHSIW antenna (b) Dual-band ZOR HMHSIW antenna. (Dimension

[mm] of the antenna are: $w_{m1} = w_{z1}$ =1.87, $w_{z2}$ =1.19, $w_{z3}$ =0.3, $w_{z4}$ =1.5, $w_{m2}$ = 1.5, $l_{m2}$ = 6, $l_s$ = 6, $l_{s1}$ = 3.5, $g_{m1} = g_{m2} = g_{z1}$ = 0.2, $r_{z1}$ = 0.7)

Dispersion characteristics of the CRLH structure can be manipulated to adjust the spectral separation between the two operating frequencies. Two cross-polarized CRLH SIW unit cells with its dual counterpart rotated 90° from each other are cascaded together, and this arrangement are fed by a 50 Ω transmission line as shown in Figure 5.7. A gap feeding line is used to match a 50 Ω transmission line at the -1st and +1st modes in HMHSIW antennas, and via walls of the SIW cavity are used to provide high isolation between the two orthogonal port and low cross polarization radiation. The high isolation and low cross polarization are two very important factors for any dual-polarized antenna.

Secondly, dual-band ZOR antenna based on HMHSIW configuration is also designed to integrate with cross-polarized CRLH HMHSIW antenna. Via wall shorts the end of the SIW to obtain a SIW cavity resonator so that it can be modeled as a short-ended CRLH resonator. Thus, zeroth-order resonance (ZOR) frequency is determined by

$$\omega_{se} = \frac{1}{\sqrt{L_R C_L}} \tag{5.1}$$

This frequency is called the zeroth-order resonance (ZOR) frequency. In order to make the vertical polarization, the slots are added on the HMHSIW structure and a via is centered.

## 5.4 Simulation and Measurement Results

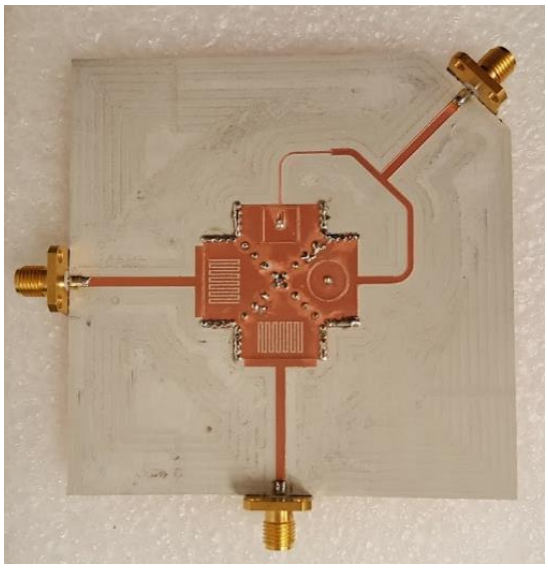

Figure 5.8. The fabricated dual-band tri-polarized antenna based on half-mode hexagonal SIW structure

The dual-band tri-polarized HMHSIW antenna in Figure 5.8 is fabricated using 0.762 mm thickness RT/duroid RO3003 substrate. As shown in Figure 5.9 and 5.10, simulated and measured S-parameter results show the feasibility of designing planar single radiator that can provide both dual-frequency and tri-polarized operation by placing HMHSIW antennas closely. Our dual-band antenna operates at frequencies $f_1 \approx 3.2$ GHz and $f_2 \approx 5.78$ GHz. The n = -1st mode resonance frequency is located around 3.2 GHz while n = +1st mode resonated around 5.78 GHz. The dual -band ZOR antenna is also designed to operate at both 3.2 GHz and 5.78 GHz. The size of fabricated antenna is $0.17\ \lambda_1 \times 0.28\ \lambda_1$ at $f_1$ and $0.34\ \lambda_2 \times 0.48\ \lambda_2$ at $f_2$ where $\lambda_1$ and $\lambda_2$ are the free space wavelengths. Return loss higher than 10dB is achieved at both frequencies, and port-to-port isolations higher than 15dB are observed for both operating frequencies as shown in Figure 5.9 and 5.10. In order to validate our concept, a prototype of the antenna is fabricated using a high resolution LPKF milling machine (ProtoMat S103) which ensures the accuracy of the drillings and ultra-

fine milling of the design. The antenna design pattern is printed on Roger RO3003 laminated with 1 oz. copper which have relative permittivity value of $\varepsilon_r$ =3.0 and loss tangent of $tan\ \delta$ = 0.001. Although small discrepancy is observed and can be due to fabrication errors, both S-parameter results are in good agreement.

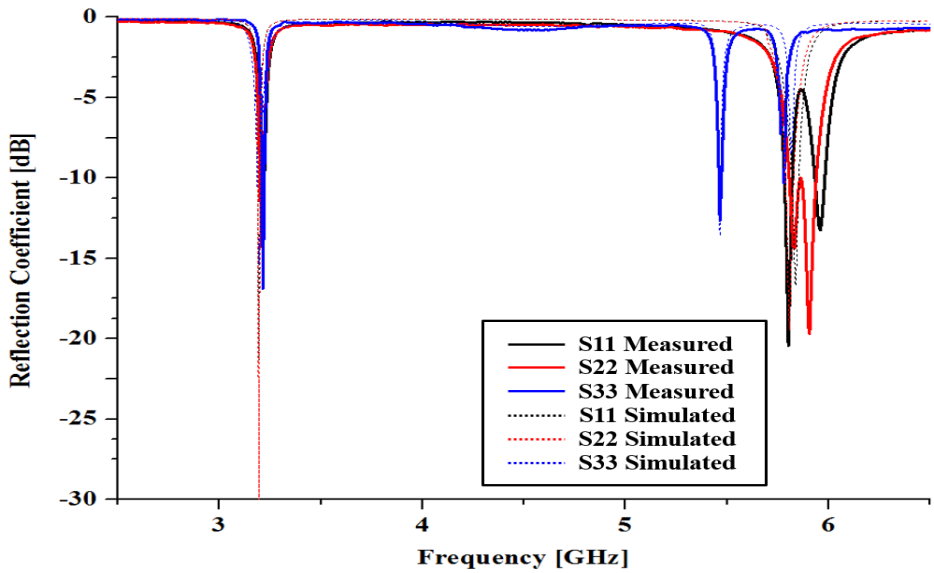


Figure 5.9. Measured and simulated return loss of each port of the of the tri-polarized SIW metamaterial antenna.

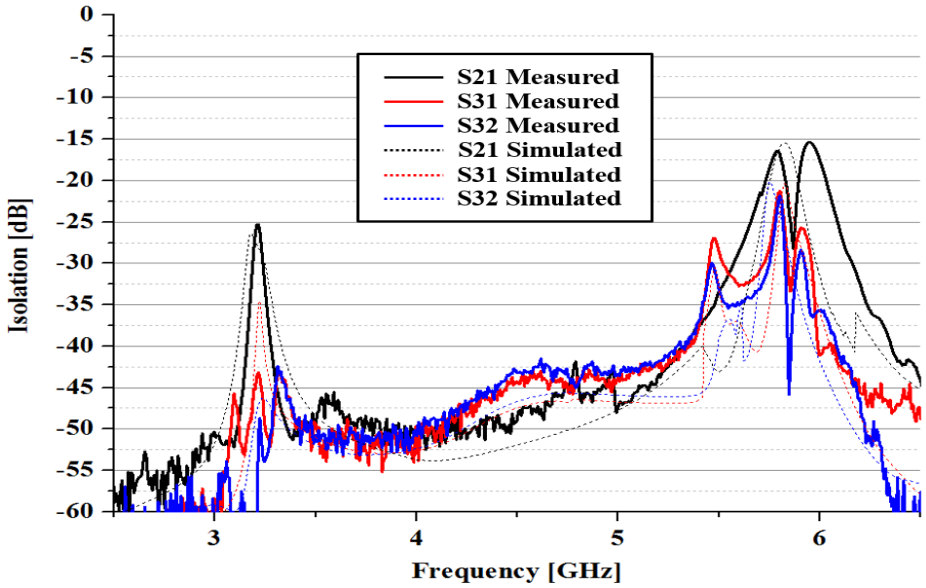


Figure 5.10. Measured and simulated isolation between each two ports of the of the tri-

polarized SIW metamaterial antenna.

The simulated normalized-radiation patterns are also illustrated in Figure 5.11. A broadside radiation patterns at port 1 and 2 are achieved at both frequencies due to their half wavelength field distribution characteristics, and vertical electric field is obtained from dual-band ZOR design at both frequencies.

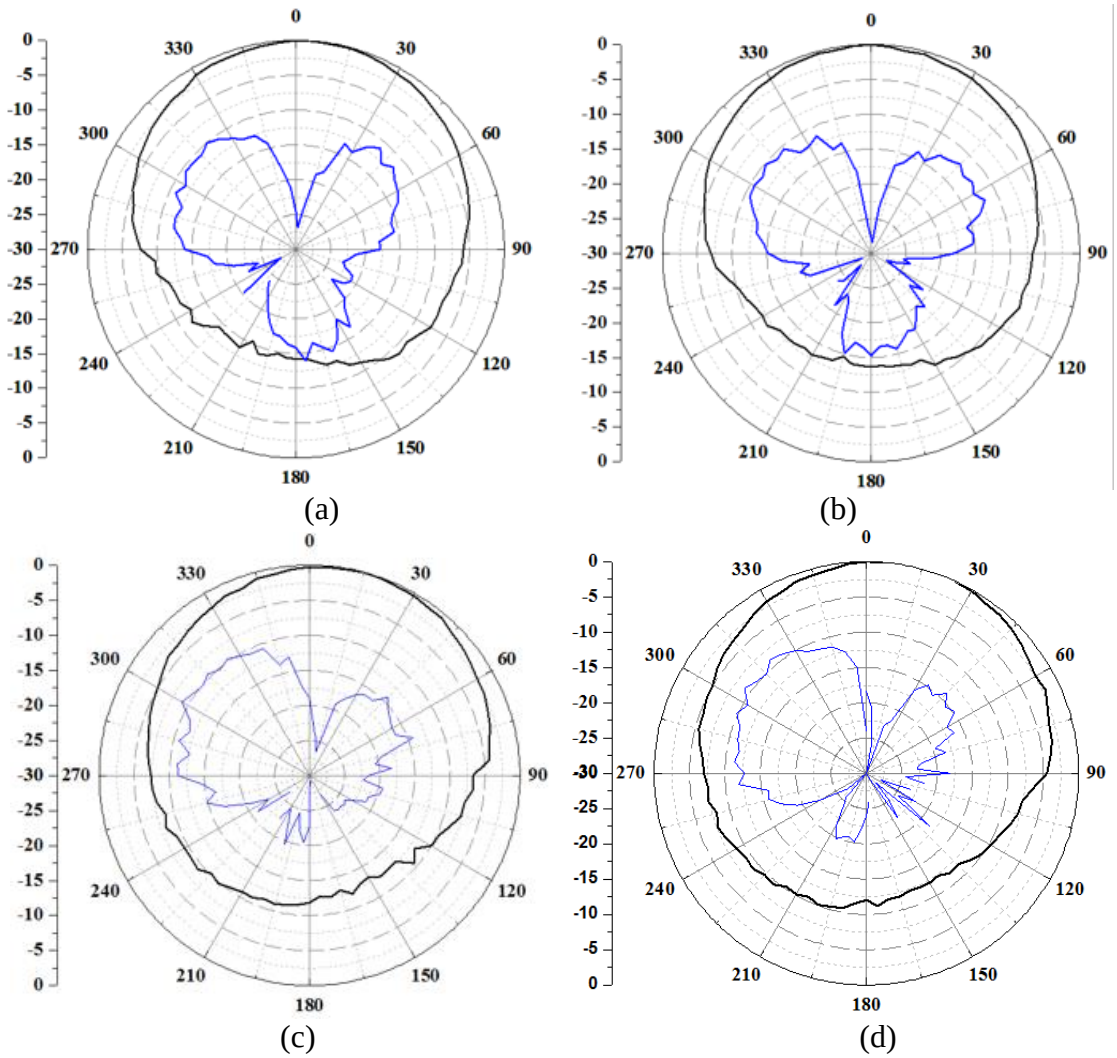

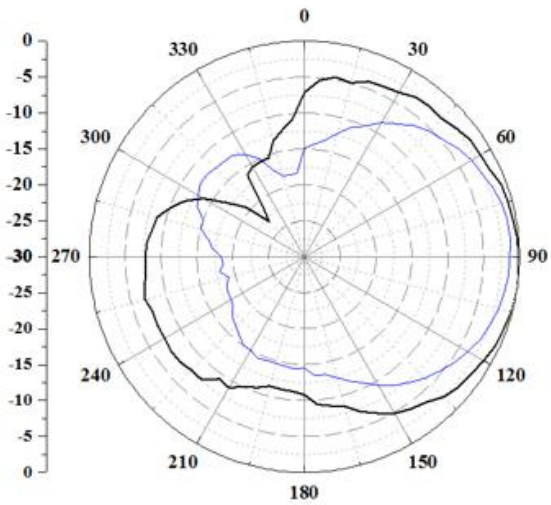


(e)

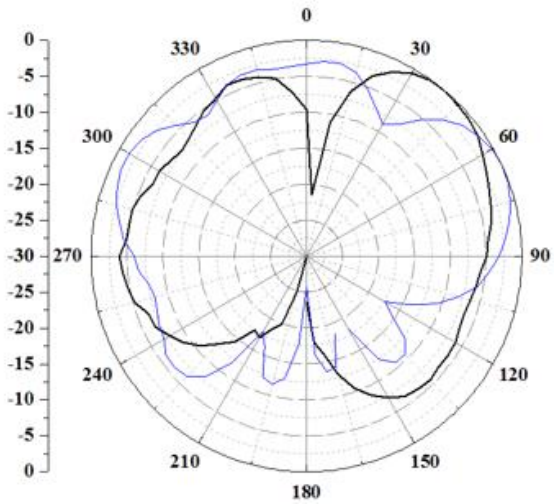


(f)

Figure 5.11. Measured and simulated radiation patterns of the proposed HMHSIW at both frequencies (a) & (c) E-planes at n=-1st mode (b) & (d) E-planes at n=+1st mode (e) 0th mode at lower frequency (f) 0th mode at higher frequency

## 5.5 Conclusion

A planar, low-profile, and flexible tripolarized antenna is proposed with three feeding ports for polarization diversity applications. By placing HMHSIW structure in the center, CRLH SIW antenna and ZOR SIW antenna are used with three feeding ports providing the three different polarizations in a single electrically-small element. By using -1, 0, and +1 modes, good isolation performances have been obtained. The half-mode hexagonal SIW can be designed with the different angles, so that the several structures can be integrated in a single element. Each HMHSIW can have different structures such as filters and antennas. The dual-band operating frequencies of the proposed antenna can also be easily scaled to desired spectrums. This novel antenna can provide much improved wireless communication efficiency for the WBAN system under various incident field angles and polarizations.

# Chapter 6

# Conclusions and Future Work

## 6.1 Summary of Achievements

In this dissertation, we have proposed and experimentally demonstrated an optically transparent, flexible, and polarization-independent broadband microwave absorber. It is designed to possess two spectrally overlapped resonances of a bow-tie array, which originates from the fundamental resonance mode and the coupling between the neighboring units. Al Wire gird is used to construct the bow-tie array to induce high ohmic loss and broaden the bandwidth of the resonances. As a result, the combined resonances lead to more than 90% total absorption cover a wide frequency range from 5.8 to 12.2GHz. The transparent and flexible properties provide more flexibility for absorber applications. The optical transmittance of the whole structure is more than 62%.

In Chapter 3, we have presented the optically semi-transparent, flexible and mechanically reconfigurable zeroth-order resonant (ZOR) antenna using stretchable micromesh structure. The size reduction of the antenna is achieved by using the ZOR property, and the uniform metallic patches of the antenna are replaced with the tortuous micromesh. The tortuous micromesh structures provide a high degree of freedom for stretching when encapsulated in elastomeric polymers, as well as optical transparency.

Accordingly, the structure can undergo mechanical deformation such as stretching (up to 40%), folding, or twisting without breakage. The resonant frequency of the antennas is linearly reconfigurable from 2.94 GHz to 2.46 GHz upon stretching. Such tunable antenna could be potentially used for the transparent, flexible, and stretchable radiofrequency wearable applications.

In Chapter 4, a flexible and low-profile triple-polarization antenna fabricated with flexible substrate and silver nanowire (AgNW) vias was presented. Highly conductive AgNWs that are ~200um long enables to realize the flexible metallic vias. Since the metamaterial-inspired array antenna is used to obtain the vertical polarization, the proposed flexible tri-polarized antenna could be realized with ultra-low profile characteristic compared with other tri-polarized antennas. Thus, it can be employed for WBAN or MIMO applications.

In Chapter 5, a dual-band and diverse radiation pattern antenna was proposed for efficient and reliable on-body and off-body communications. A half mode hexagonal (HMH) SIW structure with the different internal angle was proposed to design and integrate the several independent structures in a single structure. In order to validate our concept, dual-band tri-polarized antenna was realized by using four HMHSIW structures. The four HMHSIWs which use the -1th mode, 0th mode, and +1th mode were closely placed so that the dual-band antenna with diverse radiation patterns was designed and fabricated. In a single area, three different antennas are placed and operate at dual frequencies $f_1 \approx 3.2$ GHz and $f_2 \approx 5.78$ GHz.

## 6.2 Future works

While the main contribution of this thesis is on the design of RF devices using the novel materials and fabrication techniques, the direction of the future works will entail an increase of the transparency and improved their performance with low loss at mm-meter wave range.

We have demonstrated a new method for fabricating transparent and stretchable radiofrequency small antennas by using stretchable micromesh structure in Chapter 3. Micromesh have designed and fabricated to be optically transparent and mechanically stretchable. The increase in the tensile strain results in the change of the resonant frequency of the antenna. However, the optical transparency is not enough to apply to the transparent applications. The optical transparency and electrical conductivity change in opposite directions. Human eye cannot see the line which the width is less than 1μm. Thus, instead of dense micromesh, the highly optically transparent antenna can be achieved by using thinner micromesh or large opening.

As discussed in Chapter 4, a low-profile flexible triple-polarized antenna can be used for WBAN network or wearable applications. It can also be realized on the Cyclic Olefin Copolymer (COC) material and silver nanowires (AgNWs) ink to be optically transparent and structurally flexible because COC has high optical transparency and very low loss. Cyclic olefin copolymer (COC) possesses high optical transparency, excellent electrical properties, and high rigidity. The COC substrates with a relative permittivity of $\varepsilon_r$=2.35 and a loss tangent of tan $\delta$= 0.00007 at 100MHz is obtained from Dow Corning. COC has properties similar to PDMS, but has a higher endurance. Since COC has low loss, it is well-suited for applications to microwave range devices. COC has glass-like transparency, low

density, high heat-deflection temperature, and excellent electrical properties, as shown in Table 6.1.

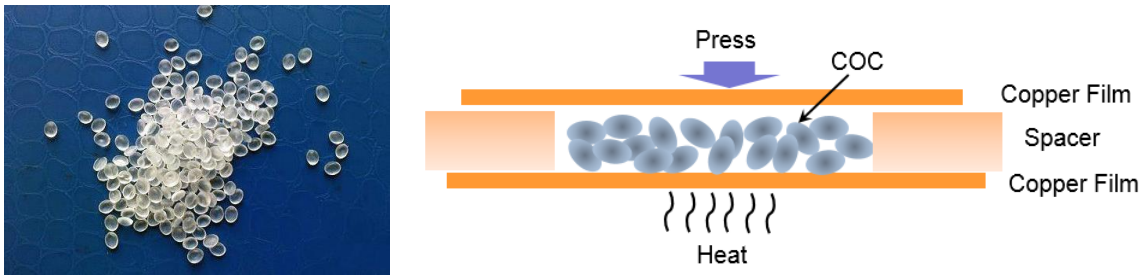


(a) (b)

Figure 6.1. (a) Pure Cyclic Olefin Copolymer (COC) grains (b) Heat-Pressure Imprinting Process

Table 6.1. Properties of cyclic olefin copolymer

| | Value |
|---|---|
| Dielectric constant | 2.35 |
| Dielectric loss tangent | 0.00007 |
| Dielectric loss tangent (@0.1-10THz) [78] | 0.00094 |
| Dielectric loss tangent (@2.5THz) [77] | 0.0023 |
| Density (g/cc) | 1.02 |
| Optical transmission (%) | 92 |
| Dielectric breakdown | 30kV/mm |

Another future work can be COC-based SIW antenna as shown in Figure 6.1. At high frequency, the dielectric loss of the substrate is increased. However, the COC substrate has very low loss tangent at 0.1-100THz. Although the SIW based on COC and silver nanowire

ink is flexible, it is not optically transparent. Thus, the SIW antenna based on COC substrate can be designed by using embedded metal mesh transparent electrode (EMTEs) in order to be optically transparent as well as to be flexible.

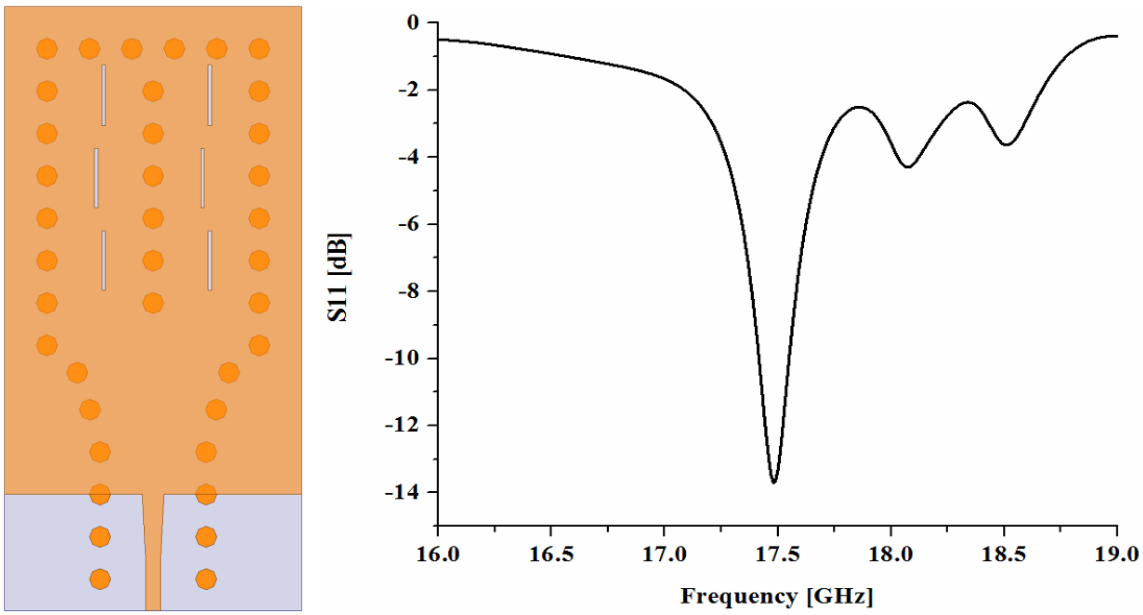


(a) (b)

Figure 6.2. (a) COC-based SIW slot antenna (b) S-parameter

# Bibliography


[1] H. Kanaya, S. Tsukamaoto, T. Hirabaru, D. Kanemoto, R. K. Pokharel, and K. Yoshida, "Energy Harvesting Circuit on a One-Sided Directional Flexible Antenna," vol. 23, pp. 164-166, 2013.

[2] C. Lin, C. Chang, Y. T. Cheng, and C. F. Jou "Development of a Flexible SU-8/PDMS-Based Antenna," vol. 10, pp. 1108-1111, 2011.

[3] M. L. Scarpello, D. Kurup, H. Rogier, D. V. Ginste, F. Axisa, J. Vanfleteren, W. Joseph, L. Martens, G. Vermeeren, "Design of an Implantable Slot Dipole Conformal Flexible Antenna for Biomedical Applications," vol. 59, pp. 3556-3564, 2011.

[4] A. C. Siegel, S. T. Phillips, M. D. Dickey, N. Lu, Z. Suo, and G. M. Whitesides, "Foldable Printed Circuit Boards on Paper Substrates," vol. 20, pp. 28-35, 2010.

[5] M. Hirvonen, C. Bohme, D. Severac, and M. Maman, "On-Body Propagation Performance With Textile Antennas at 867 MHz," vol. 61, pp. 2195-2199, 2013.

[6] S. Park, G. Wang, B. Cho, Y. Kim, S. Song, Y. Ji, *et al.*, "Flexible molecular-scale electronic devices," vol. 7, pp. 438-442, 2012.

[7] E. M. Cruz, F. Colombel, M. Himdi, G. Legeay, X. Castel, and S. Vigneron, "Ultrathin metal layer, ITO film and ITO/Cu/ITO multilayer towards transparent antenna," vol. 3, pp. 229-234, 2009.

[8] J. Hautcoeur, F. Colombel, X. Castel, M. Himdi, and E. M. Cruz, "Optically transparent monopole antenna with high radiation efficiency manufactured with silver grid layer (AgGL)," vol. 45, p. 1014, 2009.

[9] D. J. Lipomi, M. Vosgueritchian, B. C. Tee, S. L. Hellstrom, J. A. Lee, C. H. Fox, *et al.*, "Skin-like pressure and strain sensors based on transparent elastic films of carbon nanotubes," vol. 6, pp. 788-792, 2011.

[10] H. J. Song, T. Y. Hsu, D. F. Sievenpiper, H. P. Hsu, J. Schaffner, and E. Yasan, "A Method for Improving the Efficiency of Transparent Film Antennas," vol. 7, pp. 753-756, 2008.

[11] D. Park, A. A. Schendel, S. Mikael, S. K. Brodnick, T. J. Richner, J. P. Ness, *et al.*, "Graphene-based carbon-layered electrode array technology for neural imaging and optogenetic applications," vol. 5, p. 5258, 2014.

[12] H. Atwater and A. Polman, "Plasmonics for improved photovoltaic devices," vol. 9, pp. 205-213, March 2010.

[13] K. Aydin, V. Ferry, R. Briggs, and H. Atwater, "Broadband polarization-independent resonant light absorption using ultrathin plasmonic super absorbers," vol. 2, p. 517, December 2011.

[14] H. Zhu, F. Yi, and E. Cubukcu, "Nanoantenna Absorbers for Thermal Detectors," vol. 24, pp. 1194-1196, August 2012.

[15] W. H. Emerson, "Electromagnetic Wave Absorbers and Anechoic Chambers through the Years," *IEEE Trans. Antennas Propagation*, pp. 484-490, 1973.
[16] S. Bhattacharyya, S. Ghosh, and K. Srivastava, "Triple band polarization-independent metamaterial absorber with bandwidth enhancement at X-band," vol. 114, p. 094514, February 2013.
[17] F. Dincer, M. Karaaslan, E. Unal, and C. Sabah, "Dual-band polarization-independent metamaterial absorber based on omega resonator and octa-star strip configuration," vol. 141, pp. 219-231, February 2013.
[18] N. Landy, S. Sajuyigbe, J. Mock, Smith, and W. Ailla, "Perfect metamaterial absorber," pp. 1-4, February 2008.
[19] Smith, D. Vier, T. Koschny, and C. Soukoulis, "Electromagnetic parameter retrieval from inhomogeneous metamaterials," pp. 1-11, February 2005.
[20] H. Tao, N. Landy, C. Bingham, and X. Zhang, "A metamaterial absorber for the terahertz regime: Design, fabrication and characterization," pp. 1-8, February 2008.
[21] J. Grant, Y. Ma, S. Saha, A. Khalid, and D. Cumming, "Polarization insensitive, broadband terahertz metamaterial absorber," February 2011.
[22] Y. Ye, Y. Jin, and S. He, "Omnidirectional, polarization-insensitive and broadband thin absorber in the terahertz regime," February 2010.
[23] W. W. Salisbury, *U.S. Patent 2599944*, 1952.
[24] G. T. Ruck, D. E. Barrick, and W. D. Stuart, *Radar Cross Section Handbook, New York*, vol. 2, 1970.
[25] E. Knott, J. F. Shaeffer, and M. T. Tuley, *Radar Cross Section, 2nd edition, Raleigh*, 2004.
[26] Y. Okano, S. Ogino, and K. Ishikawa, "Development of Optically Transparent Ultrathin Microwave Absorber for Ultrahigh-Frequency RF Identification System," vol. 60, pp. 2456-2464, September 2012.
[27] P. Singh, K. Korolev, M. Afsar, and S. Sonkusale, "Single and dual band 77/95/110 GHz metamaterial absorbers on flexible polyimide substrate," vol. 99, p. 264101, February 2011.
[28] F. Pardo, P. Bouchon, R. Haïdar, and J. Pelouard, "Light funneling mechanism explained by magnetoelectric interference," pp. 1-4, February 2011.
[29] M. Kwak, J. Ok, J. Lee, and L. Guo, "Continuous phase-shift lithography with a roll-type mask and application to transparent conductor fabrication," vol. 23, p. 344008, September 2012.
[30] J. Ok, M. Kwak, C. Huard, H. Youn, and L. Guo, "Photo-Roll Lithography (PRL) for Continuous and Scalable Patterning with Application in Flexible Electronics," vol. 25, pp. 6554-6561, 2013.
[31] T. J. Jung, J. H. Kwon, and S. Lim, "Flexible zeroth-order resonant antenna independent of substrate deformation," *Electronics Letters*, vol. 46, p. 740, May 2010.
[32] C.-P. Lin, C.-H. Chang, Y. T. Cheng, and C. F. Jou, "Development of a Flexible SU-8/PDMS-Based Antenna," *IEEE Antennas and Wireless Propagation Letters*, vol. 10, pp. 1108-1111, Oct. 2011.
[33] B. Aïssa, M. Nedil, M. A. Habib, E. Haddad, W. Jamroz, D. Therriault, *et al.*, "Fluidic patch antenna based on liquid metal alloy/single-wall carbon-nanotubes

operating at the S-band frequency," *Applied Physics Letters,* vol. 103, p. 063101, Aug. 2013.

[34] S. Cheng, A. Rydberg, K. Hjort, and Z. Wu, "Liquid metal stretchable unbalanced loop antenna," *Applied Physics Letters,* vol. 94, p. 144103, Apr. 2009.

[35] S. Cheng and Z. Wu, "A Microfluidic, Reversibly Stretchable, Large-Area Wireless Strain Sensor," *Advanced Functional Materials,* vol. 21, pp. 2282-2290, Mar. 2011.

[36] G. J. Hayes, J.-H. So, A. Qusba, M. D. Dickey, and G. Lazzi, "Flexible Liquid Metal Alloy (EGaIn) Microstrip Patch Antenna," *IEEE Transactions on Antennas and Propagation,* vol. 60, pp. 2151-2156, Jun. 2012.

[37] M. Kubo, X. Li, C. Kim, M. Hashimoto, B. J. Wiley, D. Ham, *et al.*, "Stretchable microfluidic radiofrequency antennas," *Advanced Materials,* vol. 22, pp. 2749-52, Jul. 2010.

[38] Z. Wang, L. Lee, D. Psychoudakis, and J. Volakis, "Embroidered Multiband Body-Worn Antenna for GSM/PCS/WLAN Communications," *IEEE Transactions on Antennas and Propagation,* vol. PP, pp. 1-1, Jun. 2014.

[39] T. F. Kennedy, P. W. Fink, A. W. Chu, N. J. Champagne, G. Y. Lin, and M. A. Khayat, "Body-Worn E-Textile Antennas: The Good, the Low-Mass, and the Conformal," *IEEE Transactions on Antennas and Propagation,* vol. 57, pp. 910-918, Apr. 2009.

[40] L. Huang and P. Russer, "Electrically Tunable Antenna Design Procedure for Mobile Applications," *IEEE Transactions on Microwave Theory and Techniques,* vol. 56, pp. 2789-2797, Dec. 2008.

[41] C. Jung, M. Lee, G. P. Li, and F. DeFlaviis, "Reconfigurable Scan-Beam Single-Arm Spiral Antenna Integrated With RF-MEMS Switches," *IEEE Transactions on Antennas and Propagation,* vol. 54, pp. 455-463, Mar. 2006.

[42] N. C. Karmakar, "Shorting strap tunable single feed dual-band stacked patch PIFA," *IEEE Antennas and Wireless Propagation Letters,* vol. 2, pp. 68-71, 2003.

[43] S. Hwang, Y. Bang, J. Kim, and T. Jang, "Switchable composite right/left-handed (S-CRLH) transmission line using MEMS switches," *Microwave and,* February 1 2009.

[44] T. Jang, S. Lim, and T. Itoh, "Tunable Compact Asymmetric Coplanar Waveguide Zeroth-Order Resonant Antenna," *Journal of Electromagnetic Waves and Applications,* vol. 25, pp. 2379-2388, Dec. 2011.

[45] S. C. D. Barrio and G. F. Pedersen, "Antenna Design Exploiting Duplex Isolation for 4G Application on Handsets," *Electronics Letters,* vol. 49, pp. 1197-1198, Sep. 2013.

[46] L. Song, A. C. Myers, J. J. Adams, and Y. Zhu, "Stretchable and Reversibly Deformable Radio Frequency Antennas Based on Silver Nanowires," *ACS Applied Materials & Interfaces,* vol. 6, pp. 4248-4253, Apr. 2014.

[47] J.-H. So, J. Thelen, A. Qusba, G. J. Hayes, G. Lazzi, and M. D. Dickey, "Reversibly Deformable and Mechanically Tunable Fluidic Antennas," *Advanced Functional Materials,* vol. 19, pp. 3632-3637, Nov. 2009.

[48] C. W. Trueman, A.-R. Sebak, T. A. Denidni, S. V. Hoa, A. Mehdipour, and I. D. Rosca, "Mechanically reconfigurable antennas using an anisotropic carbon-fibre composite ground," *IET Microwaves, Antennas & Propagation,* vol. 7, pp. 1055-1063, Oct. 2013.

[49] T. Jang, H. S. Youn, Y. J. Shin, and L. J. Guo, "Transparent and Flexible Polarization-Independent Microwave Broadband Absorber," *ACS Photonics,* vol. 1, pp. 279-284, Feb. 2014.

[50] T. Jang, J. Choi, and S. Lim, "Compact Coplanar Waveguide (CPW)-Fed Zeroth-Order Resonant Antennas With Extended Bandwidth and High Efficiency on Vialess Single Layer," *IEEE Transactions on Antennas and Propagation,* vol. 59, pp. 363-372, Mar. 2011.

[51] J. Oh and K. Sarabandi, "A Topology-Based Miniaturization of Circularly Polarized Patch Antennas," *IEEE Transactions on Antennas and Propagation,* vol. 61, pp. 1422-1426, Mar. 2013.

[52] A. Lai, K. M. K. H. Leong, and T. Itoh, "Infinite Wavelength Resonant Antennas With Monopolar Radiation Pattern Based on Periodic Structures," *IEEE Transactions on Antennas and Propagation,* vol. 55, pp. 868-876, Mar. 2007.

[53] J.-H. Park, Y.-H. Ryu, J.-G. Lee, and J.-H. Lee, "Epsilon Negative Zeroth-Order Resonator Antenna," *IEEE Transactions on Antennas and Propagation,* vol. 55, pp. 3710-3712.

[54] J. Oh and K. Sarabandi, "Low Profile, Miniaturized, Inductively Coupled Capacitively Loaded Monopole Antenna," *IEEE Trans. Antennas Propagation,* vol. 60, pp. 1206-1213, March 2012.

[55] C. Caloz and T. Itoh, *Electromagnetic Metamaterials*: John Wiley & Sons, 2005.

[56] D. S. Gray, J. Tien, and C. S. Chen, "High-Conductivity Elastomeric Electronics," *Advanced Materials,* vol. 16, pp. 393-397, Apr. 2004.

[57] K. Ellmer, "Past achievements and future challenges in the development of optically transparent electrodes," *Nature Photonics,* vol. 6, pp. 809-817, Nov. 2012.

[58] R. E. Glover and M. Tinkham, "Conductivity of Superconducting Films for Photon Energies between 0.3 and 40kTc," *Physics Review,* vol. 108, pp. 243-256, Oct. 1957.

[59] A. Khan, S. Lee, T. Jang, Z. Xiong, C. Zhang, J. Tang, *et al.*, "High-Performance Flexible Transparent Electrode with an Embedded Metal Mesh Fabricated by Cost-Effective Solution Process," *Small,* vol. 12, pp. 3021-3030, June 2016.

[60] S. Lee, J. Lee, E. Lee, J. Choi, J. Jung, J. Jung, *et al.*, "High Durable AgNi Nanomesh Film for a Transparent Conducting Electrode," *Small,* vol. 10, pp. 3767-3774, Sep. 2014.

[61] B. Han, K. Pei, Y. Huang, X. Zhang, Q. Rong, Q. Lin, *et al.*, "Uniform Self Forming Metallic Network as a High Performance Transparent Conductive Electrode," *Advanced Materials,* vol. 26, pp. 873-877, Feb. 2014.

[62] M. Vosgueritchian, D. J. Lipomi, and Z. Bao, "Highly Conductive and Transparent PEDOT:PSS Films with a Fluorosurfactant for Stretchable and Flexible Transparent Electrodes," *Advanced Functional Materials,* vol. 22, pp. 421-428, Nov. 2012.

[63] J. Groep, P. Spinelli, and A. Polman, "Transparent Conducting Silver Nanowire Networks," *Nano Letters,* vol. 12, pp. 3138-3144, May 2012.

[64] A. E. Hollowell and L. J. Guo, "Nanowire Grid Polarizers Integrated into Flexible, Gas Permeable, Biocompatible Materials and Contact Lenses," *Advanced Optical Materials,* vol. 1, pp. 343-348, Apr. 2013.

[65] C. A. Balanis, *Antenna Theory*: John Wiley & Sons, 2012.
[66] N. K. Das, T. Inoue, T. Taniguchi, and Y. Karasawa, "An Experiment on MIMO System Having Three Orthogonal Polarization Diversity Branches in Multipath-Rich Environment," *Proc. 60th IEEE Veh. Technol Conf.,* vol. 2, pp. 1528–1532, September 2004.
[67] E. R. Iglesias, O. Q. Teruel, and M. S. Ferflifldez, "Compact Multi mode Patch Antennas for MIMO Applications," *IEEE Antennas Propag. Mag.,* vol. 50, pp. 197–205, April 2008.
[68] K.-M. Mak, H. Wong, and K.-M. Luk, "A Shorted Bowtie Patch Antenna With a Cross Dipole for Dual Polarization," *IEEE Antennas and Wireless Propagation Letters,* vol. 6, pp. 126-129, April 2007.
[69] M. Barba, "A high-isolation, wideband and dual-liear polarization patch antenna," *IEEE Trans. Antennas Propagation,* vol. 56, pp. 1472-1476, May 2008.
[70] A. Adrian and D. H. Schaubert, "Dual aperture-coupled microstrip antenna for dual or circular polarization," *Electronics Letters,* vol. 23, pp. 1226-1228, November 1987.
[71] C.-Y. Chiu, J.-B. Yan, and R. D. Murch, "Compact Three-Port Orthogonally Polarized MIMO Antennas," *IEEE Antennas and Wireless Propagation Letters,* vol. 6, pp. 619-622, January 2007.
[72] X. Gao, H. Zhong, Z. Zhang, Z. Feng, and M. F. Iskander, "Low-Profile Planar Tripolarization Antenna for WLAN Communications," *IEEE Antennas and Wireless Propagation Letters,* vol. 9, pp. 83-86, February 2010.
[73] H. Zhong, Z. Zhang, W. Chen, Z. Feng, and M. F. Iskander, "A Tripolarization Antenna Fed by Proximity Coupling and Probe," *IEEE Antennas and Wireless Propagation Letters,* vol. 8, p. 2009, April 2009.
[74] B. Bari, J. Lee, T. Jang, P. Won, S. H. Ko, K. Alamgir, *et al.*, "Simple hydrothermal synthesis of very-long and thin silver nanowires and their application in high quality transparent electrodes," *Journal of Materials Chemistry A,* vol. 4, pp. 11365-11371, 2016.
[75] D. Deslandes and K. Wu, "Integrated microstrip and rectangular waveguide in planar form - IEEE Microwave and Wireless Components Letters [see also IEEE Microwave and Guided Wave Letters]," pp. 1-3, April 30 2001.
[76] M. Bozzi, A. Georgiadis, and K. Wu, "Review of substrate-integrated waveguide circuits and antennas," *IET Microwaves, Antennas & Propagation,* vol. 5, p. 909, February 1 2011.
[77] D. M. Pozar and S. M. Duffy, "A Dual-Band Circularly Polarized Aperture-Coupled Stacked Microstrip Antenna for Global Positioning Satellite," *IEEE Trans. Antennas Propagation,* vol. 45, pp. 1618-1625, November 1997.
[78] J. Granholm and N. Skou, "Dual-frequency, dual-polarization microstrip antenna array devel-opment for high-resolution, airborne SAR," *in Proc. Asia-Pacific Microwave Conf., Sydney, Australia,* pp. 17-20, 2000.